Photochemical Studies:
Method Development and Evaluation

A THESIS
SUBMITED TO THE FACULTY OF THE
GRADUATE SCHOOL
OF THE UNIVERSITY OF MINNESOTA

Kelsey Anne Parker

IN PARTIAL FULFILLMENT OF THE REQUIREMENTS
FOR THE DEGREE OF
DOCTOR OF PHILOSOPHY

Advisor: Donald G. Truhlar
March 2020

Acknowledgments

I want to acknowledge and thank many people in my group for their help with research and for their friendship. I thank Dr. Chad E. Hoyer, Dr. Laura E. Fernandez, Dr. Rubén M. Pañeda, and Dr. Shaohong L. Li for helping me get started in a new field. I want to posthumously thank Steven for his patience, tremendous help with chemistry and coding problems, and unique humor. I thank Dr. Zoltan Varga and Siriluk Kanchanakungwankul for working with me on diabatization through the highs and lows and for finding silver linings when things didn't work. I thank Lyuben Borislavov, Dr. Sijia S. Dong, and Linyao Zhang for working with me on dynamics projects and being super helpful and kindhearted. I thank Dr. Yinan Shu for helping me with everything all the time and for thought provoking discussions. I thank Dr. Pragya Verma and Jie J. Bao for their constant friendship and long, fun discussions about chemistry and life. I thank the many other group members I was lucky to get to know who inspire me with their work. Lastly, I want to acknowledge and thank my advisor, Dr. Donald G. Truhlar. He is a great teacher and I am always shocked by the sheer breadth and depth of his knowledge. I want to thank him for the tremendous opportunity and experience to be a part of his group.

Dedication

I dedicate this work to my dad, mom, and sister, Lauren. My dad, for teaching me to code and talking through problems when I would get stuck. My mom for being my work buddy and for dropping everything to help when I needed her. Lauren for being my best friend and for her great advice. I also want to thank my friends for their support and encouragement: Laura, E, Ronnie, Mimi, Xiaoling, Heather, Sarah, Heather Tori, Sanjana, Kari, Rose and Marckileine. Thanks for inspiring me, making me laugh, and for the fun times throughout my years in graduate school.

Abstract

Photochemistry is an important area of research, but modeling photochemical systems is complex and expensive. In this dissertation, I present my work on the testing and development of methods for photochemistry studies. Chapter 1 introduces some important concepts. In Chapter 2, I present an electronic structure method for excited states called the dual-functional Tamm-Dancoff approximation. This method is based on the relatively inexpensive time-dependent density functional theory (TDDFT) and it gives similar results to TDDFT away from conical intersection seams (CISs). Near CISs involving the ground state, DF-TDA shows an improvement over TDDFT because it gives the correct (F-2)-dimensionality of these seams, where F is the number of degrees of freedom of the potential energy surfaces. In Chapters 3 and 4, I present work on two diabatization methods for coupled electronic states: the dipole, quadrupole, electrostatic potential method and the N/D method. Neither method requires a user to define diabatic molecular orbitals, and both solve for diabatic energies without relying on following a path through coordinate space. Both methods are shown to be successful for a wide range of test cases. In Chapter 5, I present work on a method called extended Hamiltonian molecular dynamics, which is designed to be an inexpensive way to cut back on zero point energy leakage. I present our findings that this method is successful for several small test systems. Finally in Chapter 6, I present work on the construction of potential energy surfaces suitable for studying the photodissociation of methylamine. This work involves diabatization and a method called anchor points reactive potential, which is a multiscale method designed for making analytic representations of high-dimensional potential energy surfaces. My work on methylamine involves the extension of this method to a more complex system than it has previously been applied to, and I compare my surfaces to previous theoretical and experimental results and find good agreement. A theme of all this work is improving our understanding of photochemistry and designing methods to model these systems that are cost effective and generally applicable.

Contents

List of Figures

List of Tables

Introduction

Photochemistry is an exciting field both from the standpoint of questions in fundamental science and for applications to important practical problems. The science behind light-matter interactions has many unsolved mysteries, which present essential questions about chemistry and physics and require new ideas and ways of thinking about our applications of mathematics and computer science. Work on understanding these issues can make important contributions to energy research, where we are in dire need of alternatives to nonrenewable energy sources.

To address the many challenges present in this area of research, the Truhlar group is working to develop inexpensive, accurate methods, which can be applied to general photochemical problems. In this dissertation, I present three new methods we've developed towards this end: the dual-functional Tamm-Dancoff approximation, N/D diabatization, and extended Hamiltonian molecular dynamics. In addition, I present an extension of the method of anchor points reactive potentials.

The dual-functional Tamm-Dancoff approximation (DF-TDA) is an electronic structure method, designed to fix the problem of time-dependent density functional theory (TDDFT) that it gives the wrong dimensionality of conical intersection seams involving the ground electronic state.[1] DF-TDA has an important difference from conventional TDDFT. In DF-TDA, we use different functionals for orbital optimization of the ground state and for calculating the time-dependent response rather than using the same functional for both steps as is done in conventional TDDFT. This change introduces coupling between the ground and excited states, which fixes the potential energy surface topology near S_0/S_1 conical intersections, where S_0 is the ground state and S_1 is the first excited state. Away from conical intersections, DF-TDA gives results similar to TDDFT. The details of this method are given in Chapter 2.

N/D diabatization is new method for transforming from an adiabatic electronic state representation to a diabatic one. The adiabatic representation is a result of the Born-Oppenheimer separation of electronic and nuclear degrees of freedom. Adiabatic states are coupled by nonadiabatic couplings (NACs), which are matrix elements resulting from the action of the nuclear momentum and nuclear kinetic energy operators acting on the adiabatic electronic states. In many cases, these coupling are negligible, and the dynamics is electronically adiabatic. However, for geometries at which two electronic states are close in energy, the Born-Oppenheimer approximation breaks down, the NACs are not negligible, and the NACS cause electronically nonadiabatic transitions. Near such geometries the adiabatic states are not smooth functions of geometry and the NACS become singular, making the adiabatic representation very difficult to work with. As an alternative, we can switch to a diabatic representation. In a diabatic representation, the diabatic states change smoothly along nuclear coordinates,[2] the NACS are negligible, and

the coupling of the states is due to smooth functions. Our N/D method makes use of the NACs and adiabatic energy gradients to convert adiabatic energies to diabatic energies and couplings. The details of this method are given in Chapter 4.

The extended Hamiltonian molecular dynamics (EHMD) method is a simple way to prevent unphysical zero-point energy leakage when running molecular dynamics simulations. In classical dynamics, energy moves between vibrational modes without consideration of conservation of zero-point energy. To prevent this in a cost effective way, we developed a method that simultaneous runs two coupled trajectories. These trajectories are replicas of one another connected by a spring potential. We have shown that this greatly decreases unphysical energy redistribution for simple test cases. This work is described in Chapter 5.

In addition to work on these new methods, I also present results on the testing and further development of methods previously developed in the Truhlar group including dipole, quadrupole (DQ) diabatization,[3] which is discussed in Chapters 3 and 6 and the anchor points reactive potential method (APRP),[4] discussed in Chapter 6.

DQ diabatization uses dipole moments and quadrupole moments to derive diabatic potential energy surfaces. We tested the addition of another property to this scheme, the electrostatic potential (Φ), and we found that it can improve the results when used either with the dipole and quadrupole (DQΦ) or when used only with the dipole (DΦ). We have also incorporated coordinate dependent weights for the quadrupole contribution and applied this to various dissociations along the potential energy surfaces of methylamine with good results. After generating diabatic data for methylamine, we fit this data to construct analytic representations of diabatic potential energy surfaces and their couplings (the diabatic surfaces and their coupling together form a diabatic potential energy matrix (DPEM)).

Fitting of the DPEM involved a large number of electronic structure calculations and making an extended version of the APRP method, which is a multiscale approach for potential energy surfaces of large systems. With APRP, certain coordinates along the surface are treated at higher accuracy compared to other coordinates, which are less important for dynamics. We expanded on the functional form of this fitting procedure because our system involves more complicated geometrical changes than were present in the systems for which the method was originally designed. Diagonalizing the DPEM yields adiabatic potential energy surfaces, and we compared our results to previous experimental and theoretical studies of the adiabatic surfaces with good agreement.

A theme that runs through all the above work is to develop, showcase, and expand on methods for theoretical and computational photochemical studies.

1 Background

Before presenting my graduate work, I give some background information that is relevant for the following chapters. Section 1.1 deals with the concept of potential energy surfaces for general purposes and for photochemistry. Section 1.2 deals with electronic structure calculations. Section 1.3 gives general details about diabatic representations and diabatization.

1.1 Potential Energy Surfaces

To study chemical systems, computational chemists often employ the concept of potential energy surfaces (PES). This concept is explained for a simple case in section 1.1.1. It is generalized to larger systems in 1.1.2, and considerations for photochemistry are presented in Section 1.1.3.

1.1.1 One-dimensional, Single-State Surfaces

To create PESs for a system, we must consider how the energy depends on the system's structure. We start with a simple example - a two-atom system. This system is shown as atom 1 and atom 2 in Figure 1.1. To change the structure of the system, we can vary the bond distance, R_{12}. The energy will change along this nuclear coordinate and by generating data, we are building a potential energy surface.

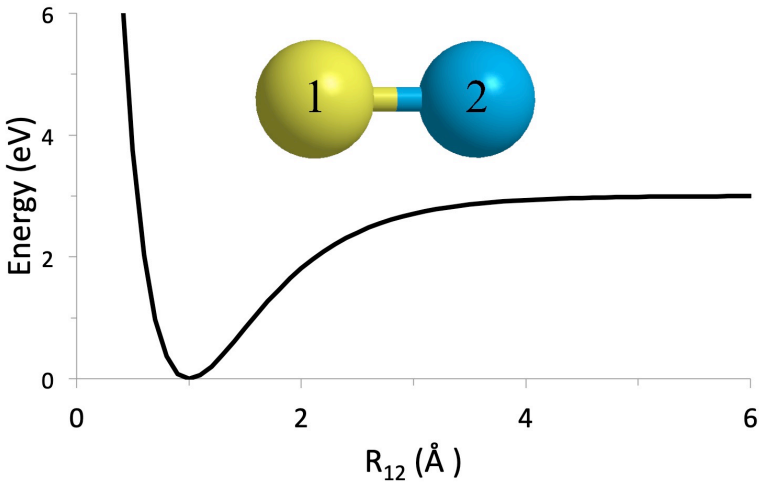

Figure 1.1 Potential energy surface for a two-atom system

This PES is one-dimensional; the only coordinate to describe the system is a single bond length. We plot this bond length on the x-axis and the potential energy on the y-axis in Figure 1.1. To study larger systems, we have to consider more complicated topologies.

1.1.2 Higher-Dimensional Surfaces

Larger systems have many more coordinates to consider. Figure 1.2(a) shows a slice of a high-dimensional surface. The z-axis is energy while the x-axis and y-axis are two coordinates of the system; these could be internuclear distances, bond angles, torsions, and out-of-plane bends. The figure is called a slice because we are only visualizing a small, 2-dimensional part of the multidimensional surface. Most of the coordinates are held at fixed values to generate this slice. Figure 1.2(b) shows a system with many atoms and therefore, many internal coordinates. Describing the energy as a function of this system's coordinates is much more complicated than the two-atom case in Section 1.1.1.

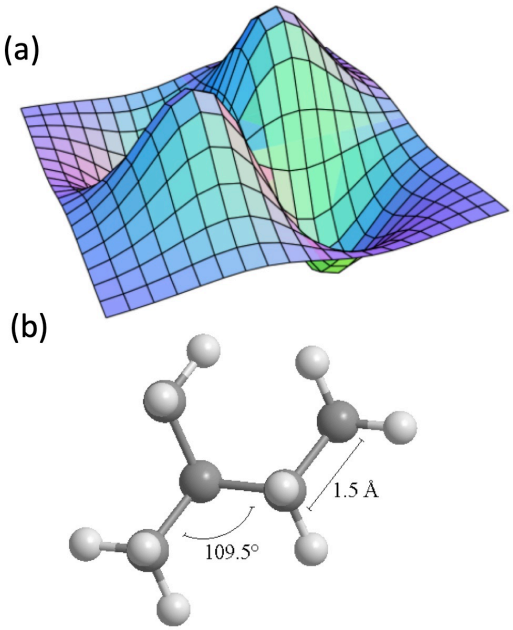

Figure 1.2. (a) slice of a high-dimensional PES (b) a many-atom system that has high-dimensional PESs

The dimensionality of a surface is determined by the system's degrees of freedom. In general, a system has $3N - 6$ degrees of freedom, where N is the number of atoms. The 3 multiple comes from determining an atom's location in Cartesian space. The subtraction of 6 comes from the fact that we could translate the entire system in three directions or rotate a three-dimensional system around three axes, and not change any of the atoms positions relative to one another. This means there are 6 coordinates that will not have an effect on the potential energy of the system.

From the degrees of freedom equation, we can see that many systems of interest will have very high-dimensional PESs. Collecting energy data along the high-dimensional coordinate space is unfeasible. As an example, a relatively small seven-atom system has 15 degrees of freedom. To consider just five energies along each degree of freedom for the entire coordinate space would require 5^{15} energy points. Instead of this impossible task, we approach this problem with a multiscale approach that prioritizes regions of the surface we are interested in and disregards regions that are high in energy

or inaccessible. This topic is explored in greater detail in Chapter 6, where we apply a multiscale method to treat a seven-atom system, methylamine.

1.1.3 Potential Energy Surfaces for Photochemistry

In photochemistry, chemical systems can access excited states, which correspond to higher-energy PESs. The ground-state's and excited-state's PESs are coupled to one another (more details on this in Sections 1.2 and 1.3), and the photochemical behavior of the system is determined by this coupling and the topologies of the surfaces. PESs can meet (have the same energy) at seams called conical intersections. An example of this is shown for two surfaces in Figure 3. Conical intersections are seams in $(F - 2)$ dimensional space, where F is the number of degrees of freedom. The topology of these seams is very important for photochemistry research, but time-dependent density functional theory has the wrong dimensionality of seams between the ground and higher excited states. This motivates our work described in Chapter 2.

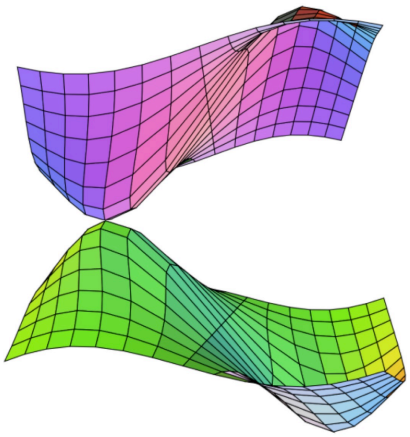

Figure 1.3. Two potential energy surfaces meeting at a conical intersection

To summarize Section 1.1, for photochemical research, we must find accurate and low-cost ways to study high-dimensional PESs.

1.2 Electronic Structure Calculations

To collect energy data and other information about a chemical system at coordinates, we use electronic structure calculations. This involves finding approximate solutions to the Schrödinger equation, which is the topic of Section 1.2.1. In Section 1.2.2, I briefly describe calculations preformed in this dissertation.

1.2.1 The Schrödinger Equation

To determine the energy of a chemical system, we use the Schrödinger equation,[2]

$$\left\{-\frac{1}{2\mu}\nabla_{\mathbf{R}}^2 + \hat{H}_{el}(\boldsymbol{R},\boldsymbol{r})\right\}\Psi(\boldsymbol{R},\boldsymbol{r}) = E\Psi(\boldsymbol{R},\boldsymbol{r}) \qquad \text{Eq. (1)}$$

In this equation, μ is the nuclear mass in isoinertial coordinates; $\nabla_{\mathbf{R}}^2$ is the Laplacian; $\hat{H}_{el}$ is the electronic Hamiltonian operator, which includes electronic kinetic energy, electron-electron, electron-nuclear, and nuclear-nuclear interactions; **R** is nuclear coordinates; **r** is electronic coordinates; and $\Psi(\boldsymbol{R},\boldsymbol{r})$ is the wave function. In eq. (2), we expand the wave function in terms of nuclear wave functions, $\psi_j(\boldsymbol{R})$, that depend on **R** and electronic states, $\phi_j(\boldsymbol{r};\boldsymbol{R})$, that depend on **r** and parametrically depend on **R**. These electronic states are normalized eigenfunctions of the electronic Hamiltonian. The subscript *j* denotes the state (i.e., $j = 1$ is the ground state, $j = 2$ is the first excited state, …).

$$\Psi(\boldsymbol{R},\boldsymbol{r}) = \sum_{j=1}^{n}\psi_j(\boldsymbol{R})\phi_j(\boldsymbol{r};\boldsymbol{R}) \qquad \text{Eq. (2)}$$

By plugging eq. (2) into eq. (1), we get eq. (3):

$$\left\{-\frac{1}{2\mu}\nabla_{\mathbf{R}}^2 + V_j(\mathbf{R})\right\}\psi_j(\mathbf{R}) + \sum_k\left\{-\frac{1}{\mu}\vec{f}_{jk}(\mathbf{R})\cdot\nabla_{\mathbf{R}} - \frac{1}{2\mu}t_{jk}(\mathbf{R})\right\}\psi_k(\mathbf{R}) = E\psi_j(\mathbf{R}) \qquad \text{Eq. (3)}$$

where

$$V_j(\mathbf{R}) = \int \phi_j^*(\boldsymbol{r};\boldsymbol{R})\hat{H}_{el}\,\phi_j(\boldsymbol{r};\boldsymbol{R})d\boldsymbol{r} \quad \text{Eq. (3a)}$$

$$\vec{f}_{jk}(\mathbf{R}) = \int \phi_j^*(\boldsymbol{r};\boldsymbol{R})\nabla_R\,\phi_k(\boldsymbol{r};\boldsymbol{R})d\boldsymbol{r} \quad \text{Eq. (3b)}$$

$$t_{jk}(\mathbf{R}) = \int \phi_j^*(\boldsymbol{r};\boldsymbol{R})\nabla_R^2\,\phi_k(\boldsymbol{r};\boldsymbol{R})d\boldsymbol{r} \quad \text{Eq. (3c)}$$

In eq. (3a), $V_j(\boldsymbol{R})$ is the potential energy in the adiabatic representation of the various states, denoted again with *j*. These adiabatic energies of the states (or adiabats) that are functions of nuclear coordinates give us PESs, as described in Section 1.1. We always order the energy of the adiabatic states from smallest to largest (i.e. $V_1 \leq V_2 \leq V_3$ ...). In eq. (3b), $\vec{f}_{jk}(\mathbf{R})$ is the nuclear momentum coupling between states *j* and *k*. This vector has size 3*N* and it is commonly called the nonadiabatic coupling. In Chapter 4, I give details on a diabatization method we developed that uses the nonadiabatic coupling vectors and adiabatic energy gradients. The term, $t_{jk}(\mathbf{R})$ in eq. (3c) is the kinetic energy coupling, which is generally neglected.

1.2.2 Electronic Structure Methods in this Dissertation

There are various electronic structure methods one can use with different levels of accuracy and cost. These methods are often broken into two major categories: wave function theory (WFT) and density functional theory (DFT). In WFT, the goal is to find wave functions, $\phi_j(\boldsymbol{r};\boldsymbol{R})$, and energies that solve the electronic Hamiltonian. In contrast to WFT, DFT solves for energies and state properties using the electron density. DFT can be less expensive than WFT methods that have similar accuracy.

For my work described in this dissertation, I've used both WFT and DFT methods. More specifically, In Chapters 2 and 6, I give results from DFT and time-

dependent density functional (TDDFT) calculations for excited states.[5-9] In Chapters 3 and 4, I used the WFT method, complete active space self-consistent field (CASSCF)[10-14] and in Chapter 6, I used the WFT method, complete active space perturbation theory (CASPT2)[15]. More specific information on the electronic structure methods can be found in the following chapters.

1.3 Diabatization

So far, we have described PESs and calculations in the adiabatic representation. This representation is problematic in photochemistry, which is the subject of Section 1.3.1. As an alternative to the adiabatic representation, we can instead use a diabatic representation, the details of which are given in Section 1.3.2. The process of switching from the adiabatic representation to a diabatic representation is called diabatization, which is the topic of Section 1.3.3.

1.3.1 Breakdown of the Born-Oppenheimer Approximation in Photochemistry

As described in Sections 1.1.3 and 1.2.1, for photochemistry problems, we must consider multiple surfaces and regions of coordinate space where the surfaces approach one another. In these regions of coordinate space, the adiabatic states and nonadiabatic coupling vectors change rapidly. This results from a breakdown of the Born-Oppenheimer approximation; the separation of nuclear and electronic degrees of freedom is not valid. For fitting purposes, this is very problematic. The adiabatic energies are unsmooth at avoided crossing and conical intersections, where the surfaces have high-dimensional cuspidal ridges. The nonadiabatic coupling vector grows rapidly as the adiabatic PESs approach and are singular along conical intersection seams. To avoid

issues that arise in working with the adiabatic representation, we consider a different representation called diabatic.

1.3.2 Diabatic Representations

A diabatic representation is defined as a representation where the electronic wave functions are smooth functions of nuclear coordinates and nonadiabatic coupling can be neglected.[2, 16] There are many ways one could derive diabatic states. In a diabatic representation, the diabatic energies (called diabats and denoted in this work as U_{XX} where $X = 1,2,3,\ldots$) are smooth functions of nuclear coordinates, which makes them much easier to fit to analytical functions. The diabats are the diagonal elements of the electronic Hamiltonian, and unlike adiabats, they are allowed to cross along nuclear coordinates (i.e. U_{11} could be less than, equal to, or greater than U_{22}). The off-diagonal elements of the diabatic Hamiltonian are called diabatic couplings.

By switching to a diabatic representation, we can fit our PES data to analytic surfaces to create analytic PESs for photochemistry research.

1.3.3 Diabatization

Changing adiabatic data to diabatic data is a procedure called diabatization. Many diabatization methods have been developed with no method being considered the best for general applications at low cost. In our work on diabatization, we have a number of criteria that we have worked towards. First, we've focused on methods that are adiabatic equivalent. This means that the diabatic states span the same space as the adiabatic states. This is convenient because it allows us to easily transform from the diabats back to the adiabats by diagonalizing the electronic Hamiltonian. Another important criteria for our

diabatization methods is path independence (also referred to as direct diabatization). This means that the diabats generated at a particular structure in the coordinate space do not depend on previous calculations at other locations in coordinate space. As was discussed in Section 1.1, we are often working in high-dimensional coordinate space and following a path through that space would be a huge and complicated undertaking. A third criterion for our methods is that they are orbital free. This means our methods do not require one to generate diabatic molecular orbitals. Orbital-free methods are preferred because they generally require less user input and less knowledge about the system under study. Finally, we want our diabats to approach the adiabats in regions of the PESs where the states are well separated, which is convenient for dynamics calculations. We have worked towards diabatization methods that meet the criteria above in addition to the criteria of low-cost and general applicability. I present two diabatization methods described in this dissertations that largely meet these goals. This is the subject of chapters 3 and 4.

2 Dual-Functional Tamm-Dancoff Approximation: A Convenient Density Functional Method that Correctly Describes S_1/S_0 Conical Intersections

*Y. S. and K. P. contributed equally to this work

Due to the lack of double excitation energies, time-dependent Kohn-Sham density functional theory generates conical intersection seams with the wrong dimensionality between the ground- and excited-state. We present a new Kohn-Sham density functional theory with global accuracy comparable with the conventional version that recovers the double cone topology of the surfaces at S_1/S_0 conical intersection seams.

2.1 The S_1/S_0 Dimensionality Problem in Time-Dependent Density Functional Theory

Population transfer between electronic states often occurs in the vicinity of conical intersections (CIs), where two or more PESs are degenerate.[2, 17-24] CIs are $(F-2)$-dimensional seams (where F is $(3N-6)$, and N is the number of atoms), and the surfaces have the shape of a double cone in the two-dimensional branching space in which the surfaces separate. To be fully useful for studying photochemical processes, electronic structure theories should predict the correct cone-like topology.

The most widely used methods that include enough dynamic correlation energy to have quantitative accuracy and that predict the correct topology of CIs with the ground state are multireference methods (i.e., methods based on adding additional dynamic correlation to a multi-configurational reference function) in which the final step is a diagonalization, in particular, multi-state complete-active-space perturbation theory (MS-CASPT2),[25] multi-configuration quasidegenerate perturbation theory (MC-QDPT),[26] and multireference configuration interaction (MRCI).[27] But these methods can be

inconvenient because they require a sometimes difficult selection of appropriate active space orbitals for the reference function, especially when one wants to calculate PESs in an even-handed way for a range of geometries.

Linear response (LR) time-dependent density functional theory (TDDFT) based on Kohn-Sham density functional theory (KS-DFT) and the adiabatic approximation is widely used to compute electronic excitation energies because it provides an economical way to include dynamic correlation effects that are essential for quantitative accuracy, and it is conveniently based on a single-configuration reference state.[5-9] It is often preferred to employ the Tamm-Dancoff approximation (TDA)[28-36] which has a matrix formalism similar to the configuration interaction singles (CIS) approximation of wave function theory, and which can provide a more stable result than the full linear-response method;[37] LR-TDDFT with the TDA will be abbreviated here as KS-TDA. The LR-TDDFT and KS-TDA methods are especially useful because of their low cost compared to other methods that include the bulk of the dynamic correlation. However, LR-TDDFT and KS-TDA only contain explicit amplitudes connecting the ground state to singly excited determinants, and hence – due to Brillouin's theorem[38] – they fail at describing PESs near S_1/S_0 conical intersections because they exhibit $(F-1)$-dimensional conical intersection seams.[1] The lack of double excitation character has been a long-standing problem in LR-TDDFT and KS-TDA.[39-42] In recent years, alternative methods based on KS-TDA have been developed. These newly developed alternatives can describe the PESs near S_1/S_0 conical intersection by introducing the coupling between ground and singly excited states, and hence some partial double excitation character is put into the formalism.[43-49]

2.2 The Dual Functional Tamm-Dancoff Approximation

In this work, we propose a new method, called the dual-functional Tamm-Dancoff approximation (DF-TDA), for application to photochemical problems. The DF-TDA is based on KS-TDA, but it predicts the correct dimensionality of the S_1/S_0 conical intersection seam. It does this without explicitly employing double excitations, and the first step is a standard Kohn-Sham calculation, so there are no complications due to active space selection in multireference methods. Furthermore, it involves only a particularly simple modification of the conventional procedure. We will begin with a brief summary of KS-TDA and illustrate its failure near S_1/S_0 conical intersections as a motivation for DF-TDA.

The KS-TDA effective Hamiltonian matrix **H** has four blocks, in particular, the KS–KS block (which is 1×1), two TDA–KS coupling blocks (which are $1\times nm$ and $nm\times1$, where n is the number of occupied orbitals and m is the number of virtual orbitals), and a TDA–TDA block (which is which is $nm\times nm$). Because of Brillouin's theorem, all elements of the TDA–KS blocks are zero. Hence the KS-TDA Hamiltonian is

$$\mathbf{H} = \begin{bmatrix} \varepsilon_1 & \mathbf{0} \\ \mathbf{0} & \mathbf{A} \end{bmatrix} \tag{1}$$

where ε_1 is the KS ground state energy (the energy of state S_0), and matrix **A** is the Hermitian TDA–TDA block. Diagonalization of the KS–TDA Hamiltonian can be achieved by diagonalizing **A:**

$$\mathbf{AZ} = \boldsymbol{\omega}\mathbf{Z} \tag{2}$$

where $\boldsymbol{\omega}$ is a diagonal matrix of excitation energies ($\varepsilon_j - \varepsilon_1$, where j labels an excited state), and **Z** is a matrix composed of amplitude vectors for the excited states.

The well-known explanation[50] of why the branching space is two-dimensional is that two conditions are required for an intersection between states i and j; one must have $H_{ij} = 0$ and $H_{ii} = H_{jj}$. Because $H_{1j} = 0$ in eq 1 at all geometries (by Brillouin's theorem), there is

only one condition required for degeneracy between the ground state (with energy ε_1) and an excited state (with energy ε_j), and so the crossing occurs in $F - 1$ dimensions. Hence, introducing the coupling between the KS ground state and its single excitations is the key to recovering the double cone topology of the PESs near an S_1/S_0 conical intersection. One possible solution is that, when building the KS-TDA Hamiltonian, another set of orbitals is used instead of using KS self-consistent orbitals. For example, approaches hacve been proposed that use variationally orbital-adapted CIS optimization of orbitals by minimizing both HF ground and CIS excited states,[47] that use the particle-particle random phase approximation to optimize the orbitals by minimizing a +2 cation state,[48] and that apply LR-TDDFT starting from a mixed ground and first excited state.[49] In the method proposed here, to be called dual-functional TDA or DF-TDA, we propose a very simple strategy, namely, optimize the orbitals with one exchange–correlation functional and build the KS-TDA Hamiltonian with a different functional. The only complication is that in most KS-TDA algorithms, as presently coded, only the $nm \times nm$ submatrix **A** is diagonalized, but in the new algorithm one must diagonalize the whole $(nm+1) \times (nm+1)$ matrix **H**. The calculations are performed with our locally modified version of GAMESS.[46, 51-54] The locally modified version is called *Gamess+DF*, and the modified routines are available online.[54]

Two questions now need to be answered. (1) Does using different functionals for the ground-state calculation and the linear response calculation decrease the accuracy of TDDFT? (2) Does the dual-functional procedure yield reasonable potential energy surfaces in the vicinity of a conical intersection? We next examine these two questions. We employed three density functionals for the illustrative examples: M06,[32] M11,[55] and MN15.[56]

2.3 Validation for Vertical Excitation Energies

We start by testing the accuracy of DF-TDA at the ground-state minimum-energy geometries. We use the 6-311+G(2d,p) basis set.[57] Table 1 shows the vertical excitation energies of low-lying singlet excited states of five small organic molecules as computed by five TDDFT methods and compared to best estimates[34, 58-59] from the literature. The table includes excitations that we label in terms of the dominant contributing single excitation as $n \rightarrow \pi^*$, $\sigma \rightarrow \pi^*$, and $\pi \rightarrow \pi^*$ excitations (only the hole orbital is listed since the particle orbital is always π^*); this labeling is nominal in cases like the A_g state of butadiene where the excitation is usually described as a double excitation. We use the notations "DF-TDA/F1:F2" and "F1:F2" to indicate the two functionals employed in DF-TDA, for example, M06:MN15 indicates that the orbitals are obtained by M06, and the response is calculated with MN15.

Table 2.1 shows that M06:MN15 always agrees with KS-TDA/MN15 within 0.20 eV, and in 9 cases out of 12, it agrees within 0.13 eV; and MN15:M06 agrees well with KS-TDA/M06, with 11 of the 12 differences in the range 0.10-0.25 eV. The table clearly shows that for the functional chosen the accuracy of DF-TDA is mostly affected by the functional used for response (F2). It is interesting that F1:F2 usually predicts vertical excitation energies about 0.1 eV higher (on average) than KS-TDA/F2. A similar behavior is often found when one compares the vertical excitation energies of CIS and configuration interaction singles and doubles (CISD). Because doubly excited configurations correlate the ground state, CISD is biased towards the reference ground state.[60] Fortunately, this "over-stabilization effect" is very small in our DF-TDA calculations

The results in Table 2.1 show that the mean signed difference between M11:M06 and MN15:M06 is only -0.07 eV. This further supports the conclusion that the accuracy of DF-TDA is mostly determined by the F2 functional for the functionals used here. The

mean unsigned errors (MUEs, relative to the best estimates) of the KS-TDA and DF-TDA methods compared to the best estimates are given in the bottom row of the table. This row shows that the F1:F2 has a general accuracy comparable to KS-TDA/F2. This would indicate that if F2 has been validated for a certain level of accuracy with KS-TDA, one does not need a new validation with DF-TDA; the results should be similar.

Table 2.1. The vertical excitation energies (eV) of singlet low-lying excited states of organic molecules as calculated by five TDDFT and DF-TDA methods compared to best estimates from the literature. The last row shows the mean unsigned error (MUE) compared to the best estimates.

Molecules	States	Best Estimates	KS-TDA/ M06	DF-TDA/ M11:M06	DF-TDA/ MN15:M06	KS-TDA/ MN15	DF-TDA/ M06:MN15
Acetone	$A_2(n)$	4.40	4.31	4.51	4.53	4.33	4.42
	$B_1(\sigma)$	9.10	8.51	8.66	8.71	8.71	8.83
	$A_1(\pi)$	9.40	8.54	8.73	8.82	9.39	9.51
Butadiene	$B_u(\pi)$	6.21	5.81	5.84	5.95	6.21	6.34
	$A_g(\pi)$	6.39	6.33	6.37	6.49	7.13	7.25
Ethylene	$B_{1u}(\pi)$	8.02	7.48	7.47	7.57	8.11	8.17
Formaldehyde	$A_2(n)$	3.88	3.84	4.01	3.97	3.86	3.90
	$B_1(\sigma)$	9.10	8.80	8.93	8.92	8.90	8.95
	$A_1(\pi)$	9.30	9.46	9.54	9.58	9.97	10.03
Furan	$B_2(\pi)$	6.32	5.98	6.05	6.20	6.55	6.74
	$A_1(\pi)$	6.57	6.57	6.65	6.76	6.97	7.17
	$A_1(\pi)$	8.13	7.75	7.85	7.98	8.69	8.88
MUE			0.32	0.28	0.24	0.28	0.35

We compare DF-TDA and KS-TDA calculations for many more combinations, which can be found in SI for the paper along with tables of the mean signed and unsigned differences with respect to KS-TDA/F1 and KS-TDA/F2. These tables show that generally the accuracy of an F1:F2 calculation tends to be close to the accuracy of the F2 calculation, but there are some exceptions. Most notable are some combinations of local and hybrid functionals. For example, DF-TDA/MN15:M06-L has 0.4 eV mean signed and unsigned differences compared with KS-TDA/M06-L, and DF-TDA/MN15-L:M06 has 0.55 eV mean signed and unsigned differences compared with KS-TDA/M06.

2.4 Investigation near Conical Intersections

We investigated DF-TDA near CIs by comparing the DF-TDA PESs in the vicinity of S_1/S_0 CIs calculated by MS-CASPT2. In particular we will consider the well-studied CIs in ammonia and ethylene. For both molecules we optimized the minimum-energy intersection (MECI) intersection geometry with the CIOpt[61] algorithm of *Molpro*.[62-63] The PESs were computed at the geometries along internal coordinates that lift the degeneracy. When we considered the ground-state equilibrium geometry, the optimized orbitals were always doubly occupied. When we consider paths near the CI we always allow different orbitals for different spins (also called spin-polarized or unrestricted Kohn-Sham) in the ground-state orbitals.

The MECI of ammonia was optimized by MS-CASPT2 with the 6-311+G(2d,p) basis set, an active space of eight electrons in seven orbitals, all electrons correlated by perturbation, and state averaging and multi-state diagonalization involving two states. The MECI turns out to be planar but with C_1 symmetry. One H atom, which we will call atom A, is farther (1.94 Å) from the N than the other two (N-H = 1.02–1.03 Å). We examined deviations from the MS-CASPT2 geometry along two internal coordinates (the same internal coordinates discussed previously[64]). One is the N–A stretch, and the other is an out-of-plane motion of the N atom with other atoms fixed. Figure 2.1 shows the PESs computed by MS-CASPT2 and M11:MN15 as functions of these coordinates. For the DF-TDA calculations, all excitation energies for the points in the figure are positive.

Figure 2.1(a) shows that the M11:MN15 energy gap between S_1 and S_0 lifts in a reasonable fashion. The energy levels of the optimized S_1/S_0 conical intersection relative to the S_0 minimum geometry at MS-CASPT2 theoretical levels are 5.02 and 5.04 eV for the two degenerate adiabatic states. At an N-H distance of 1.94 Å, the M11:MN15 calculation predicts 5.15 and 5.17 eV for ground and excited states, which are close to the MS-CASPT2 values. Figure 2.1(b) shows the PESs as a function of out-of-plane distance.

The M11:MN15 PESs near the S_1/S_0 conical intersection are very similar MS-CASPT2; the energy difference is smaller than 0.5 eV for most regions along the coordinate. A zoom in of the N-H dissociation coordinate is shown in Figure 2.1(c). It is clear that the PESs are smooth near the CI; no negative excitation energies were observed.

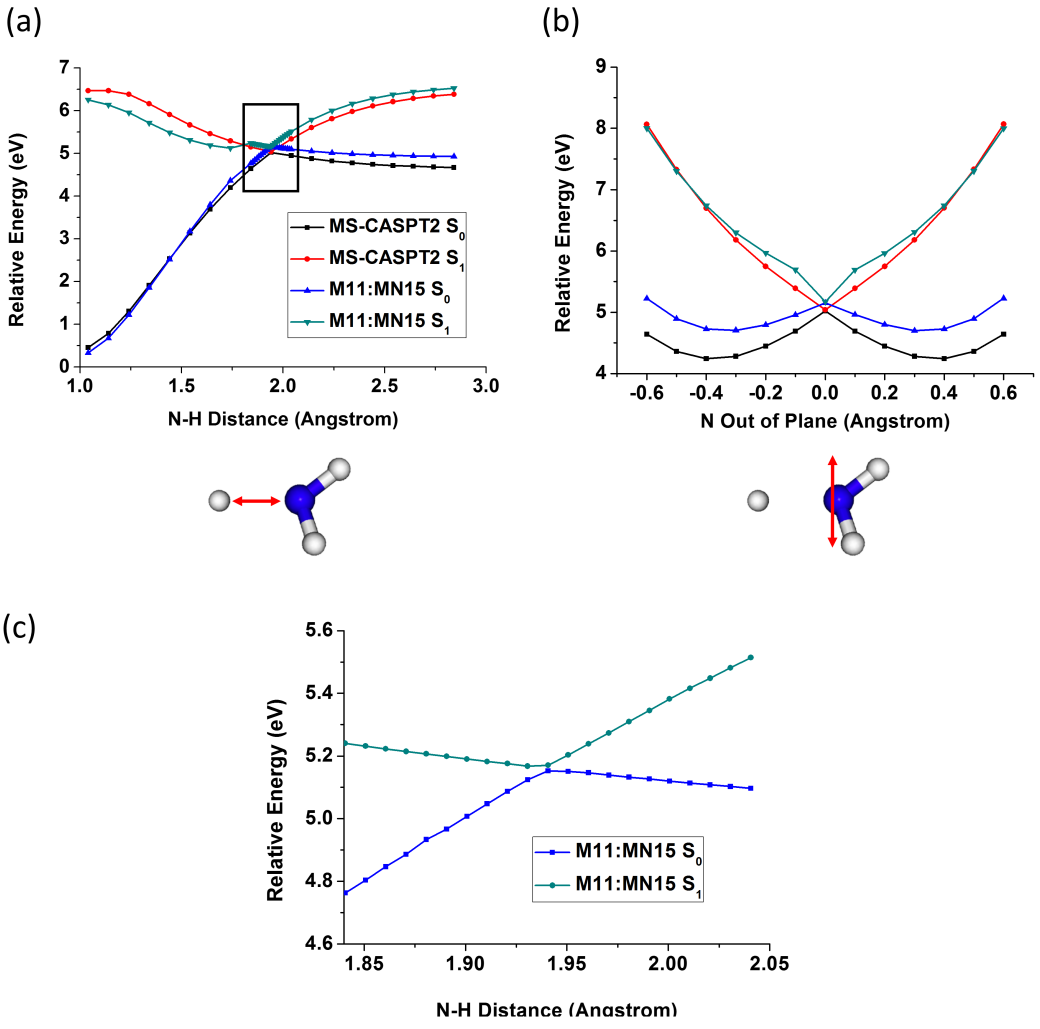

Figure 2.1. The PESs near S_1/S_0 ammonia CI along (a) the N-A dissociation coordinate, (b) the nitrogen out-of-plane coordinate, and (c) a zoom in of N-A dissociation coordinate calculated with CASPT2 and DF-TDA

For ethylene, the S_1/S_0 CI is optimized by MS-CASPT2/6-311+G(2d,p) with two active electrons in two orbitals and averaging of two states, and all electrons are correlated in the PT2 step. Figure 2.2 shows PESs computed along the pyramidalization

angle and twisting angle of the ethylene molecule (the same internal coordinates as discussed in a previous study[65]). For the DF-TDA calculations, all excitation energies for the points in the figure are positive. The MS-CASPT2 optimized CI is 4.76 eV above the ground state of the S_0 minimum-energy geometry. The M11:MN15 calculation predicts 4.63 and 4.75 eV at the same geometry, which is very close to MS-CASPT2 energy levels. (note that the levels are not precisely degenerate because we are at an MS-CASPT2 CI point but only close to an M11:MN15 CI point. If we did the comparison staring at the M11:MN15 MECI, we would get the tables turned, i.e., exact degeneracy with M11:MN15 and near degeneracy with MS-CASPT2). We find that the PESs computed by M11:MN15 and MS-CASPT2 are very similar with differences less than 0.3 eV in most regions. Figure 2.2(c) shows a zoom in of the potential curves as functions of the pyramidalization angle; at pyramidalization angle of 37 degrees, we found a point that is very close to the DF-TDA/M11:MN15 CI seam, with two nearly degenerate states at 4.73 and 4.75 eV above the ground state of the S_0 minimum geometry.

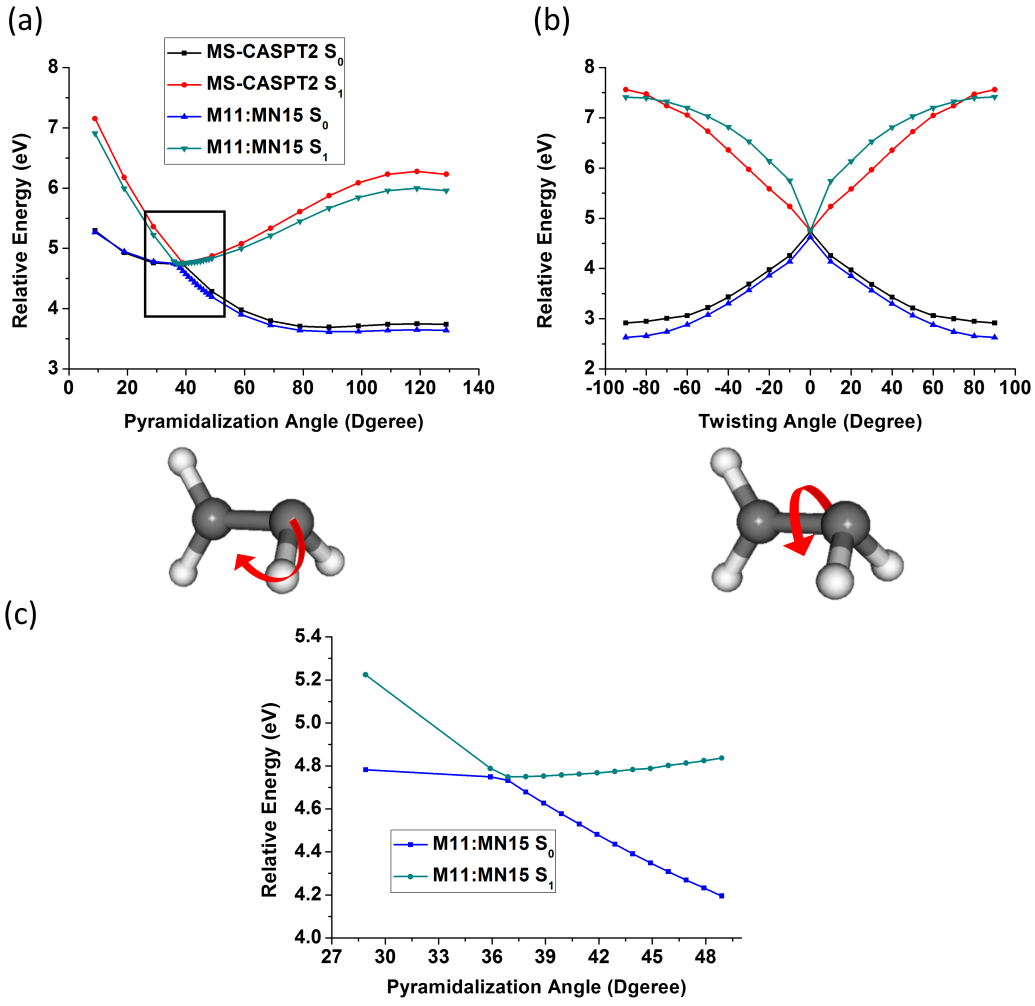

Figure 2.2. The PESs near S_1/S_0 ammonia CI along (a) the pyramidalization angle, (b) twisting angle, and (c) a zoom in of pyramidalization coordinate computed with CASPT2 and DF-TDA

2.5 Conclusions

In summary, we developed a new variant of TDDFT called the dual-functional Tamm-Dancoff approximation or DF-TDA. It is a conceptually simple, easy-to-implement, and black-box method. DF-TDA employs different functionals (F1 and F2) for orbital optimization and for TDA Hamiltonian construction, and hence the coupling between the ground and singly excited states is nonzero. Thus the double cone topology of the PESs

in the vicinity of S_1/S_0 conical intersection is correct. We have shown that the accuracy of DF-TDA is mostly determined by the functional that is used to build the TDA Hamiltonian. The new DF-TDA/F1:F2 has global accuracy comparable with that of KS-TDA/F2; it predicts higher vertical excitation energy – by about 0.1 eV – than does KS-TDA/F2. We also have illustrated how the PESs computed by DF-TDA/M11:MN15 have the correct double cone topology and are generally about as accurate as MS-CASPT2.

3 The DQ and DQΦ electronic structure diabatization methods: Validation for general applications

Reproduced from Chad E. Hoyer, Kelsey Parker, Laura Gagliardi, and Donald G. Truhlar, J. Chem. Phys. **144**, 194101 (2016) with permission of AIP Publishing

Sections 3.1 and 3.2 review the theories behind Boys localization and the dipole, quadrupole (DQ) diabatization methods respectively. Section 2.3 describes the dipole, quadrupole, electrostatic potential (DQΦ) diabatization method (an extension of the DQ method). Section 2.4 describes test cases and Section 2.5 gives results.

3.1 Boys localized diabatization

We express diabatic states, $\{\phi_A\}$, as a linear combination of *n* adiabatic states, $\{\psi_I\}$:

$$\phi_A = \sum_{I=1}^{n} \psi_I T_{IA}, \tag{1}$$

where **T** is an orthogonal transformation matrix that depends on the choice of diabatization method. Therefore the diabatic states span the same space as the adiabatic states, which are sometimes called the Born-Oppenheimer (BO) states.

The Boys localization scheme was originally developed for localizing MOs;[66-67] however, it was recently extended to the localization of polyelectronic states by Subotnik *et al*.[68] This scheme defines the rotation matrix **T** of eq.(1) such that it maximizes the sum of the squares of the dipole moments (so only the magnitude of the dipole is important):

$$f_{Boys} = \sum_{A=1}^{n} |\langle \phi_A | \boldsymbol{\mu} | \phi_A \rangle|^2, \tag{2}$$

$$\boldsymbol{\mu} = \sum_{i=1}^{N_{\mathrm{el}}+N_{\mathrm{nuc}}} q_i \mathbf{r}_i, \tag{3}$$

where *n* and ϕ_A are defined in eq. (1), $\boldsymbol{\mu}$ is the dipole operator, $\mathbf{r}_i$ and q_i are the coordinate and charge of particle *i*, N_{el} is the number of electrons, N_{nuc} is the number of nuclei, and $\langle \phi_A | \boldsymbol{\mu} | \phi_A \rangle$ is the dipole moment of diabatic state *A*. The dipole moment is

independent of origin for a neutral system, and the origin should be should be specified for charged systems. Minimization of eq. (2) is easily accomplished, and the only input required is the adiabatic dipole matrix, with elements $\langle\psi_I|\boldsymbol{\mu}|\psi_J\rangle$. Note that the diagonal elements of this matrix are the adiabatic dipole moments, and the off-diagonal elements are the adiabatic transition dipoles, as used in oscillator strength calculations.

The motivation for eq. (2) is that it is equivalent to maximizing the sum of the squares of the differences in dipole moments of pairs of diabatic states. A prototype for the kind of case for which maximizing the difference in dipole moments produces useful diabatic states is a two-state, two-center system where a charge could be on the left or the right. The adiabatic states might correspond to delocalized charge distributions, but maximizing the difference in dipole moments of the diabatic states corresponds to one diabatic state with the charge on the left and another with the charge on the right. Equation (2) provides a generalization to *n* many-electron states that should be and is successful when the dipole moment is a distinguishing characteristic for the electronic states of interest, but it does not produce useful diabatic states in more general cases.

3.2 Dipole, quadrupole diabatization

The dipole-quadrupole (DQ) diabatization method was developed recently.[3] The DQ method computes a transformation matrix, **T** in (1), by maximizing a linear combination of dipole and quadrupole terms:

$$f_{\mathrm{DQ}} = \sum_{A=1}^{n}\left(|\langle\phi_A|\boldsymbol{\mu}|\phi_A\rangle|^2 + \sum_{j=1}^{N_{\mathrm{Q}}}\alpha_j\left|\langle\phi_A|\mathrm{Q}^{(j)}|\phi_A\rangle\right|^2\right), \tag{4}$$

$$\mathrm{Q}^{(j)} = \sum_{i=1}^{N_{\mathrm{el}}+N_{\mathrm{nuc}}} q_i\left|\mathbf{r}_i - \mathbf{r}_j\right|^2, \tag{5}$$

where N_{Q} is the number of quadruple terms considered, α_j is a parameter that controls the influence of quadrupole term j, and $\mathrm{Q}^{(j)}$ is the traceless quadrupole corresponding to an

origin at $\mathbf{r}_j$. In some cases, we use only one origin, in which case we write α instead of α_j. More generally, α or α_j could be a function of geometry, as long as it is a smooth function.

The DQ function of eq. (4) may be considered a generalization of the Boys localization function in eq. (2); it reduces to it when $\{\alpha_j\}$ are zero. The addition of the quadrupole terms has the advantage of allowing adequate treatment of more general reactions. The DQ method has the same formal advantages as Boys localized diabatization, and the only input data required are the adiabatic dipole matrix, with elements $\langle\psi_I|\boldsymbol{\mu}|\psi_J\rangle$, and the adiabatic quadrupole matrix or matrices, with elements $\langle\psi_I|\mathrm{Q}^{(j)}|\psi_J\rangle$.

3.3 Dipole, quadrupole, electrostatic potential diabatization

We've extend dipole-quadrupole (DQ) diabatization to also include the electronic electrostatic potential (i.e., the electrostatic potential due to the electrons), and we name this method dipole–quadrupole–electrostatic-potential (DQΦ) diabatization. The function that is maximized in DQΦ diabatization is the DQ function in eq. (4) plus an additional summation for the electrostatic potential:

$$f_{\mathrm{DQ}\Phi} = f_{\mathrm{DQ}} + \sum_{A=1}^{n}\sum_{k=1}^{N_\Phi} \beta_k \left|\langle\phi_A|\Phi^{(k)}|\phi_A\rangle\right|^2 \tag{6}$$

$$\Phi^{(k)} = -\sum_{i=1}^{N_{\mathrm{el}}} \frac{e}{|\boldsymbol{r}_i - \boldsymbol{r}_k|} \tag{7}$$

where $N_{\boldsymbol{\Phi}}$ is the number of origins for the electrostatic potential, e is the unit charge, k denotes a choice of origin for the electrostatic potential, $\mathbf{r}_k$ is an origin, and β_k is a

parameter that weights the importance of the electrostatic potential in the diabatization. When N_Φ equals 1, we simply call the parameter β.

We include the nuclear contribution in the dipole and quadrupole terms for convenience since they are usually included in those properties, but we omit it in the electrostatic potential to avoid singularities when the origin is at a nucleus. When all β_j are zero, the method reduces to DQ diabatization. When all α_j are zero, the method is referred to as DΦ diabatization.

3.4 Test Cases

To study the performance of the DQ method as a function of α_j, we consider diatomic hydrides XH where X is Li or Cl. In these cases we use one quadrupole origin, and we place it at the nucleus of atom X. To compare the fourfold way with Boys, DQ, DΦ, and DQΦ diabatization, we consider $(H_2)_2$, O_3, and the reaction Li + HF $\rightarrow$ LiF + H. These three systems have qualitative differences from each other and were used in the original work on the four fold way, which is a diabatization method previously developed in the Truhlar group.[69]

The first two $^1\Sigma^+$ states of HCl and the first four $^1\Sigma^+$ states of LiH were investigated. The adiabatic potential energy curves (V_i, where i = 1–2 for HCl and i = 1–4 for LiH) were computed by state-averaged complete-active-space self-consistent-field[12] calculations averaging over the number n of states of interest, which will be abbreviated SA(n)-CASSCF. In particular, we carried out SA(2)-CASSCF calculations for HCl and SA(4)-CASSCF calculations for LiH with equal weights for each state and with the aug-cc-pVTZ[70] basis set. These calculations were carried out with *Molcas*, version 8.1.[71] The wave function was constrained to have C_{2v} spatial symmetry, and calculations were done in the A_1 irreducible representation. The active space of HCl has eight electrons in five

orbitals, which nominally correspond to $1s_{\mathrm{H}}$, $3s_{\mathrm{Cl}}$, and $3p_{\mathrm{Cl}}$, and it is denoted as CAS(8,5). The active space of LiH has two electrons in nine orbitals, which nominally correspond to $1s_{\mathrm{H}}$, $2s_{\mathrm{Li}}$, $2p_{\mathrm{Li}}$, $3s_{\mathrm{Li}}$, and $3p_{\mathrm{Li}}$; this active space is denoted as CAS(2,9).

For these systems we carried out diabatization by the Boys localized method, by the DQ method with more than one choice of the parameter α, and by the fourfold way. The dipole matrices needed for Boys localization and the DQ method and the quadrupole matrices needed for the DQ method were computed with the RASSI module[72] of *Molcas* 8.1, and the Boys localized diabatization and DQ diabatization were implemented in a locally modified version of *Molcas 8.1*. As already mentioned earlier, the origins for the quadrupole moments were taken as the Cl atom and Li atom, respectively, for HCl and LiH. For the DQ method, we tested three values of α: 0.5, 1.0, and 10.0 a_0^{-2}.

Also included for comparision for these test cases are results from fourfold way diabatization. Fourfold way diabatization is generally successful, but requires orbital analysis that makes the method difficult and time intensive. In the fourfold way calculations, the threefold-density-matrix criterion does not need to be augmented by a reference-orbital overlap term in this case, so the fourfold way reduces to the threefold way for these systems.

For the $(H_2)_2$ system, adiabatic potential energy curves for the first two excited $\sum^+$ states, were computed by SA(*n*)-CASSCF with equal weights for each state and with the TZP basis set[73] in *Molpro 2012.1*.[62-63] The active space was 4 electrons in 4 orbitals corresponding to the 1*s* orbital on each H.

For the Li + FH → LiF + H system, the change along a reaction coordinate, *s*, was defined by

$$\Delta s = \sqrt{\sum_{i=Li,F,H} (\Delta x_i^2 + \Delta y_i^2 + \Delta z_i^2)} \qquad (8)$$

where the summation is over the change in the mass-weighted Cartesian coordinates for the three atoms with the origin of *s* at the saddle point of the lower adiabatic curve. The reactant side was defined by stretching the LiF bond while optimizing the FH bond distance. The product side was defined by stretching the FH bond while optimizing the LiF bond distance. The bond angle was held at 120° for all calculations. The geometries were taken from previous calculations that were performed for the fourfold way diabatization method.[74] The adiabatic ground state ($1^1A'$) and first excited state ($2^1A'$) were calculated with SA(2)-CASSCF in *Molpro 2012.1*[62-63] with the 6-311G++(3*df*,3*pd*) basis set augmented by additional diffuse *s* and *p* functionals with exponents 0.0052(*s*) and 0.0097(*p*) for Li, 0.089(*s*), 0.083(*p*) and 0.000 01(*s*) for F, and 0.037(*s*), 0.012(*s*), and 0.055(*p*) for H.[57, 69, 74-75] The active space was made up of 7 electrons distributed in eight orbitals for the 2*s* and 2*p* orbitals of Li, the 2*p* orbitals of F and the 1*s* orbital of H.

For ozone, the first and second excited singlet states ($1^1A''$ and $2^1A''$ in C_s symmetry) are considered. The calculations were performed in *Molpro 2012.1*[62-63] at the SA(2)-CASSCF/DZP[76] level of theory. The active space has 12 electrons distributed in 9 orbitals corresponding to the 2*p* orbitals for each O.

We performed diabatization with Boys localized method, the DQ method, and the DΦ method. Quadrupole and electrostatic potential origins were put on each atom, except in the case of the LiFH system where calculations were performed with only one quadrupole origin, which was on the Li atom. For all results shown in the paper, the α values were 10 a_0^{-2}, and the β values were 1 a_0. (Note: 1 $a_0 \equiv 1$ bohr = 0.5292 Å.) The dipole and quadrupole matrices were computed with the TRANS and MATROP modules of *Molpro* version 2012.1.[62-63] The electrostatic potential matrices were computed with the MATROP module of *Molpro* version 2012.1. Diabatization was performed with *DQΦpac*.[77]

An additional metric for evaluating a diabatization scheme is the comparison of reference nonadiabatic couplings with nonadiabatic couplings computed from the results of a diabatization calculation. The nonadiabatic couplings were computed via finite difference (DDR) with the DDR module of *Molpro* version 2012.1. [62-63] When computing nonadiabatic couplings from the results of a diabatization scheme, we used the following relationship:[78]

$$f_{12} = \left\langle \psi_1 \middle| \frac{\partial}{\partial \mathbf{R}} \middle| \psi_2 \right\rangle = \frac{1}{V_2 - V_1} \sum_A^n \sum_B^n T_{1A} T_{2B} \frac{\partial}{\partial \mathbf{R}} U_{AB}, \quad (9)$$

where f_{12} is the nonadiabatic coupling between two states of interest. To compute the derivative in eq. (9), we fit the diabatic potential energies and coupling with a simple function (second-order polynomial for $(H_2)_2$ and third-order polynomial for LiFH and O_3) over the one coordinate of interest. For more complicated systems, we recommend fitting with more robust functions.[4] The origin of all DDR calculations was the center of mass.

3.5 Results

3.5.1 HCl

The first two $^1\Sigma^+$ states of HCl provide a prototypical example of an ionic-covalent curve crossing.[79] This ionic–covalent curve crossing provides a case where Boys diabatization might be expected to work well. The ionic diabatic state has a $3s^2_{\mathrm{Cl}}3p^6_{\mathrm{Cl}}$ valence configuration and the covalent state has the valence configuration $1s^1_{\mathrm{H}}3s^2_{\mathrm{Cl}}3p^5_{\mathrm{Cl}}$.

Figure 3.1 reports the adiabatic (V_i) and diabatic (U_i) potential energy curves obtained with (a) the threefold way and (b) Boys localization for the two lowest-energy $^1\Sigma^+$ states of HCl (U_1 corresponds to the ionic state and U_2 to the covalent state). The threefold way results in smooth diabats that agree well with the adiabats away from crossings as seen in Figure 3.1(a). Therefore, we use the threefold way result as a

reference. The Boys curve in Figure 3.1(b) produces the reasonable diabats; however, the diabats at small $\mathbf{R}_{\mathrm{H-Cl}}$ do not match the adiabats well.

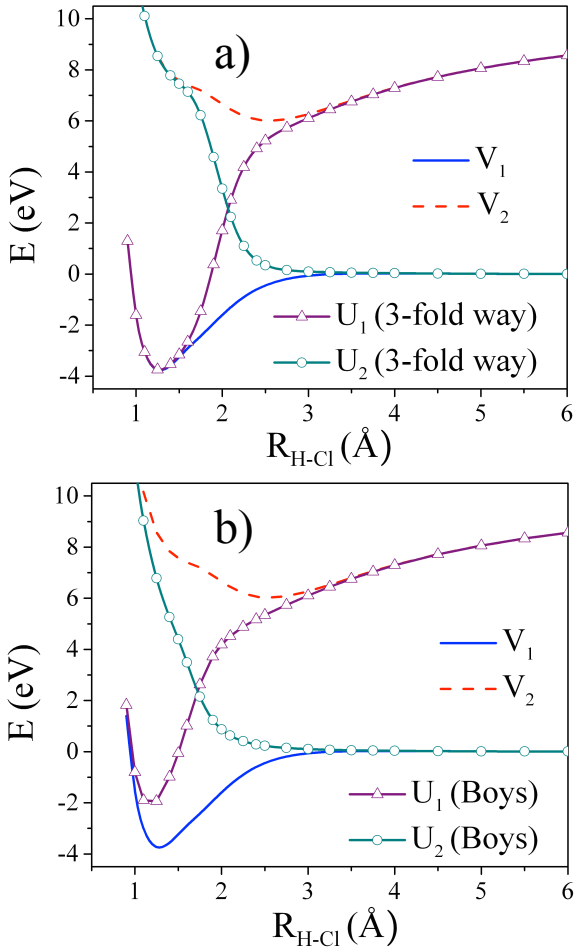

Figure 3.1. Adiabats and diabats of the two lowest-energy $^1\Sigma^+$states for HCl. The diabats were computed with (a) the threefold way and (b) Boys localization.

In Figure 3.2, we show the DQ diabats with (a) $\alpha = 0.5\ a_0^{-2}$,(b) $\alpha = 1.0\ a_0^{-2}$,and (c) $\alpha = 10.0\ a_0^{-2}$ for the two lowest-energy $^1\Sigma^+$ states of HCl. The DQ method with any of these three values of α produces reasonable diabats. For all three values, the diabats agree with the adiabats at small $\mathbf{R}_{\mathrm{H-Cl}}$ better than was observed in the Boys calculations. Inspection of Figure 1(b) and Figure 3.2 shows that addition of the quadrupole improves the matching between diabats and adiabats at small $\mathbf{R}_{\mathrm{H-Cl}}$. Figure 3.2(c) shows that good diabats are obtained even when the diabatization is dominated by the quadrupole, α =

10.0 a_0^{-2}. As for the α-dependence, there is essentially no difference between α = 0.5, 1.0, and 10.0 a_0^{-2}.

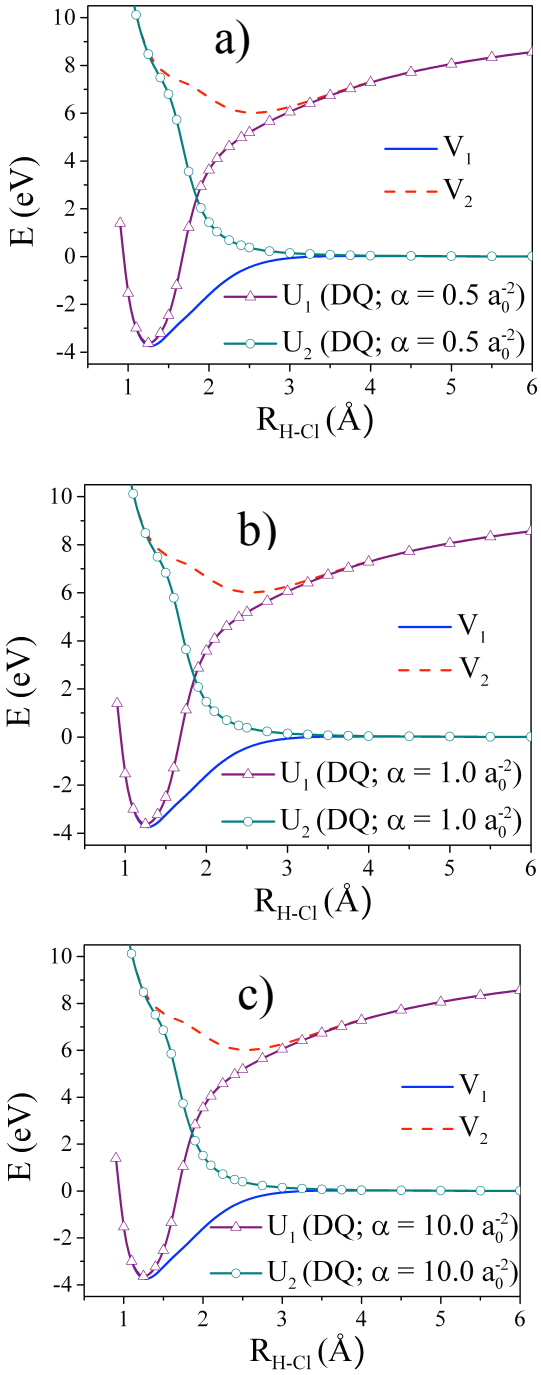

Figure 3.2. Adiabats and diabats of the two lowest-energy $^1\Sigma^+$states for HCl. The diabats are obtained by DQ with (a) $\alpha = 0.5\ a_0^{-2}$, (b) $\alpha = 1.0\ a_0^{-2}$, and (c) $\alpha = 10.0\ a_0^{-2}$.

Figure 3.3 shows the squares of the diabatic couplings (U_{12}) with (a) the threefold way (defined in section II.A) and (b) the Boys localization method, and Figure 4 shows these for the DQ method with α = 0.5 a_0^{-2}, 1.0 a_0^{-2}, and 10.0 a_0^{-2}. The threefold way coupling in Figure 3.3(a) is in qualitative agreement with the DQ results in Figure 3.4 for all three nonzero values of α, and the peak position corresponds to the crossing in Figure 3.2. The qualitative behavior of Boys localized diabatization in Figure 3.3(b) is similar to those of Figures 3.3(a) and 3.4; however, there is a larger coupling than the other methods at small $\mathbf{R}_{\mathrm{H-Cl}}$ (e.g., 1.0 Å), which correlates with the larger adiabat-diabat separation in the potential energy curves at the same distance in Figure 3.1(b). As one increases the value of α, the crossing of the diabats (in Figures 3.1 and 3.2) and peak of the squared diabatic coupling (in Figures 3.3 and 3.4) shift to greater values of $\mathbf{R}_{\mathrm{H-Cl}}$, closer to the threefold way results. A similar behavior was also observed for the 3-state case of LiH previously.[3]

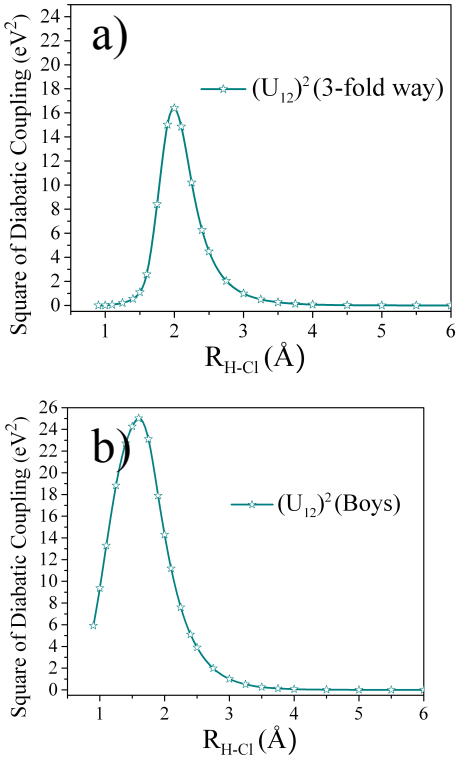

Figure 3.3. Square of the diabatic coupling between the two lowest-energy $^1\Sigma^+$states for HCl. Diabatization was done with (a) the threefold way and (b) Boys localization.

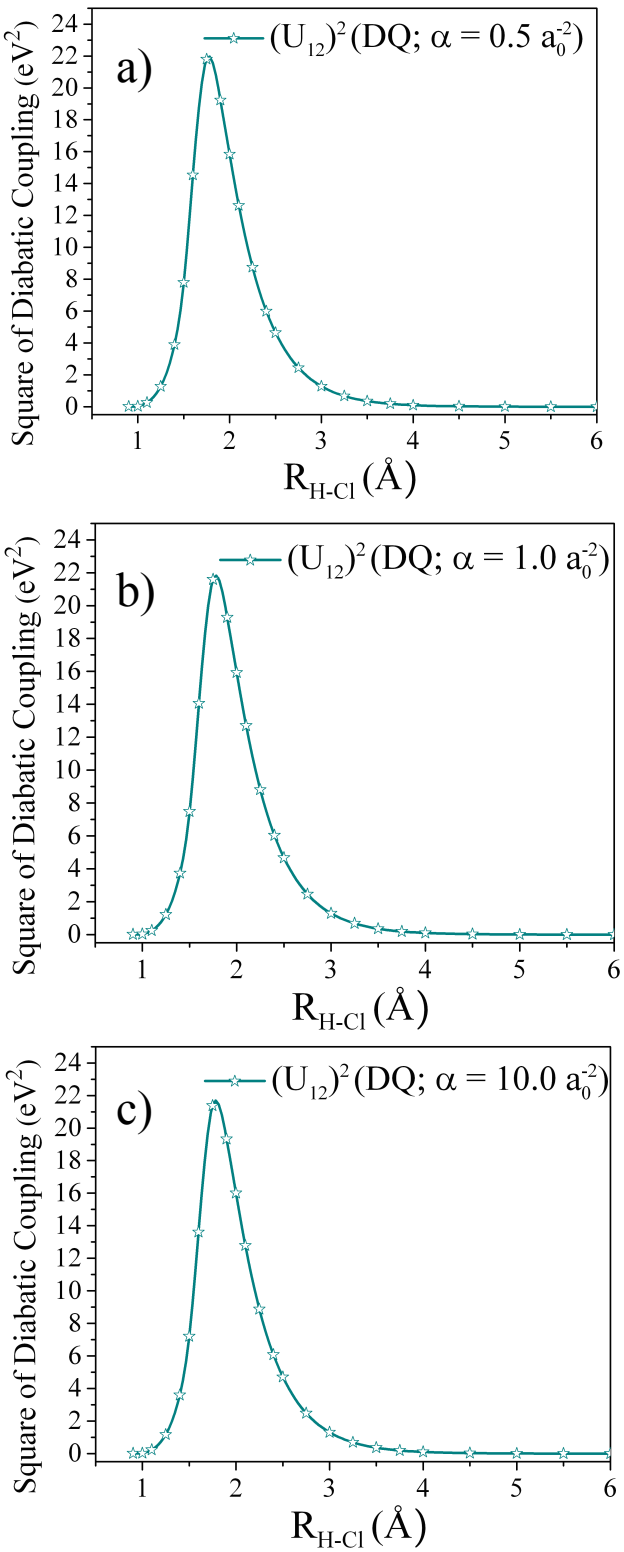

Figure 3.4. Square of the diabatic coupling between the two lowest-energy $^1\Sigma^+$states for HCl. Diabatization was done by DQ with (a) $\alpha = 0.5\ a_0^{-2}$, (b) $\alpha = 1.0\ a_0^{-2}$, and (c) $\alpha = 10.0\ a_0^{-2}$.

3.5.2 LiH

In previous work on DQ diabaitzation,[3] we diabatized the first three $^1\Sigma^+$ states of LiH by using the threefold way, Boys localized diabatization, and the DQ method, each applied to SA(3)-CASSCF(2,5) wave functions. In that study, we determined that Boys localized diabatization was unable to distinguish the covalent $1s_{\mathrm{H}}^1 2s_{\mathrm{Li}}^1$ and $1s_{\mathrm{H}}^1 2p_{\mathrm{Li}}^1$ states at large $\mathbf{R}_{\mathrm{Li-H}}$, the threefold way yielded adequate diabats, and for DQ the only constant value of α to yield adequate diabats was 0.3 a_0^{-2}, and we needed to fit α to a function of geometry to obtain diabats as smooth as the threefold way. This study revealed that the performance of the DQ method is sensitive to the choice of α for LiH.

In this section, we report our new findings for the LiH molecule with SA(4)-CASSCF(2,9) wave functions. We do not report any Boys results for LiH because the Boys localized diabatization fails for LiH with more than two states. The lowest four $^1\Sigma^+$ states of LiH provide a variety of electronic structures as illustrated in in Table 3.1: an ionic state, two covalent states with valence orbitals, and a covalent state involving a Rydberg orbital. The numbering of the diabatic states corresponds to the energetic ordering of the states at the equilibrium geometry.

Table 3.1. Definitions, potential-energy-curve labeling, and valence electronic configurations for the diabatic states of LiH.

Label	Type	Curve	Valence Configuration
ionic	ionic	U_1	$1s_{\mathrm{H}}^2$
covalent sσ	covalent	U_2	$1s_{\mathrm{H}} 2s_{\mathrm{Li}}$
Rydberg	covalent - Rydberg	U_3	$1s_{\mathrm{H}} 3s_{\mathrm{Li}}$
covalent pσ	covalent	U_4	$1s_{\mathrm{H}} 2p_{\mathrm{Li}}$

In Figure 3.5, we report LiH diabats computed with the threefold way. The crossing of the Rydberg and covalent pσ diabatic states between 2-3 Å, the crossing of the ionic and covalent sσ diabatic states between 3-3.5 Å, and the crossing of the ionic and covalent pσ

diabatic states between 4.5-5 Å are all smooth. In addition, the diabats match the adiabats away from crossings. We use the threefold way as reference.

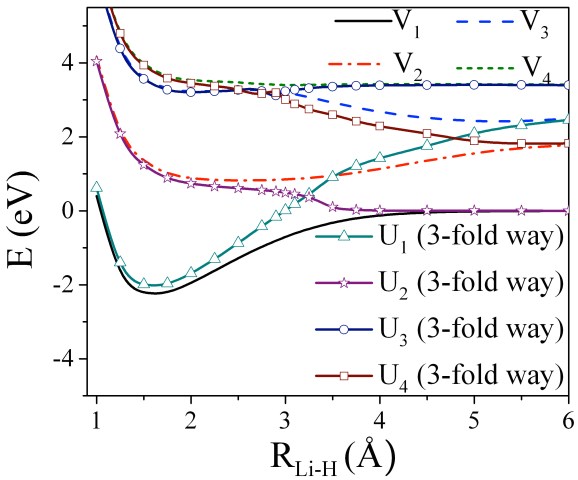

Figure 3.5. Adiabats and diabats of the four lowest-energy $^1\Sigma^+$states for LiH. Diabats were calculated with the threefold way.

We computed diabatic curves with various values of α for DQ as shown in Figure 3.6. All three α values provide smooth crossings of the Rydberg and covalent pσ diabatic states in the 2–3 Å range. This is not surprising since Rydberg states tend to have large values of $\langle \mathbf{r}^2 \rangle$, which can be easily distinguished from the other states. In addition, the crossings of the ionic and covalent pσ diabatic states between 4.5 and 5 Å are smooth. At large $\mathbf{R}_{\mathrm{Li-H}}$, this is due to both the dipole and quadrupole terms. The crossing between the ionic and covalent sσ diabatic states between 2 and 3 Å does show some sensitivity to the α value, and the crossing appears too abrupt with $\alpha = 1.0\ a_0^{-2}$. It is interesting to note the crossings are shifted to slightly larger $\mathbf{R}_{\mathrm{Li-H}}$ as α increases, in better agreement with the threefold way, and the ionic and covalent pσ diabatic state crossings are more strongly coupled by DQ than by the threefold way. For the three values of α shown in Figure 3.6, the DQ method produces diabats that match the adiabats away from crossings.

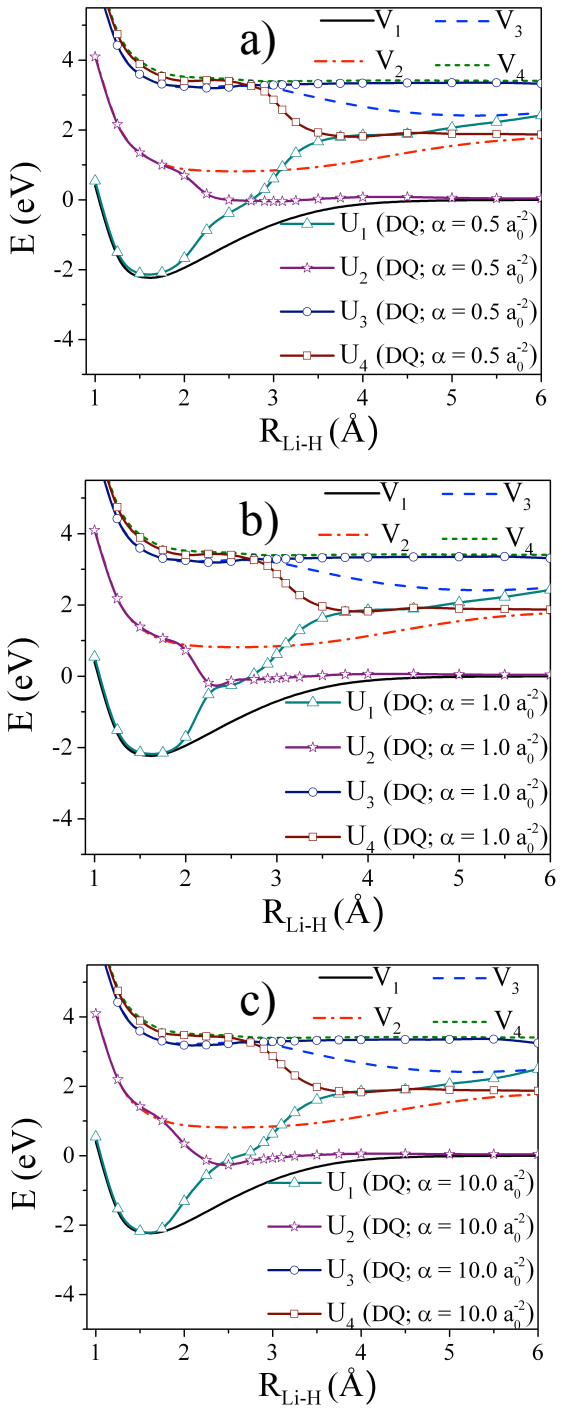

Figure 3.6. Adiabats and diabats of the four lowest-energy $^1\Sigma^+$states for LiH. Diabats are obtained by DQ with (a) $\alpha = 0.5\ a_0^{-2}$, (b) $\alpha = 1.0\ a_0^{-2}$, and (c) $\alpha = 10.0\ a_0^{-2}$.

The squared diabatic couplings for the threefold way are reported in Figure 3.7. The couplings between the covalent states ($(U_{23})^2$, $(U_{24})^2$, and $(U_{34})^2$) are small. The

coupling between the ionic and covalent sσ diabatic states ($(U_{12})^2$) in Figure 3.7(a) is constant until ~3.75 Å, which is soon after the state crossing in Figure 3.5. The ionic–Rydberg coupling, ($(U_{13})^2$), does not have a simple interpretation based on Figure 3.5. The ionic– covalent pσ coupling, $(U_{14})^2$, is strong from about 1 to 5 Å. The region after 5 Å corresponds to the region after any crossing. A noticeable feature in Figure 7 is the local minimum at 3 Å. This seems to correlate with the unexpected peak in the squared coupling between the ionic and Rydberg states at 3.0 Å in Figure 3.7(a). This may be due to the extensive configuration mixing between the ionic, Rydberg, and covalent pσ state.

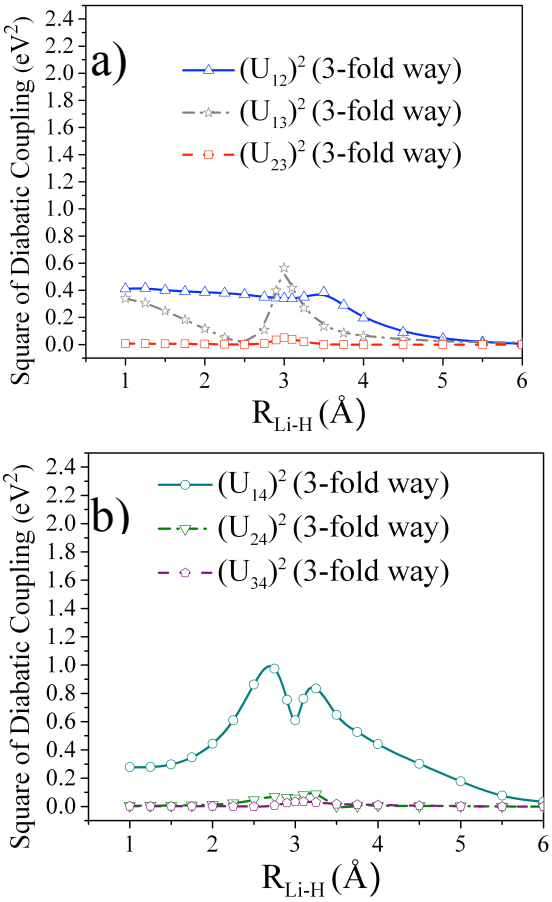

Figure 3.7. Square of the diabatic couplings between the four lowest-energy $^1\Sigma^+$states for LiH. The diabatic states were computed with the threefold way.

The squared diabatic couplings with the DQ method can be found in Figures 3.8, 3.9, and 3.10 for α = 0.5, 1.0, and 10.0 a_0^{-2}, respectively. There is little qualitative difference in the squared diabatic coupling between these figures, so we will only discuss Figure 3.10. The very large peak in $(U_{12})^2$ in Figure 3.10(a) correlates very well with the crossing of the ionic and covalent sσ diabatic states in Figure 3.6(c). The peak in $(U_{14})^2$ in Figure 3.10(b) also occurs at the same location as the crossing of the ionic and covalent pσ diabatic states in Figure 3.6(c).

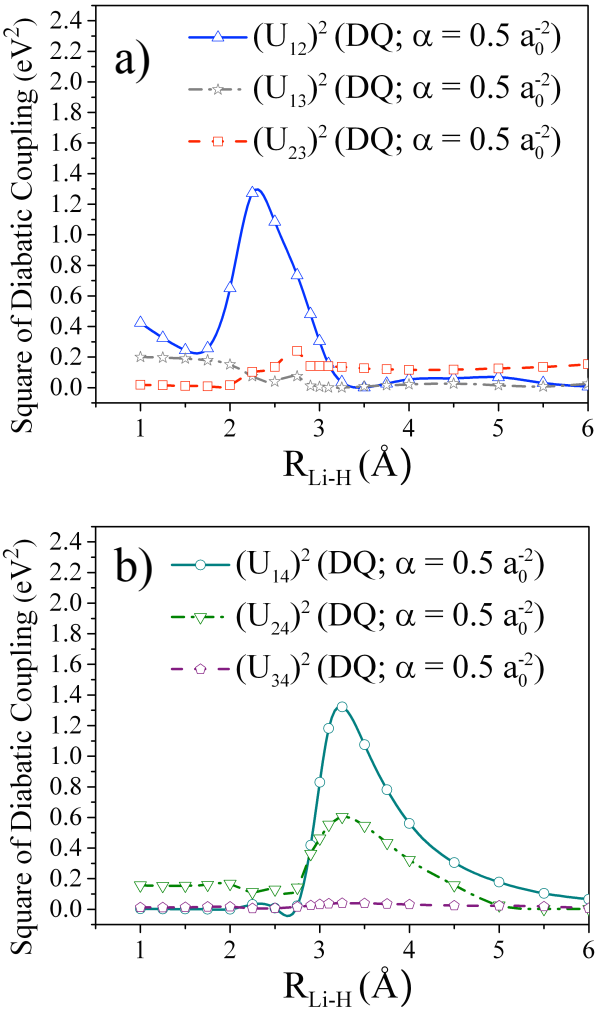

Figure 3.8. Square of the diabatic couplings between the four lowest-energy $^1\Sigma^+$states for LiH. The diabatic states were computed with DQ with $\alpha = 0.5\ a_0^{-2}$.

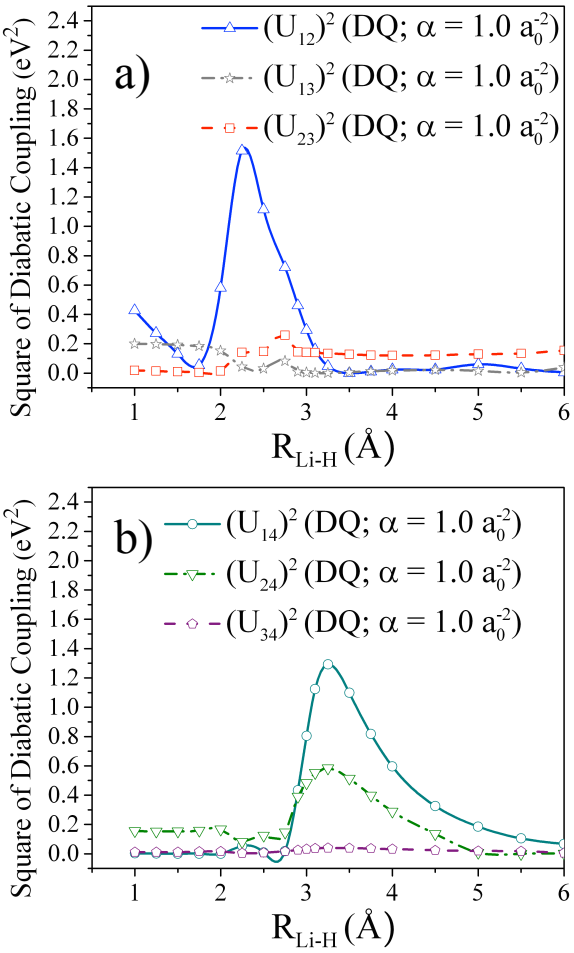

Figure 3.9. Square of the diabatic couplings between the four lowest-energy $^1\Sigma^+$states for LiH. The diabatic states were computed with DQ with $\alpha = 1.0\ a_0^{-2}$.

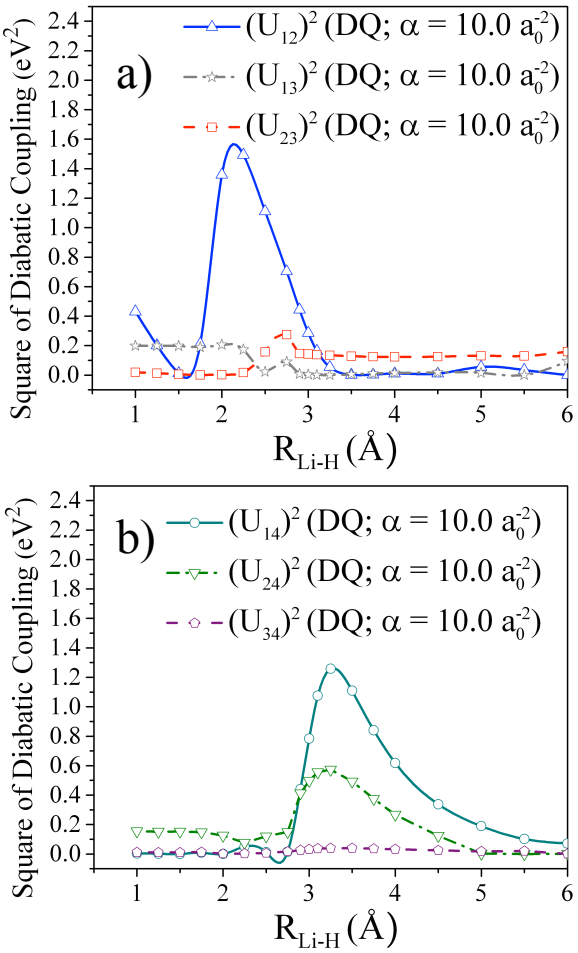

Figure 3.10. Square of the diabatic couplings between the four lowest-energy $^1\Sigma^+$states for LiH. The diabatic states were computed with DQ with $\alpha = 10\ a_0^{-2}$.

A large value of α (10 a_0^{-2}) produced smooth diabats for LiH, unlike our previous work on this molecule summarized above. This is due to the addition of the fourth state in the diabatization. Our previous work used three states, where the third state was Rydberg at small $\mathbf{R}_{\mathrm{Li-H}}$ and covalent pσ at large $\mathbf{R}_{\mathrm{Li-H}}$ (we labeled it as the covalent pσ state ($1s_{\mathrm{H}}2p_{\mathrm{Li}}$) due to its character at large $\mathbf{R}_{\mathrm{Li-H}}$)**.** The abrupt change in electronic character resulted in difficulties in finding a good constant value for DQ. However, in this work, we explicitly included a fourth state, which resulted in the relative ease of diabatization. The situation here is similar in some respects to what we found in our previous paper for phenol, where we could compare to recent work[80] with the fourfold way. For phenol,

Boys localized diabatization did not yield useful diabats; however, DQ with a constant value of 10 a_0^{-2} produced diabats that matched the fourfold way quite well. We conclude from our findings that if the diabatic potential curves have a consistent electronic structure at all **R**, then the choice of α can be simple (for example, 10 a_0^{-2} worked well in this work and in our previous work). However, if the highest-energy potential curve changes character (as in our previous work on LiH), then finding an α that yields good diabats may not be straightforward.

The comparison of our three-state and four-state treatments of LiH illustrates an important general point. For general polyatomics there is no symmetry, and the first adiabatic state somewhere intersects the second, the second intersects the third, the third intersects the fourth, and so forth. On one side of that third state - fourth state intersection, the third adiabatic state may be dominated, for example, by the third diabat, and on the other side it is dominated by the fourth diabat. Thus an accurate global treatment of the three lowest adiabats requires four diabats. We get the fourth diabat by calculating four adiabats, but the fourth adiabat intersects the fifth, and so now we need five diabats. The pattern continues, but eventually the new intersections introduced by bringing in more adiabats occur at high enough energy that we need not treat them accurately. Thus, for example, if the intersection of the third and fourth adiabat occurs at low enough energy to be important in the dynamics of interest, we should include four states, but if it occurs at higher energy, we can probably get by with three because it is not necessary to treat the third adiabat accurately for all geometries. Note, however, that a poorly treated high-energy intersection of the last included state can cause a little unsmoothness in the lower diabats because the orthogonality constraints on the rows and columns of the orthonormal adiabatic-to-diabatic transformation matrix mean that the representation of each state has an effect on the representation of every other state. The extent of such unsmoothness, if any, is expected to be highly system dependent. It can be

avoided to a large extent in the fourfold way by using an expanded diabatic prototype list for the last state.

3.5.3 $(H_2)_2$

In this section, we report our findings for Boys localized, DQ, and DΦ diabatization for H_2 dimer, and we compare the results to previously calculated[69] fourfold way results. The two hydrogen molecules are collinear with the centers of mass of the molecules always separated by 10 a_0. One molecule is referred to as A and the other as B. Molecule A has a bond length of $r - \Delta r$, and B has a bond length of $r + \Delta r$ where r is 1.5 a_0 and $\Delta\mathbf{r}$ ranges from -0.2 to 0.2 a_0. The first two $^1\Sigma^+$ excited states of $(H_2)_2$ show an avoided crossing due to the symmetry of the reaction coordinate. The first adiabatic excited state corresponds to excitation of a σ MO to a σ* MO on the compressed molecule. The second adiabatic excited state is a σ-to-σ* excitation of the stretched molecule. The roles of the molecules A and B change over the $\Delta\mathbf{r}$ reaction coordinate, which results in the avoided crossing of the adiabatic states, which are labeled V_2 and V_3 in Figure 3.11.

Previously, the threefold way was successful for diabatization with DMOs localized on molecules A and B.[69] The threefold-way results meet our criteria of good diabatic curves by being smooth and matching the adiabatic curves away from crossings. Figure 3.11 shows the results from Boys localized, DQ, and DΦ diabatization. For the DQ method, each H was used as an origin and all α_j values are 10 a_0^{-2}. For the DΦ method, each H was used as an origin and all β_j values are 1 a_0. Results from the Boys localized method are shown in Figure 3.11(a). The diabatic curves cross at zero as expected, but away from the avoided crossing, the diabatic curves diverge from the adiabatic curves. Addition of the quadrupole or electrostatic potential changes this behavior, as shown in Figures 3.11(b) and 3.11(c), respectively. The diabatic curves now more closely resemble

the adiabatic curves in regions further away from the avoided crossing. Both DQ and DΦ results show an improvement over using the dipole alone.

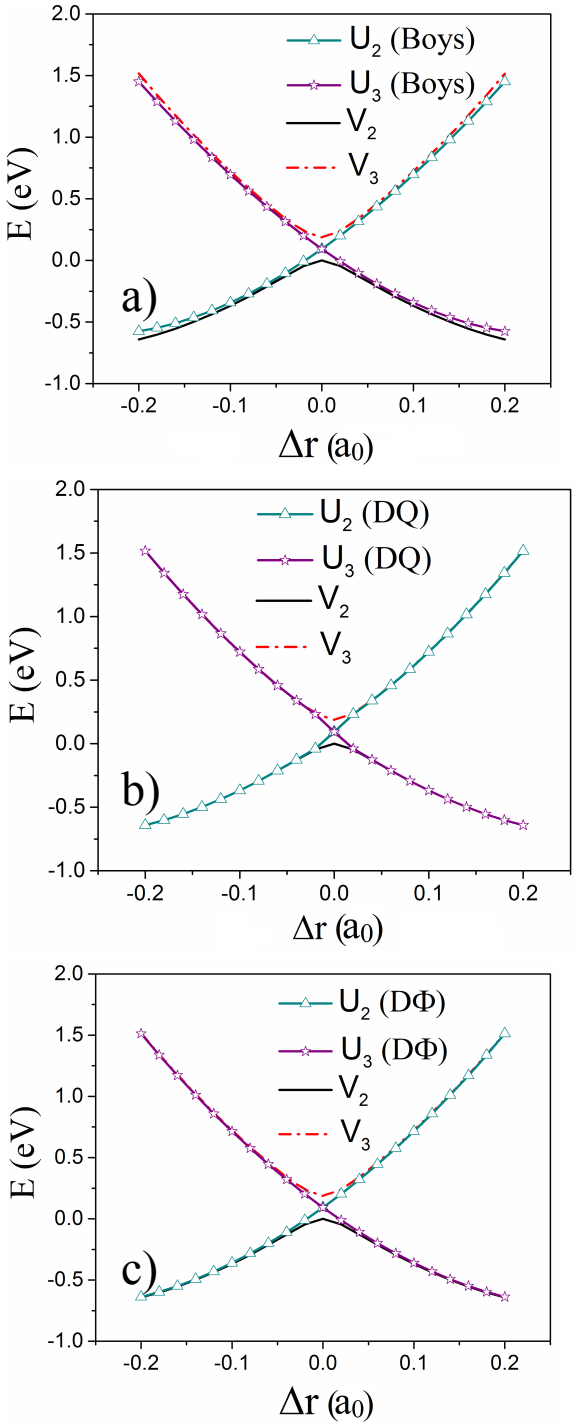

Figure 3.11. Adiabats and diabats of the two lowest-energy $^1\Sigma^+$excited states for $(H_2)_2$. Diabats were calculated with the (a) Boys method, (b) DQ method with an origin on each H with $\alpha_j = 10\ a_0^{-2}$, and (c) DΦ with an origin on each H with $\beta_j = 1\ a_0$.

The squared diabatic couplings for the three methods are shown in Figure 3.12. The Boys results have a minimum at $\Delta\mathbf{r} = 0$ and increase as $|\Delta\mathbf{r}|$ increases, which agrees with the finding that the diabatic curves diverge from the adiabatic curves away from the avoided crossing. The DQ and DΦ graphs are an order of magnitude smaller and there is a peak at the avoided crossing. The curves decrease as $|\Delta\mathbf{r}|$ increases.

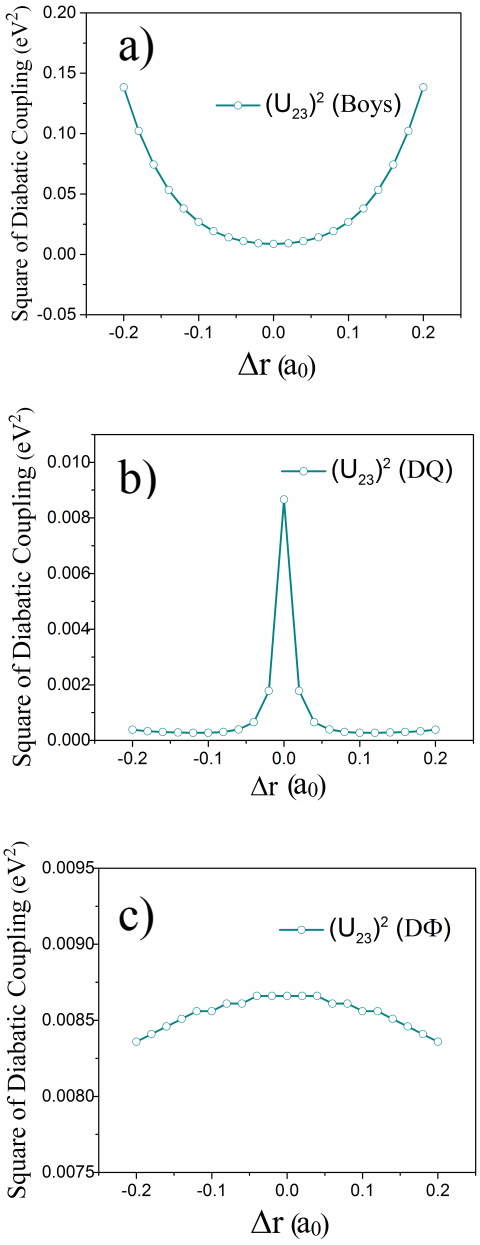

Figure 3.12. Square of the diabatic coupling between the two lowest-energy $^1\Sigma^+$states for $(H_2)_2$ computed with (a) Boys method, (b) DQ with an origin on each H and $\alpha = 10.0\ a_0^{-2}$, and (c) DΦ with an origin on each H and $\beta = 1.0\ a_0$.

We also compare the DDR nonadiabatic coupling with the nonadiabatic coupling computed with Boys, DQ, and DΦ diabatization method results in Figure 3.13. The DDR and DΦ completely overlap, indicating excellent performance of the diabatization method. The DQ results match the DDR results from Δr of -0.20 to -0.15 and 0.15 to 0.20 a_0; however, the DQ results match less well at other values of Δr. The Boys results match the DDR results well at positive Δr but differ at negative Δr. All three diabatization methods have a qualitatively correct shape of $|f_{12}|$.

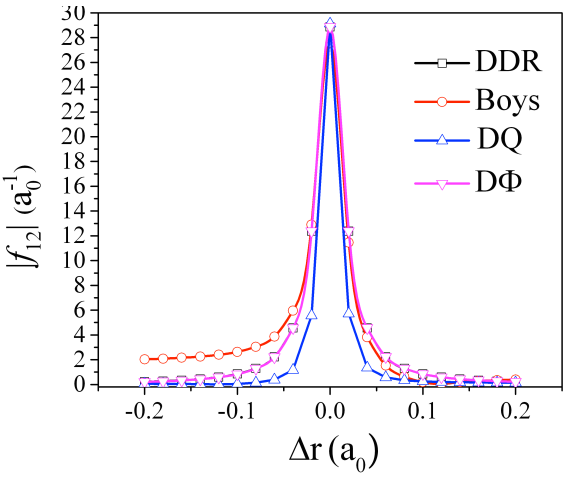

Figure 3.13. Absolute value of the nonadiabatic coupling for the two lowest-energy $^1\Sigma^+$states for $(H_2)_2$. The coupling was computed with direct differentiation (DDR), Boys, DQ with an origin on each H and $\alpha = 10.0\ a_0^{-2}$, and DΦ with an origin on each H and $\beta = 1.0\ a_0$.

The Boys localized method is not as satisfactory as DQ or DΦ for diabatization of the $(H_2)_2$ system. The addition of the electrostatic potential, like the addition of the quadrupole, shows an improvement in differentiating diabatic states in this case. The nonadiabatic coupling results indicate that DΦ is an excellent diabatization method for this system.

3.5.4 LiFH

The LiFH system involves a reaction: Li(^{2}S, ^{2}P) + FH → LiF + H. In the reactant region, the two lowest adiabatic potential energy surfaces (1^1A′, 2^1A′) correspond to Li being in S and P states respectively. In the products region, the ground state has a singly occupied H(1*s*) orbital and the high energy first excited state shows electron donation from an in-plane lone pair on F to the H atom. Previous results of the fourfold way show diabatization was possible with this method by using a reference orbital.[69, 74] In order to obtain diabats that smoothly change from the reactant region to the product region, it was necessary to identify and choose appropriate reactant and product CSF groups as diabatic prototypes.

Figure 3.14(a) shows Boys localized results. The 2^1A′ curve is off-scale in the product region due to its very high energy. In the product region, the Boys localized results do differentiate between the diabatic states, but Boys diabatization fails in the reactant region, where it cannot differentiate the S and P states of the ground and first excited state of Li. These results are similar to what we saw for the diatomic hydrides where the addition of the quadrupole was found to improve the diabatization. Figure 14(b) shows the results from using the quadrupole with an origin on the Li atom and an α value of 10 a_0^{-2}. The reactant region now shows diabatic curves that approach the adiabatic curves, similar to fourfold way results.

Adding the electrostatic potential to the DQ method to give the DQΦ method shows a slight smoothing of the diabatic curves around s = 0 as shown in Figure 3.14(c). For these calculations, the quadrupole parameters are the same as for the previously described DQ calculations and the electrostatic potential parameters are: an origin on each atom and each β_j value set equal to 1 a_0. Taking out the quadrupole to give DΦ diabats was found to be unsuccessful in a similar way to the failure of the Boys localized calculations.

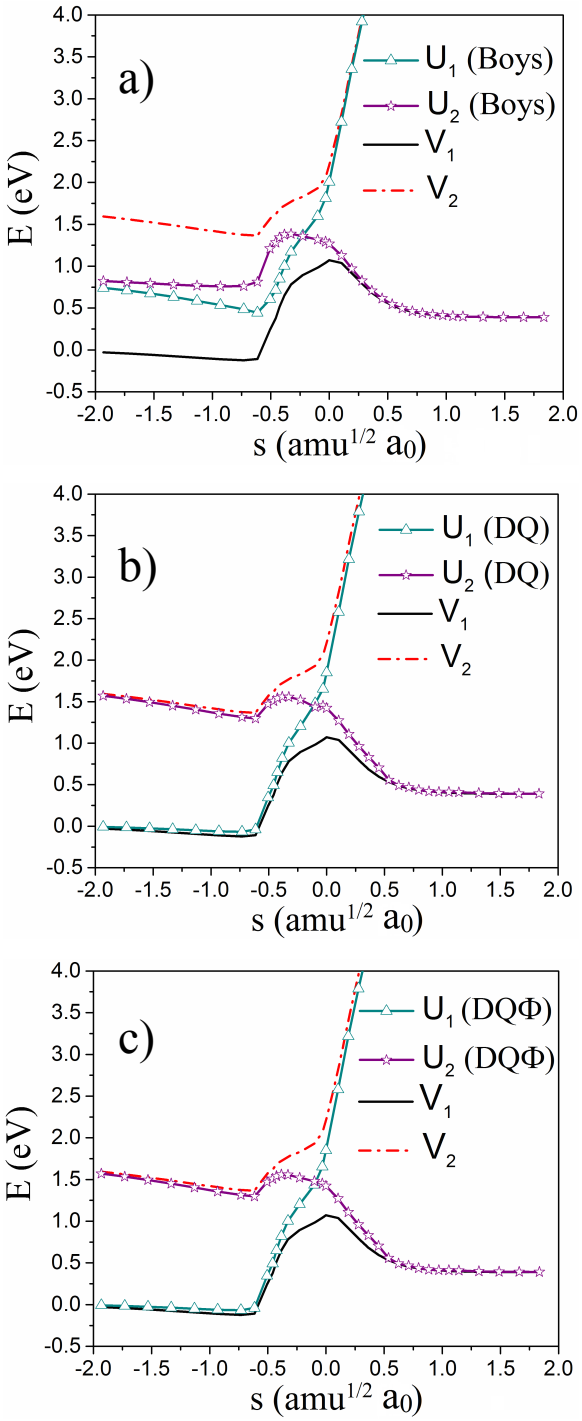

Figure 3.14. Adiabats and diabats of the two lowest 1^1 A′ and 2^1 A′ states for LiFH. Diabatization was performed by (a) Boys method, (b) DQ with an origin on Li and $\alpha = 10.0\ a_0^{-2}$, and (c) DQΦ with a quadrupole origin on Li and $\alpha = 10\ a_0^{-2}$ and electrostatic potential origins on all three atoms and $\beta_j = 1\ a_0$.

Figure 3.15 shows the square of the diabatic coupling. The DQ and DQΦ results are essentially identical. In both plots, there is a peak near s = 0.4 a_0 $amu^{1/2}$.

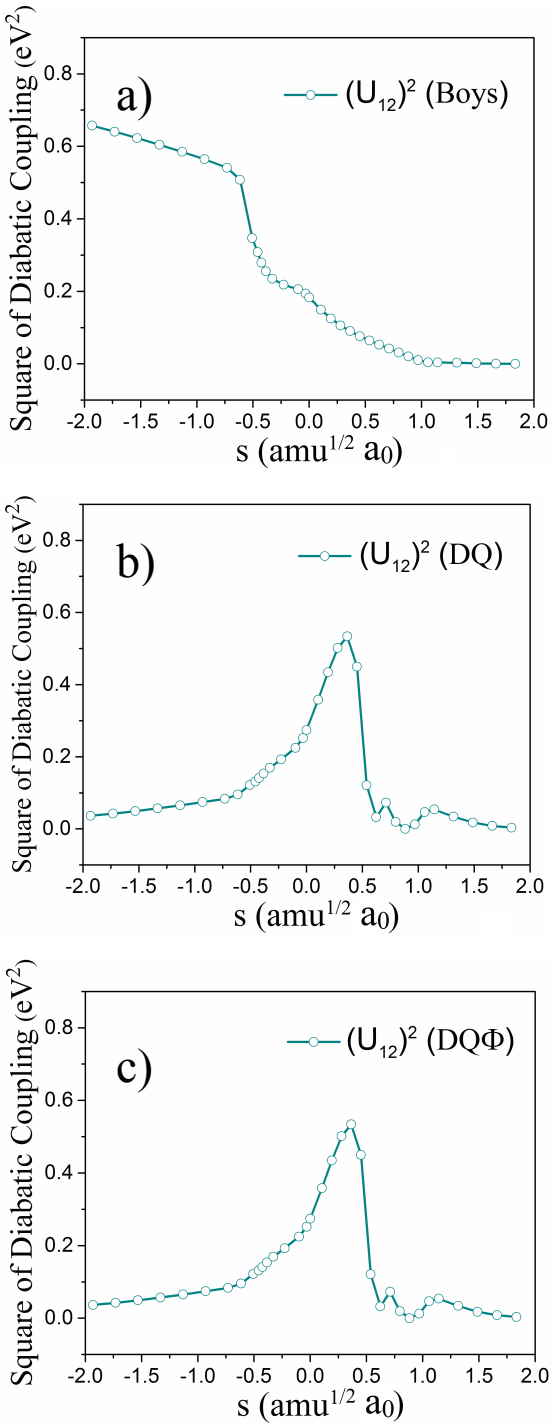

Figure 3.15. Square of the diabatic coupling of the two lowest 1^1 A′ and 2^1 A′ states for LiFH. The diabatic states were computed with (a) the Boys method, ((b) the DQ with an origin on Li and $\alpha = 10.0\ a_0^{-2}$, and (c) the DQΦ with a quadrupole origin on Li and $\alpha = 10\ a_0^{-2}$ and with electrostatic potential origins on all three atoms and all $\beta_j = 1\ a_0$.

The absolute values of the nonadiabatic couplings for LiFH are shown in Figure 3.16. We only focused on the region where the adiabatic states are close in energy to avoid difficulties with fitting. All three diabatization methods do not produce nonadiabatic couplings that qualitatively match the DDR results; the peak maximum differs by 0.5 a_0 $amu^{1/2}$ between the DDR and diabatization results. From -2.0 to -1.0 a_0 $amu^{1/2}$, the DQ and DQΦ couplings match the DDR results. The Boys coupling has regions that increase in magnitude, correlating with the strong state mixing that occurs in Figures 3.14(a) and 3.15(a). The peak magnitude of the DQΦ coupling best matches the DDR magnitude, and the Boys and DQ couplings have similar peak magnitude. The more correct peak magnitude of DQΦ seems correlated to the smoother crossing in Figure 3.14(c) when compared to Figures 3.14(a) and 3.14(b).

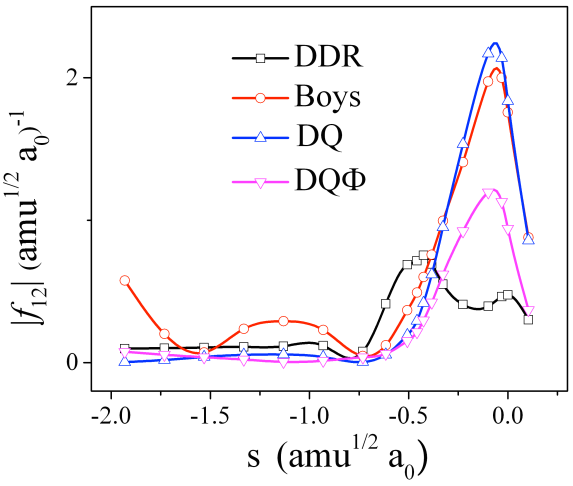

Figure 3.16. Nonadiabatic couplings of the two lowest 1^1 A′ and 2^1 A′ states for LiFH. The couplings were computed by finite difference (DDR), the Boys method, the DQ with an origin on Li and $\alpha = 10.0\ a_0^{-2}$, and DQΦ with a quadrupole origin on Li and $\alpha = 10\ a_0^{-2}$ and with electrostatic potential origins on all three atoms and all $\beta_j = 1\ a_0$.

In summary, similarly to what was shown for the diatomic hydrides, the DQ method worked with an origin on Li and an α value of 10 a_0^{-2}. The addition of the electrostatic potential in the DQΦ method improved the smoothness and produces a better

nonadiabatic coupling. The diabatic curves are similar to the fourfold way curves, but the DQΦ method does not require a reference orbital or a prototype CSF list.

3.5.5 O_3

In this section we report on Boys localized, DQ, and DΦ diabatization of the first and second singlet states of O_3. The geometries considered for ozone have the bond angle held first at 120° and one bond length held at 2.7 a_0. The other bond length, called *r*, is varied in the range 2.0 – 3.3 a_0. With the bond angle held at 120°, the results are compared with previous fourfold way results. The angle is then changed to 100°, and the results are compared between Boys localized, DQ, and DΦ diabatization.

The first two 1^1 A″ and 2^1 A″ singlet states of an asymmetrical ozone stretch have an avoided crossing when held at 120° . The adiabatic states are shown in Figure 3.17 where the two states are labeled V_1 and V_2. In this figure, the two adiabatic states are largely hidden by the diabatic states, which are nearly identical to the adiabatic states. The diabatic states cross while the adiabatic states do not cross, as V_1 is always lower than V_2. The diabatic states are discussed in greater detail below. We refer to the center oxygen as O1, the oxygen with a variable bond length with O1 is referred to as O2, and the final oxygen that stays a constant distance from O1 is labeled O3.

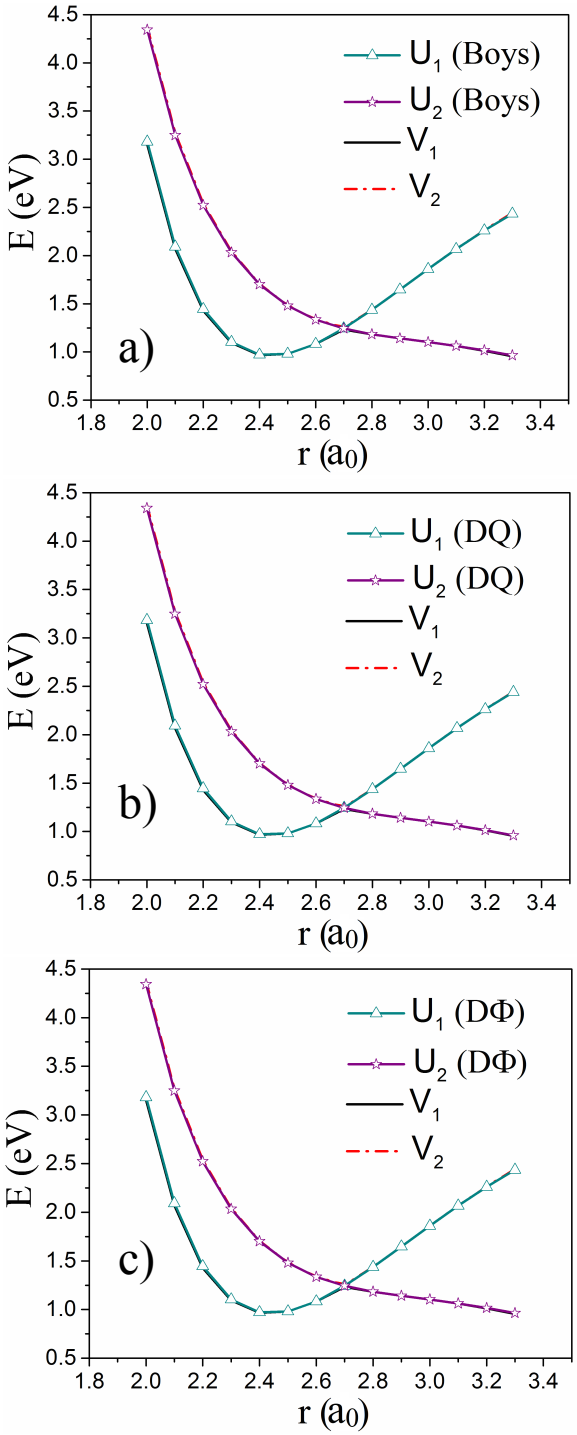

Figure 3.17. Adiabats and diabats of the two lowest 1^1 A″ and 2^1 A″ states of O_3 held at 120° bond angle. Diabats were calculated with (a) Boys method, (b) DQ with an origin on each O and all $\alpha_j = 10.0\ a_0^{-2}$, and (c) DΦ with an origin on each O and and all $\beta_j = 1\ a_0$.

For both adiabatic states, O2-O1 and O3-O1 σ MOs are doubly occupied and O2 and O3 have a nonbonding p orbital in the plane of the molecule. Out of the plane, O1 has a π

bond with the closer oxygen and the further oxygen has a doubly occupied nonbonding *p* orbital. The final electron is in an out of plane singly occupied orbital with π* character.

The characters of the first and second excited singlet states depend on which of the two O–O bonds is short and which is long. The oxygen closer to O1 has a doubly occupied nonbonding orbital in the first excited state and is singly occupied in the second excited state. The oxygen further from O1 has a singly occupied nonbonding orbital in the first excited state, and this orbital is doubly occupied in the second excited state. As a consequence the adiabats already have some localized charge character. The roles of O2 and O3 change along the coordinate path, giving rise to the avoided crossing of the adiabatic states.

As noted above, the diabatic states calculated with just the dipole are nearly identical to the adiabatic states, but show a curve crossing at $r = 2.7\ a_0$ as shown in Figure 3.17(a). The results indicate that maximizing the difference in the dipole moment of the diabatic states gives essentially the same states as the adiabatic states except that the states cross where the adiabatic states avoid, which eliminates the cusp-like behavior in the adiabats at the avoided crossing. As discussed in the previous paragraph, the two adiabatic states have a large charge separation. Therefore the diabats produced by Boys localization are reasonable, and we judge the method to be successful. The fourfold way, whose results were presented previously,[69] is also successful in removing the cusp-like behavior of the adiabats, but the diabats are quite different; in particular, they cross at much smaller *r*, and they do not tend to the adiabats over the domain of the plot.

Thus we find that both diabatization schemes (fourfold way and Boys) produce smooth diabats, but they are quite different. This raises the issue of whether one of the diabatizations is to be preferred. The wave function is the same in the adiabatic and diabatic representations, if one does not make approximations, and one has the freedom to take the (nonunique) diabatic states to be the same as the adiabatic ones far from the

intersections (which we usually try to do because it is convenient). From this point of view, the Boys result would be preferred. This illustrates the issue that, although the non-uniqueness of diabatic representations is a disadvantage from some points of view, it also has advantages that we can use. Along these lines, it is relevant to keep in mind a result obtained in previous work.[81] In particular, we showed that the residual nuclear momentum coupling and nuclear kinetic energy coupling in a diabatic representation are in general of the same order of magnitude as nuclear momentum coupling and nuclear kinetic energy coupling in the adiabatic approximation, except that the singularities and large values at and near conical intersections are no longer present (if the *n* adiabatic states under consideration are well separated from the higher states). Thus one can find diabatic representations that reduce the coupling everywhere to a level comparable to the nonadiabatic coupling that occurs in the adiabatic representation in regions where the Born-Oppenheimer approximation is a good approximation. The analysis also shows that[81] "one cannot do systematically better than this, i.e., there is no privileged representation in which aside from considerations specific to a particular molecular system, the coupling is systematically smaller than the normal BO breakdown terms.... Furthermore, it means that all nonadiabatic (i.e., diabatic, quasi-diabatic) representations are equally formally justified, provided that they remove the singularities in the adiabatic representation, and one may choose between them on the basis of convenience for a specific application or aptness for a particular molecular situation." This justifies our preference for the Boys diabatization in this case, even though both diabatization methods are successful.

We also carried out DQ calculations with a quadrupole origin on each atom ($N_Q = 3$) and with each α_j set to 10 a_0^{-2}. Finally we carried out DΦ calculations in which the electrostatic origin is on each atom, and each β_j value is set to 1 a_0. The DQ and DΦ

diabatic potentials are shown in Figures 3.17(b) and 3.17(c) and are approximately the same as the Boys localized results, which is encouraging.

The squared diabatic coupling of Boys diabatic states and DQ diabatic states are shown in Figure 3.18. The scale of the plot is small because the adiabatic states are nearly identical to the diabatic states, but the couplings, despite their small size, are smooth, which is further encouraging.

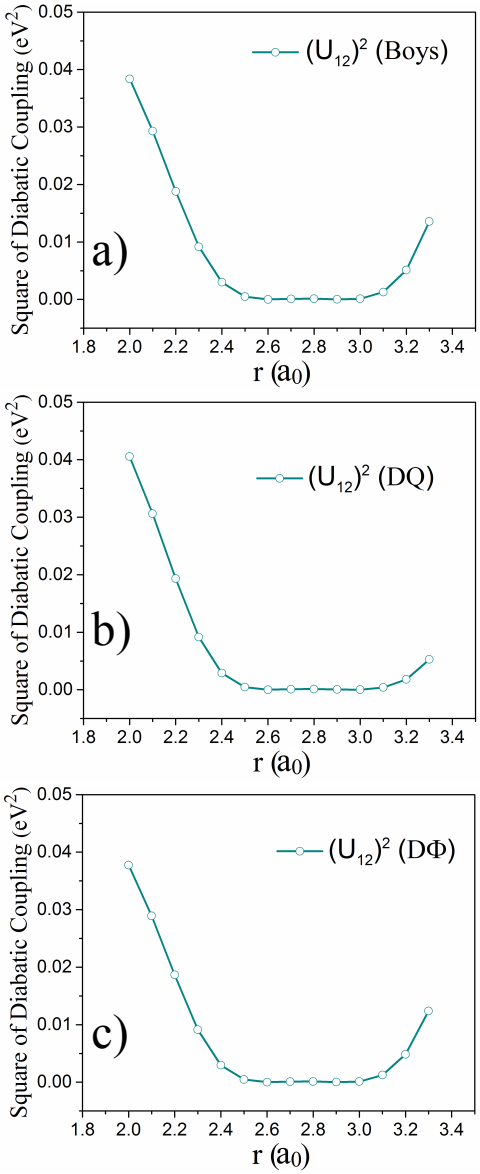

Figure 3.18. Square of the diabatic coupling of the two lowest 1^1 A″ and 2^1 A″ states of O_3 held at 120° bond angle. The diabatic states were computed with (a) Boys method, b) DQ with an origin on each O and all $\alpha_j = 10.0\ a_0^{-2}$, and (c) DΦ with an origin on each O and all $\beta_j = 1.0\ a_0$.

The nonadiabatic coupling computed with finite difference, Boys, DQ, and DΦ are reported in Figure 3.19. There is little difference between the nonadiabatic couplings computed from the three diabatization methods. There is little qualitative difference of all three diabatization methods and the finite difference result; however, the magnitude of the peaks at 2.7 a_0 differs greatly from the finite difference result (a factor of 3). This region is near the conical intersection, possibly indicating a difficulty in describing strongly-interacting states.

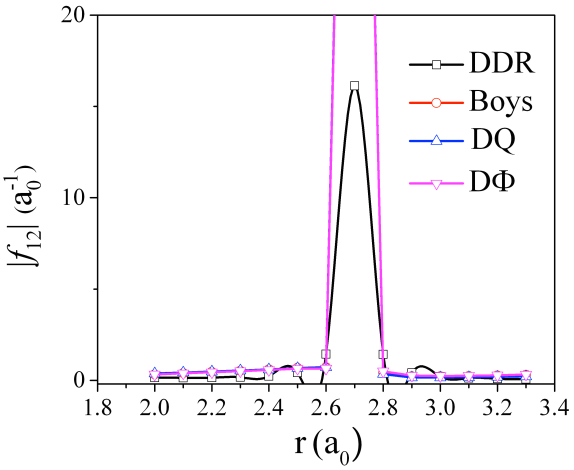

Figure 3.19. Absolute value of the nonadiabatic coupling of the two lowest 1^1 A″ and 2^1 A″ states of O_3 held at 120° bond angle. The coupling was computed with finite difference (DDR), Boys method, DQ with an origin on each O and all $\alpha_j = 10.0$ a_0^{-2}, and DΦ with an origin on each O and all $\beta_j = 1.0$ a_0. All diabatization methods are overlapping.

The first two singlet states were also analyzed with the bond at 100° and the results are in Figure 3.20. This region of the surface is further from the conical intersection and the two adiabatic states, V_1 and V_2, show a larger separation near **r** = 2.7 a_0. Boys localized and DQ method results are in Figures 20(a) and 20(b), respectively. For the DQ calculations, the α_j value is 10 a_0^{-2} and an origin is on all atoms. The Boys localized and DQ plots are nearly identical; the addition of the quadrupole does not make any significant improvements. We see that the diabatic potentials cross, and the diabatic states again

approach the adiabatic states as the stretch increases, which, can be taken as criteria for successful and convenient diabatizations. Figure 3.20(c) shows DΦ results with an origin on each O and all β_j values equal to 1 a_0. These diabats are slightly smoother than the Boys diabats near the diabatic curve crossing.

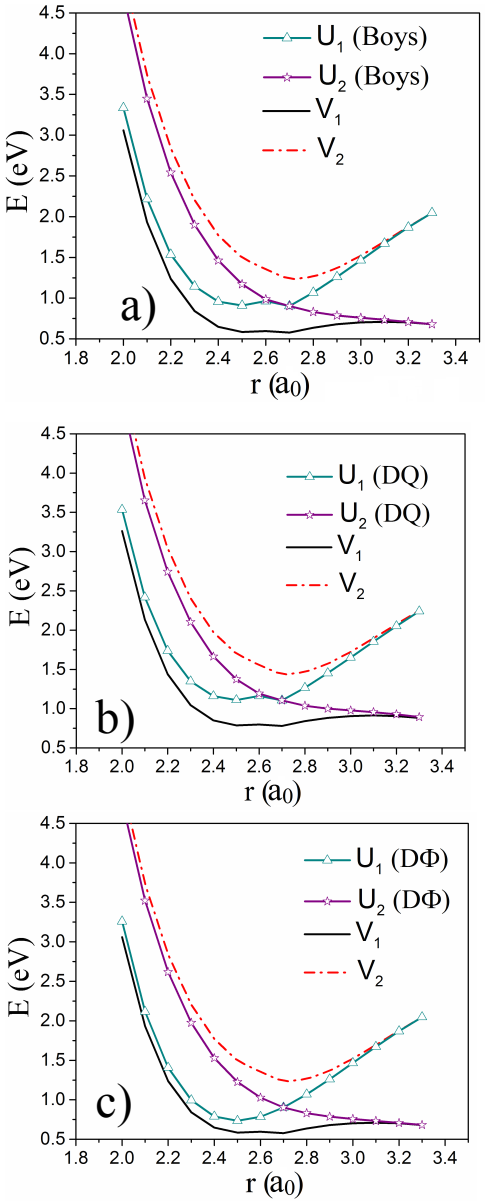

Figure 3.20. Adiabats and diabats of the two lowest 1^1 A″ and 2^1 A″ states of O_3 at 100°. Diabatization was done by (a) the Boys method, (b) DQ with an origin on each O and all $\alpha_j = 10.0\ a_0^{-2}$, and (c) DΦ with electrostatic potential origins on each O and all $\beta_j = 1.0\ a_0$.

The squared diabatic coupling of all three methods is nearly identical, as shown in Figure 3.21. We analyzed the non-diabatic coupling, shown in Figure 3.22. The couplings computed with Boys, DQ and DΦ have a similar shape to finite difference. The magnitude of the peak is similar for all three methods and they agree at bond lengths greater than 2.9 a_0. The Boys and DQ nonadiabatic couplings match closely. No method agrees with finite difference at bond lengths less than 2.4 a_0.

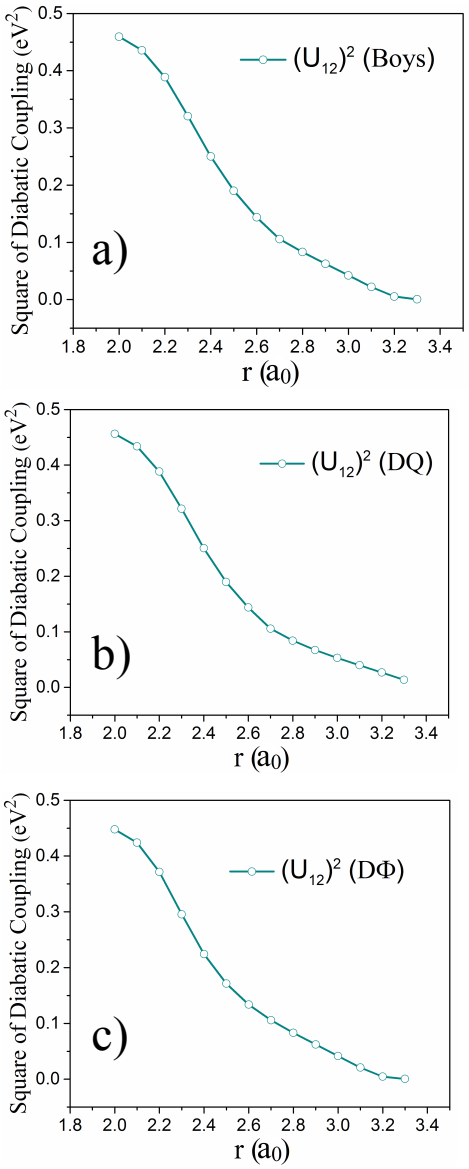

Figure 3.21. Square of the diabatic coupling of the two lowest 1^1 A″ and 2^1 A″ states of O_3 at 100°. The diabatic states were computed with (a) Boys method, b) DQ with an origin on each O and $\alpha = 10.0\ a_0^{-2}$, and c) DΦ with electrostatic potential origins on each O and $\beta = 1.0\ a_0$.

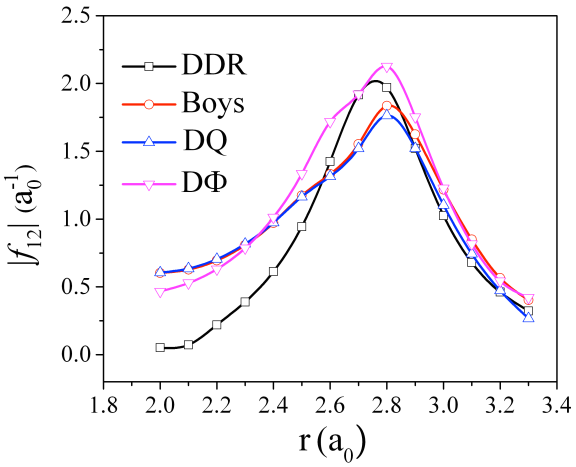

Figure 3.22. Absolute value of the nonadiabatic coupling of the two lowest 1^1 A″ and 2^1 A″ states of O_3 held at 100° bond angle. The coupling was computed with finite difference (DDR), Boys method, DQ with an origin on each O and $\alpha = 10.0\ a_0^{-2}$, and DΦ with electrostatic potential origins on each O and $\beta = 1.0\ a_0$.

3.6 Conclusions

We have investigated the dependence of the DQ method on the α parameter for producing adequate diabatic potential curves of HCl and LiH, where α is the weight given to the quadrupole, relative to the dipole, in determining diabatic states. For the ionic-covalent curve crossing of HCl, all nonzero values of α tested performed well, and all performed better than using only the dipole (Boys localized diabatization method). We also studied the first four $^1\Sigma^+$ states of LiH with the DQ method, and we found that it yields smooth diabats with a large value of α. Based on this work and our previous work on DQ, we recommend 10.0 a_0^{-2} as a starting value for α (it has worked for all systems tested as long as one has no unsmoothness caused as discussed above by the first excluded state).

We conclude that the DQ method is a useful method for diabatization due to its simplicity, applicability to general types of reactions, and generality with respect to the electronic structure method. Our findings are very encouraging in that a single value of α leads to successful results in a variety of systems. In this work we've also presented an

extension of the DQ method by including the electrostatic potential, yielding the DQΦ method. The $(H_2)_2$ diabatic curves show an improvement upon adding wither the quadrupole or the electrostatic potential. The LiFH results continue the trend of the diatomic hydrides, but also show a small improvement in smoothness with the addition of the electrostatic potential. Finally, the O_3 results show little change with the addition of the quadrupole or electrostatic potential near the conical intersection. However, at a 100° bond angle, which is farther from the conical intersection, the DΦ method yields the smoothest diabats. The addition of the electrostatic potential does not make the results worse in any of the systems we studied, and sometimes it makes them smoother. The added flexibility is expected to be useful for diabatization of polyatomics in many degrees of freedom. The DΦ and DQΦ methods show promise as new ways of obtaining good diabatic potentials.

4 Direct Diabatization Based on Nonadiabatic Couplings: The N/D Method

Adapted with permission from Zoltan Varga*, Kelsey A. Parker*, and Donald G. Truhlar, Phys. Chem. Chem. Phys. **20**, 26643 (2018);*Z.V. and K.A.P. contributed equally

In this chapter, I introduce a new diabatization method we developed based on components of the nonadiabatic couplings (NACs) and the adiabatic energy gradients; we call this method the N/D method. Section 4.1 explains the theory behind the method. Section 4.2 gives computational details for a number of test cases. Section 4.3 shows applications to the test cases. Section 4.4 summarizes the findings.

4.1 Theory

4.1.1 The N/D Transformation

In the adiabatic representation, the NACs arise from the nuclear momentum and nuclear kinetic energy operators acting on the electronic wave functions.[2, 16] The nonrelativistic, spin-free Schrödinger equation can be written as:[2]

$$\left\{-\frac{1}{2\mu}\nabla_{\mathbf{R}}^2 + \widehat{H}_{el}(\boldsymbol{R},\boldsymbol{r})\right\}\Psi(\boldsymbol{R},\boldsymbol{r}) = E\Psi(\boldsymbol{R},\boldsymbol{r}) \tag{1}$$

where E is the total energy, the electronic coordinates are denoted by **r**, the nuclear coordinates by **R**, and the nuclear mass by μ. (We use isoinertial coordinates so masses are the same for all nuclei.) The electronic Hamiltonian, which includes electronic kinetic energy, electron-electron, electron-nuclear, and nuclear-nuclear interactions, is denoted by H_{el}, the Laplacian (∇_R^2) extends over all nuclear coordinates, and $\Psi(R,r)$ is the wave function. The wave function can be expanded as:[2]

$$\Psi(\boldsymbol{R},\boldsymbol{r}) = \sum_{j=1}^{n}\psi_j(\boldsymbol{R})\phi_j(\boldsymbol{r};\boldsymbol{R}) \tag{2}$$

where j labels electronic states, $\phi_j(\boldsymbol{r};\boldsymbol{R})$ are normalized eigenfunctions of the electronic Hamiltonian, and $\psi_j(R)$ are nuclear wave functions. Substituting eqn (2) into eqn (1) yields,[2]

$$\left\{-\frac{1}{2\mu}\nabla_{\mathbf{R}}^2 + V_j(\mathbf{R})\right\}\psi_j(\mathbf{R}) + \sum_k\left\{-\frac{1}{\mu}\vec{f}_{jk}(\mathbf{R})\cdot\nabla_{\mathbf{R}} - \frac{1}{2\mu}t_{jk}(\mathbf{R})\right\}\psi_k(\mathbf{R}) = E\psi_j(\mathbf{R}) \tag{3}$$

where

$$V_j(\mathbf{R}) = \int \phi_j^*(\boldsymbol{r};\boldsymbol{R})\widehat{H}_{el}\,\phi_j(\boldsymbol{r};\boldsymbol{R})d\boldsymbol{r} \tag{4}$$

$$\vec{f}_{jk}(\mathbf{R}) = \int \phi_j^*(\boldsymbol{r};\boldsymbol{R})\nabla_R\,\phi_k(\boldsymbol{r};\boldsymbol{R})d\boldsymbol{r} \tag{5}$$

$$t_{jk}(\mathbf{R}) = \int \phi_j^*(\boldsymbol{r};\boldsymbol{R})\nabla_R^2\,\phi_k(\boldsymbol{r};\boldsymbol{R})d\boldsymbol{r} \tag{6}$$

The function $V_j(\boldsymbol{R})$, is the adiabatic potential energy function for nuclear motion in state *j*, and these potentials may be assembled as the elements of a diagonal matrix **V**(**R**). We always arrange them such that $V_1(\boldsymbol{R}) \le V_2(\boldsymbol{R}) \le V_3(\boldsymbol{R})$ .... For *N* atoms, the vector $\vec{f}_{jk}(\mathbf{R})$ is the 3*N*-dimensional nuclear momentum coupling vector between states *j* and *k*, and $t_{jk}(\mathbf{R})$ is the kinetic energy coupling, which is usually considered less important in semiclassical approximations,[82] and which can also be hard to treat consistently in approximate approaches.[83] (We omit it here not because it is necessarily ignorable but rather as part of the freedom we have to choose a non-unique diabatic transformation.) In the rest of the paper, $\vec{f}_{jk}(\mathbf{R})$ will be called a NAC. Note that a NAC is a 3N-dimensional vector in coordinate space, but it is also an off-diagonal matrix element of an $n\times n$ matrix in electronic state space; the anti-Hermitian property of the gradient in eqn (5) means that[2]

$$\vec{f}_{jk}(\mathbf{R}) = -\vec{f}_{kj}(\mathbf{R}) \tag{7}$$

and

$$\vec{f}_{jj}(\mathbf{R}) = 0 \tag{8}$$

In a diabatic representation, one neglects the NACs.[2, 16] Although it is well known that one cannot completely eliminate the coupling due to NACs,[16] the idea of making a transformation with a form similar to diagonalizing the NAC matrix is what motivates

our strategy. In particular, we obtain a diabatic representation by a sequence of diagonalizations applied to matrices of the form:

$$\mathbf{M}^{(jk)}(\mathbf{R}) = \begin{bmatrix} M_j^{(jk)}(\mathbf{R}) & f_{jk}(\mathbf{R}) \\ f_{jk}(\mathbf{R}) & M_k^{(jk)}(\mathbf{R}) \end{bmatrix}$$

where $f_{jk}(\mathbf{R})$ is the magnitude of $\vec{f}_{jk}(\mathbf{R})$. Because $\mathbf{M}^{(jk)}(\mathbf{R})$ is a 2×2 matrix, it can be diagonalized by a single Jacobi rotation, which yields the diagonal matrix

$$\widetilde{\mathbf{M}}^{(jk)}(\mathbf{R}) = \left[\mathbf{P}^{(jk)}(\mathbf{R})\right]^{-1}\mathbf{M}^{(jk)}(\mathbf{R})\mathbf{P}^{(jk)}(\mathbf{R}) \tag{9}$$

where

$$\mathbf{P}^{(jk)}(\mathbf{R}) = \begin{pmatrix} \cos\theta_{jk}(\boldsymbol{R}) & -\sin\theta_{jk}(\boldsymbol{R}) \\ \sin\theta_{jk}(\boldsymbol{R}) & \cos\theta_{jk}(\boldsymbol{R}) \end{pmatrix} \tag{10}$$

and where

$$\tan(2\theta_{jk}) = \frac{N_{jk}(\mathbf{R})}{D_{jk}(\mathbf{R})} \tag{11}$$

where the numerator is

$$N_{jk}(\mathbf{R}) = \tilde{f}_{jk}(\mathbf{R}) \tag{12}$$

with $\tilde{f}_{jk}(\mathbf{R})$ being either a NAC or a modified NAC, and the denominator is

$$D_{jk}(\mathbf{R}) = M_k^{(jk)}(\mathbf{R}) - M_j^{(jk)}(\mathbf{R}) \tag{13}$$

where $M_k^{(jk)}$is exaplined in Section 4.1.3. The use of a modified NAC in the numerator allows us to remove undesired couplings in the Born–Oppenheimer approximation and will be explained in Section 4.1.2.

This corresponds to a 2×2 rotation of two adiabatic basis functions. When there are more than 2 states, we apply this transformation in sequence to "eliminate" NACs one-by-one; for example for 3-state case, first $f_{12}(\mathbf{R})$, then $f_{13}(\mathbf{R})$, and finally $f_{23}(\mathbf{R})$. Note that a Jacobi transformation makes previously rotated off-diagonal elements nonzero

again, therefore the procedure has to be repeated until all of the off-diagonal elements become zero to within a pre-established tolerance. We stop the iteration if the root mean square of the off-diagonal elements is less than 5×10^{-7} a. u. This sequence of transformations of the adiabatic basis functions is then used to transform the potential energy matrix into the diabatic representation. In particular, we get the following diabatic potential energy matrix:

$$[\mathbf{P}(\mathbf{R})]^{-1}\mathbf{V}(\mathbf{R})\mathbf{P}(\mathbf{R}) = \mathbf{U}(\mathbf{R}) \tag{14}$$

where $\mathbf{P}(\mathbf{R}) = \prod \mathbf{P}^{(jk)}(\mathbf{R})$, i.e., the product of the individual rotation matrices of state pairs.

After the transformation, rows and columns of $\mathbf{U}(\mathbf{R})$ correspond to the diabatic states, but they might not be in the right order. We found, however, that it is easy to re-order them by inspection.

The adiabatic potential curves are sometimes called adiabats, and the diabatic potential curves are sometimes called diabats.

The resulting method is called the N/D method to recognize the key role of eqn (11). All that remains is to identify suitable formulas for the numerator $N_{jk}(\mathbf{R})$ and the denominator $D_{jk}(\mathbf{R})$, that is, for $\tilde{f}_{jk}(\mathbf{R})$ and for $M_i^{(jk)}(\mathbf{R})$, with $i = j$ or k.

4.1.2 The N/D Numerator

First we consider the numerator. It is well documented that NACs are unphysical in various respects; this is discussed in various ways, including the lack of electron momentum in the Born-Oppenheimer basis and the dependence of conventional Born-Oppenheimer calculations on the coordinate system.[84-100] This is not a serious problem in regions where adiabatic states are strongly coupled because the NACs are singular at conical intersections and the singular terms that dominate in strongly coupled regions are

free of these defects;[81] however, the incorrect behavior of NACs when subsystems separate is very inconvenient for dynamics.[84-85, 87, 90, 96, 99-100] Our first modification of NACs is to remove these long-range couplings because they are "fictitious" forces in the sense defined by Delos.[90] As in other aspects of the present treatment, we do this by taking advantage of the fact that diabatic states are not uniquely defined.

The starting NACs for the treatment proposed here are those calculated analytically by the *Molpro* electronic structure package.[63] These NACs are calculated by displacing one coordinate at a time in the 3*N*-dimensional Cartesian coordinate system without transformation to a center-of-mass coordinate system. These NACs may be written,

$$\vec{f}_{jk}(\mathbf{R}) = \sum_{\rho=1}^{N}\sum_{\gamma=1}^{3} f_{jk,\rho\gamma}(\mathbf{R})\hat{\mathrm{e}}_{\rho\gamma} \tag{15}$$

where $\hat{\mathrm{e}}_{\rho\gamma}$ is a unit vector, ρ labels an atom in the *N*-atom system, γ = 1,2,3 corresponds to the *x,y,z* Cartesian coordinates, and

$$f_{jk,\rho\gamma}(\mathbf{R}) = \int \phi_j^*(\boldsymbol{R},\boldsymbol{r})\frac{\partial}{\partial \boldsymbol{X}_{\rho\gamma}}\phi_k(\boldsymbol{R},\boldsymbol{r})d\boldsymbol{r} \tag{16}$$

where $\boldsymbol{X}_{\boldsymbol{\rho\gamma}}$ is an atomic Cartesian coordinate. To eliminate unphysical coupling we replace $\vec{f}_{jk}(\mathbf{R})$ by

$$\vec{g}_{jk}(\mathbf{R}) = \sum_{\rho=1}^{N}\sum_{\gamma=1}^{3} w_\rho f_{jk,\rho\gamma}(\mathbf{R})\hat{\mathrm{e}}_{\rho\gamma} \tag{17}$$

where w_ρ is a weighting function that may be different for each atom ρ and may even be zero for some atoms, and we define

$$g_{jk}(\mathbf{R}) = \left|\vec{g}_{jk}(\mathbf{R})\right| \tag{18}$$

Our second modification is to place a threshold on the usage of the NACs. This serves two purposes: (i) it avoids unnecessary operations in regions where the NACs are very small and inconsequential and may be sensitive to the numerical methods used to compute them; (ii) it allows for stable treatment of asymptotic regions where the

couplings should have no effect. Applying the threshold yields the following expression for the numerator:

$$N_{jk}(\mathbf{R}) \equiv \tilde{f}_{jk}(\mathbf{R}) = \begin{cases} 0 & \text{if } g_{jk} \leq f_{\text{thr}} \\ g_{jk}(\mathbf{R}) - f_{\text{thr}} & \text{otherwise} \end{cases} \tag{19}$$

where $f_{\text{thr},jk}$ is a parameter. If $\tilde{f}_{jk}(\mathbf{R})$ is zero at some $\mathbf{R}$, then the diagonalization is skipped at that $\mathbf{R}$, i.e., $\mathbf{P}^{(jk)}(\mathbf{R})$ is set equal to the unit matrix, and no rotation of state *j* with state *k* occurs at that $\mathbf{R}$.

In some cases, one might want to use a different weight or a different threshold for different state pairs (replace w_ρ and/or f_{thr} by $w_{jk,\rho}$ and/or $f_{\text{thr},jk}$), but that was not necessary here.

4.1.3 The N/D Denominator

The denominator needs to work in concert with the NACs to provide diabatic curves that have the correct physics. The proposed function for the denominator is

$$D_{jk}(\mathbf{R}) = \varepsilon \sum_{\rho=1}^{N-1} \sum_{\rho'=\rho+1}^{N} W_{jk,\rho\rho'}\, h_{jk,\rho\rho'}(\mathbf{R}) \tag{20}$$

where ε is a scaling factor, $W_{jk,\rho\rho'}$ is a weight, and

$$h_{jk,\rho\rho'}(\mathbf{R}) = \frac{\partial}{\partial Q_{\rho\rho'}} \left[V_k(\mathbf{R}) - V_j(\mathbf{R}) \right] \tag{21}$$

where $Q_{\rho\rho'}$ are the $N(N\text{-}1)/2$ internuclear distances of atom pairs r and r' for the N-atom system. Ideally, the internuclear distances that are roughly perpendicular to the seam of diabatic crossing should be used. This can be controlled by the weighting function $W_{jk,\rho\rho'}$ for each state pair. Notice that for $N > 4$, the internuclear distances are a redundant set of internal coordinates, but in practice we will set the weighting function of many of the partial derivatives equal to zero using $W_{jk,\rho\rho'}$, and the number of terms retained in eqn (20) will be less than F.

To motivate eqn (20), let's consider passing through a locally avoided intersection of two states of the same symmetry. In the diabatic representation, the two states cross, and the gradients of those two states are smooth and do not cross. In the adiabatic representation, the potential energy surfaces do not cross, but the two energy gradients must switch if those two adiabatic states have a crossing or avoided crossing due to a change in configuration. Therefore, the denominator will change sign, and therefore the tangent of eqn (11) will also change sign. On one side of the sign change, $2\theta_{jk}$ will be in the range 0 to π/2, and on the other side of the sign change it will be in the range π/2 to π. Consequently, on one side of the sign change, cos θ_{jk} will be greater than sin θ_{jk}, but on the other side it will be smaller. Thus the transformation of eqn (10) will switch the diabats from one adiabat to another, which is our goal. In a simple case a single $Q_{\rho\rho'}$ might be enough for diabatization.

According to eqn (20), a scaling factor (ε) is required to adjust the relative scale of the numerator and denominator because they would otherwise have different units. If the scaling factor were too small, then the nominator in eqn (11) will dominate, thus strong mixing would occur over a wide range of geometries. In an extreme case, the diabatic states would be stuck together instead of crossing one another. Even in the regions where the diabatic energies should be approximately equal to the adiabatic energies, the diabatic energies would still correspond to significant mixtures of adiabatic energies. On the other hand, if the scaling factor were too large, then the denominator in eqn (11) would dominate, and the diabatic coupling would be significant only for a very narrow range of geometries. In an extreme case, the diabatic energies would be approximately equal to the adiabatic energies, and due to the sign change the two diabatic curves would suddenly switch at the diabatic state crossing. A reasonable choice for ε will result in a reasonable peak in the NAC. (Theoretically a NAC will approach infinity at a conical intersection; however, the usual case encountered for a polyatomic system along a path is a locally

avoided crossing because it is unlikely that a path goes precisely through a conical intersection by chance).

If the diabatic crossing seam is highly curved, the employed coordinates $Q_{\rho\rho'}$ might need to be functions of **R** controlled by geometry-dependent $W_{jk,\rho\rho'}$, but $W_{jk,\rho\rho'}$ should be a smooth function. In the present treatment though we take $W_{jk,\rho\rho'}$ to be independent of geometry.

In the following sections, we will show that the NACs and gradients of the adiabatic states, when used together, can provide relevant chemical insight into the system by uncovering the physical diabatic states that underlie the adiabatic ones.

4.2 Test Cases

All of the calculations in this work were carried out using the *Molpro* program package[63, 101] with state-averaged CASSCF,[10-14] i.e., SA(*n*)-CASSCF, where *n* is the number of states averaged. In all cases, equal weights were used for the state average. *Molpro* calculates the energy gradients for each state and the NAC values for the state couplings analytically via coupled-perturbed multi-configurational self-consistent field (MCSCF) calculations. active spaces will be labeled (*e,o*), where *e* is the number of active electrons and *o* is the number of active orbitals.

LiF

For the calculation of LiF dissociation, C_{2v} symmetry was used and the first two singlet A_1 states were averaged with equal weights ($n = 2$). The 1s orbital of Li and the 1s and 2s orbitals of F were kept doubly occupied. The active space was (6,7), and the 6-311+G* basis set[75, 102] was used. The potential energy curve was scanned from 0.8 Å to 10.0 Å.

$H + H_2$

In the minimum energy path calculation of H_3, three states were averaged, but only the first two singlet A' states were used in the diabatization process ($n = 3$ for SA(n)-CASSCF, but $n = 2$ for eqn (2)). The symmetry of the system was set to C_s. The active space was (3,15) with twelve a' and three a'' orbitals; the def2-QZVP basis set[103] was used. The geometries correspond to an approximate minimum-energy path and are specified in the supporting information for the paper.

$(H_2)_2$

The calculation of the H_2 dimer system corresponds to the calculation used in the previous fourfold way and DQΦ work.[69, 104] Thus $n = 3$ in SA(n)-CASSCF calculations, the active space is (4,4); and the TZP basis set[105] was used. The symmetry was turned off.

Li + HF

The reaction path of Li + FH → LiF + H was previously studied with the fourfold way and DQΦ method.[69, 104] The symmetry of this three-body system is C_s. We consider $n = 2$ with both states being singlet A'. The active space is (7,8), including the 2s and 2p orbitals of Li, the 2p orbitals of F, and the 1s orbital of H; the 6-311+G* basis set[75, 102] was used.

PhOH

The photodissociation of phenol into PhO and H was also calculated. To get the diabatic representation for photodissociation, we considered $n = 3$. We used the same active space as Ref.[80], which is (12,11); the def2-SVPD basis set[106] was used. The equilibrium geometry of phenol was taken from Ref.[80]. The torsion angle between the C(6)-C(1)-C(2) plane and the C(1)-O-H plane was $\theta = 45°$; therefore the calculated structures belong to C_1 symmetry. Then the OH bond distance was varied between 1.0 and 3.0 Å, and except for this bond distance and θ, the other internal coordinates are fixed at their equilibrium values.

O_3

For O_3, C_s symmetry was applied, and the first three $^3A'$ triplet states were calculated (n = 3). The active space was (12,9) including the nine 2p orbitals. The bond angle of the three oxygen atoms was fixed at 175 degrees. One of the bond lengths was fixed at the equilibrium distance of O_2 molecule, R_e = 1.208 Å, and the other bond length was scanned from 3 to 1 Å. In these calculations, the maug-cc-pVTZ basis set[107-109] was used.

In all the calculations described so far, the adiabatic states are obtained with SA(n)-CASSCF and diabatization was carried out by the N/D method. For O_3, for comparison, we also ran calculations with the DQΦ method.[104] In the DQΦ calculations, we started with the same SA(3)-CASSCF(12,9) calculations as used for N/D and then added external correlation by extended multi-state second order perturbation theory[15, 110-112] (XMS(3)-CASPT2) to obtain the adiabatic energies and dipole, quadruple, and electrostatic potential matrix elements required for DQΦ diabatization. The def2-TZVPD basis set[106] was used in the DQΦ calculations.

4.3 Results

To apply the method to a given case, we must specify the options that can be different for different applications. There are four of these: (i) the unitless weights w_ρ used in the numberator, (ii) the threshold f_{thr} used in the numerator, (iii) the choices of internuclear distances $Q_{\rho\rho'}$ for each jk state pair for the denominator as determined by the nonzero weights $W_{jk,\rho\rho'}$ used in the denonimator, and (iv) the energetic scaling parameter ε used in the denominator. The values of these parameters used for the current article are given in Table 4.1.

Table 4.1. Parameters of the N/D calculations[a]

System	w_ρ	f_{thr} (a_0^{-1})	ε (E_h^{-1})	$W_{jk,\rho\rho'}$
LiF	1	0	160	$W_{12,\text{LiF}} = 1$
$H + H_2$	1	0	sets 1,2: 20 set 3: 10	set 1: $W_{12,12} = 1$ set 2: $W_{12,13} = 1$ set 3: $W_{12,12} = 1$, $W_{12,13} = -1$
$(H_2)_2$	1	0	200	set 1: $W_{23,12} = W_{23,13} = W_{23,23} = 1$ $W_{23,14} = W_{23,24} = W_{23,34} = -1$ set 2: $W_{jk,12} = W_{jk,13} = 1$ $W_{jk,24} = W_{jk,34} = -1$
LiHF	1	sets 1,3: 0.25 set 2: 0.3	sets 1,3: 70 set 2: 300	set 1: $W_{12,\text{FH}} = 1$ set 2: $W_{12,\text{LiF}} = 1$ set 3: $W_{12,\text{LiF}} = W_{12,\text{LiH}} = 1$
phenol	$w_{\text{OH}} = 1$ $w_{\text{other }\rho} = 0$	0.2	80	$W_{jk,\text{OH}} = 1$
O_3	1	0.2	40	$W_{jk,12} = 1$ $W_{jk,13} = -1$

[a] 1 a_0 = 1 bohr = 0.5292 Å; 1 E_h = 1 hartree = 27.212 eV. The value of w_ρ is the same for all ρ except where indicated otherwise. Only nonzero $W_{jk,\rho\rho'}$ are shown.

4.3.1 LiF

Our first example is LiF, which is a well studied case of ionic–covalent curve crossing. The NACs as well as the energy gradients are 3*N*-dimensional vectors in Cartesian coordinates. In Fig. 4.1a shows the magnitude of the NAC between the ground and the first excited states; Fig. 4.1b shows the difference between adiabatic energy gradients of the ground and the first excited states with respect to the internuclear distance of the two atoms as a function of the internuclear distance. Figure 4.1b shows that the two gradients cross each other around 5.6 Å, where Fig. 4.1(a) shows that N_{12} has a peak.

The adiabatic (V_1 and V_2) and diabatic (U_{11} and U_{22}) potential energy curves and the diabatic coupling (U_{12}) are shown in Fig. 4.2. The two diabatic curves cross smoothly around 5.6 Å. Thus the method is successful in this simple case.

In the repulsive wall region, the energy of the adiabatic ground state increases more rapidly than the energy of the adiabatic first excited state, leading to the denominator of eqn (11) changing its sign around 1.2 Å. At the same time the nominator is increasing as the distance between the two atoms becomes shorter. These two features lead to a sudden state crossing at 1.2 Å but the energy of two diabatic states are not significantly different than the adiabatic energies in this region, and the diabatic energies were manually switched back for the plot.

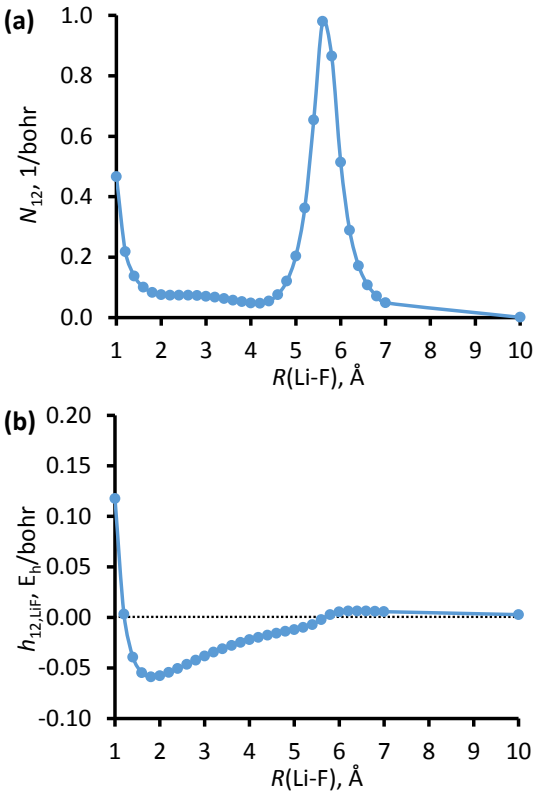

Figure 4.1. Input data for the N/D diabatization of LiF: (a) magnitude of the NAC, and (b) difference between adiabatic energy gradients of the ground and the first excited states.

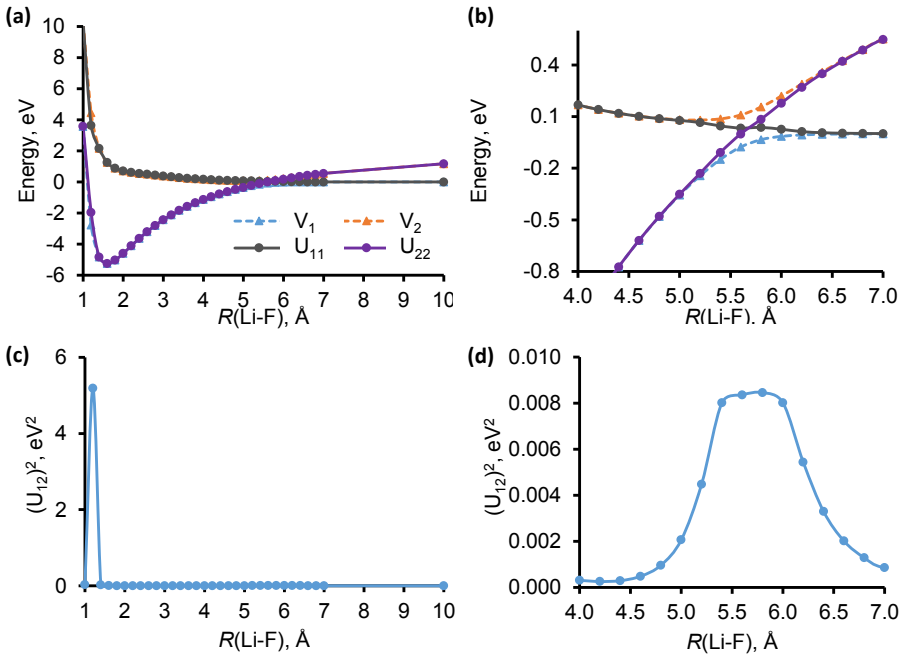

Figure 4.2. (a) Adiabatic and diabatic potential energy curves and (c) square of the diabatic coupling for LiF calculated with N/D. Plots (b) and (d) are enlarged curves at the avoided crossing region.

4.3.2 $H + H_2$ exchange reaction

The minimum energy path of the $H + H_2$ exchange is collinear. The central hydrogen is labeled H_1 and the two terminal hydrogens are labeled H_2 and H_3. At the saddle point the two nearest-neighbor H–H bond lengths, R_{12} and R_{13} are equal to $R_{HH}^{\ddagger}$ = 1.757 a_0 , and this point is defined as the origin of the reaction coordinate, which is defined as

$$s = \text{sign}\left(R_{12} - R_{HH}^{\ddagger}\right)\left(\sqrt{\left(R_{12} - R_{HH}^{\ddagger}\right)^2 + \left(R_{13} - R_{HH}^{\ddagger}\right)^2}\right), \tag{22}$$

For this example, the ground state and first excited state were taken into account. The two states are well separated in energy; the energy difference is 6.7 eV at the saddle point according to the CASSCF calculations. Thus, their crossing is widely avoided. Every component of the NAC was used to calculate the nominator N_{12}, which is given in Fig. 3a.

Three different diabatizations will be presented to illustrate the flexibility of the N/D method; these sets differ only the parameters used to calculate the denominator D_{12}. The three partial derivatives of the energy gap along the reaction path are shown in Fig. 3b. Based on the shape of these three curves, it is easy to conclude that the data set of gradient difference based on r_{23} will not lead to useful diabatization as it does not cross zero (gray curve in Fig. 4.3(b)). This gradient difference was not used in eqn (20). The investigated solutions include the following sets of gradient differences. Set 1 only includes the gradient difference for r_{12} (i.e, $W_{12,12} = 1$, and the other two are zero). Set 2 only includes the gradient difference for r_{13} (i.e, $W_{12,13} = 1$, and the other two are zero). Set 3 includes the gradient difference from both r_{12} and r_{13}; their weights in eqn (20) are $W_{12,12}$, = 1 and $W_{12,13}$ = –1.

Both sets 1 and 2 provide smooth diabats, but the state crossing is slightly shifted away from zero (the saddle point). Set 1 shifts the crossing slightly right, and set 2 shifts the crossing slightly left. These shifts are in accord with the locations where the partial derivative differences cross zero, as shown in Fig. 4.3(b). When the combination of the two gradient differences is used, as described in set 3, the crossing occurs at the saddle point, as expected. The solutions of diabatizations based on these three sets are shown in Fig. 4.4.

This illustrates an important point. When a system shows symmetry, one should take account of that symmetry when assigning the parameters. When this was done, the method is successful for the H + H_2 reaction. For LiF we considered a narrowly avoided crossing, and here we consider a widely avoided one; the method is successful in both cases.

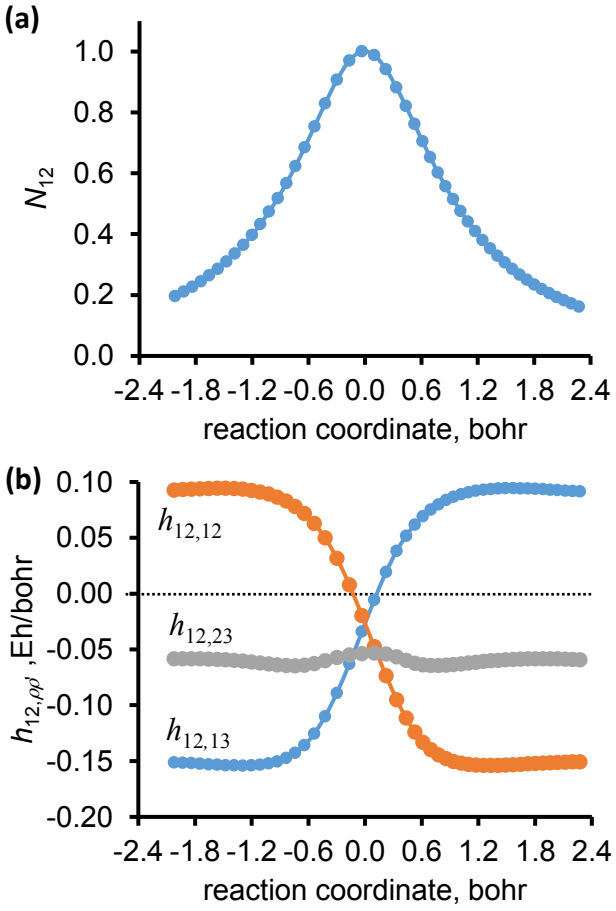

Figure 4.3. Input data for the N/D diabatization for the H_2 + H exchange: (a) magnitude of the NAC between the ground and the first excited states, and (b) the differences between partial derivatives (with respect to the three internuclear distances) of adiabatic energy differences.

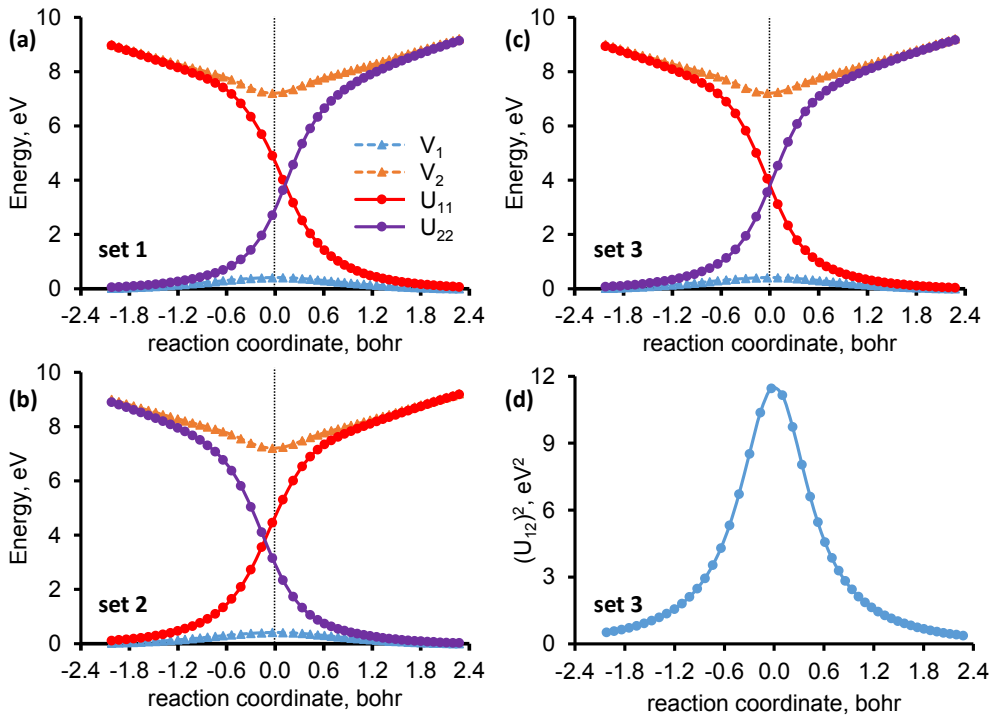

Figure 4.4. Adiabatic and diabatic potential energy curves and square of diabatic coupling for the H + H_2 reaction.

4.3.3 H_2 dimer

The H_2 dimer was previously calculated by both the fourfold way and DQΦ (in particular by the Boys localized, DQ, and DΦ special cases of DQΦ).[69, 104] The four atoms are collinear, and we consider a system consisting of two hydrogen molecules with centers of mass separated by 10 a_0 and with each molecules starting with a bond distance of R_0 = 1.5 a_0. The bond lengths of the two molecules are simultaneously changed by DR; one of the H_2 bond distances is decreased (R_0 – DR) and the other H_2 bond distance is increased (R_0 + DR). The range of DR is -0.2 to 0.2 a_0. This reaction coordinate results in one bond switching from stretched to compressed while the other molecule simultaneously goes from compressed to stretch. When DR is zero, the two bond lengths are equal (at the middle of the reaction coordinate). Along this reaction path, the first and second excited states (i.e., states 2 and 3, both $^1S^+$), show a locally avoided crossing in the adiabatic

representation. These two crossing states are energetically well separated from the ground state.

To carry out the N/D diabatization, we considered two possible ways to proceed. The ground state is well separated from the other two states and the ground state is only slightly coupled with either of the two excited states; see Fig. 4.5(a). Therefore, in the first set of calculations, a simple two-by-two diabatization is carried out for state pair *ij* = 23. The partial derivatives of the 2-3 energy gap are shown in Fig. 4.5(d) for the six possible internuclear distances. We label the atoms left to right: 1,2 for the first H_2 and 3,4 for the second H_2. As can be seen in the plot, four of the curves can lead to useful diabatization, but, similarly to the situation in subsection 4.2, the diabats based on a single atom pair set would suffer from some asymmetry. Therefore, we again take a linear combination to get symmetric diabatic energy curves. Among the possible combinations, we only show the one for which the weights $W_{23,\rho\rho'}$ are 1.0, 1.0, -1.0, 1.0, -1.0, and -1.0 with respect to internuclear ditances, R_{12}, R_{13}, R_{14}, R_{23}, R_{24}, and R_{34}, respectively. The two diabatic curves cross smoothly where the two H_2 molecules have equal bond lengths ($R_{12} = R_{34}$) as shown in Fig. 4.6.

A second set of calculations is shown for a three-by-three diabatization. The differences of the partial energy derivatives with respect to the six possible internuclear distances for state pairs 12 and 13 are shown in Figs. 4.5(b) and 4.5(c). For all three *jk* state pairs, the weights $W_{jk,\rho\rho'}$ were selected to be 1.0, 1.0, 0.0, 0.0, -1.0, and -1.0 for the partial derivatives with respect to the six internuclear distances in the same order as above. Figure 4.7 shows the result of this diabatization. In this diabatization the couplings of state pairs 12 and 13 are stronger than that of state pair 23, but state 1 is well separated from the other two states in energy, thus those couplings do not cause the diabatic energy curves to differ noticeably from the adiabatic ones in Fig. 4.7(a). As expected, diabatic states 2 and 3 cross each other where the two H_2 molecules have equal bond lengths.

Thus both strategies yield useful diabats, but the simpler two-state treatment r probably preferable.

If one used larger $W_{12,\rho\rho'}$ and $W_{13,\rho\rho'}$, the couplings of state pairs 12 and 13 would be further decreased, but for all examples shown in the present article, $W_{jk,\rho\rho'}$ is independent of j and k.

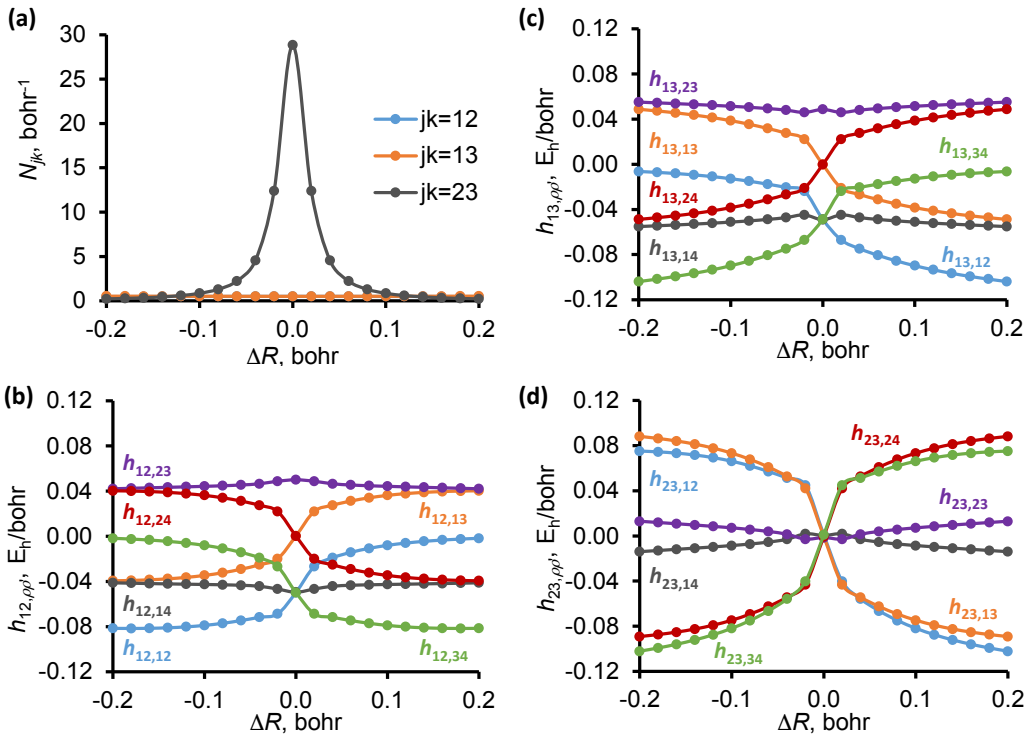

Figure 4.5. Input data for the N/D diabatization of H_2 dimer: (a) magnitudes of the NACs between state pairs 12, 13, and 23, and (b), (c), and (d) show differences between adiabatic energy gradients of state pairs 12, 13, and 23, respectively, with respect to the six internuclear distances.

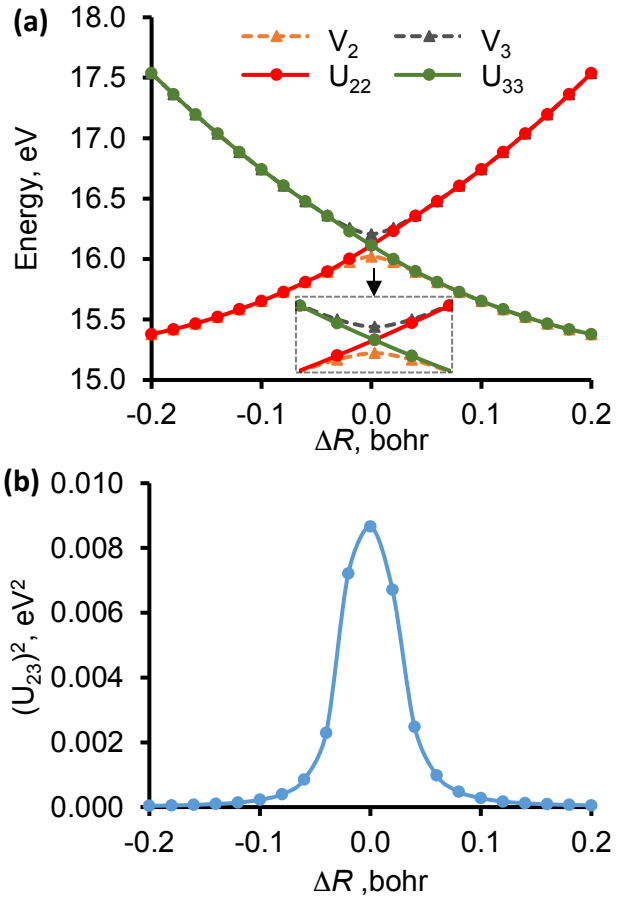

Figure 4.6. Adiabatic and diabatic potential energy curves and the square of the diabatic coupling for H_2 dimer based on a two-by-two diabatization for state pair 23

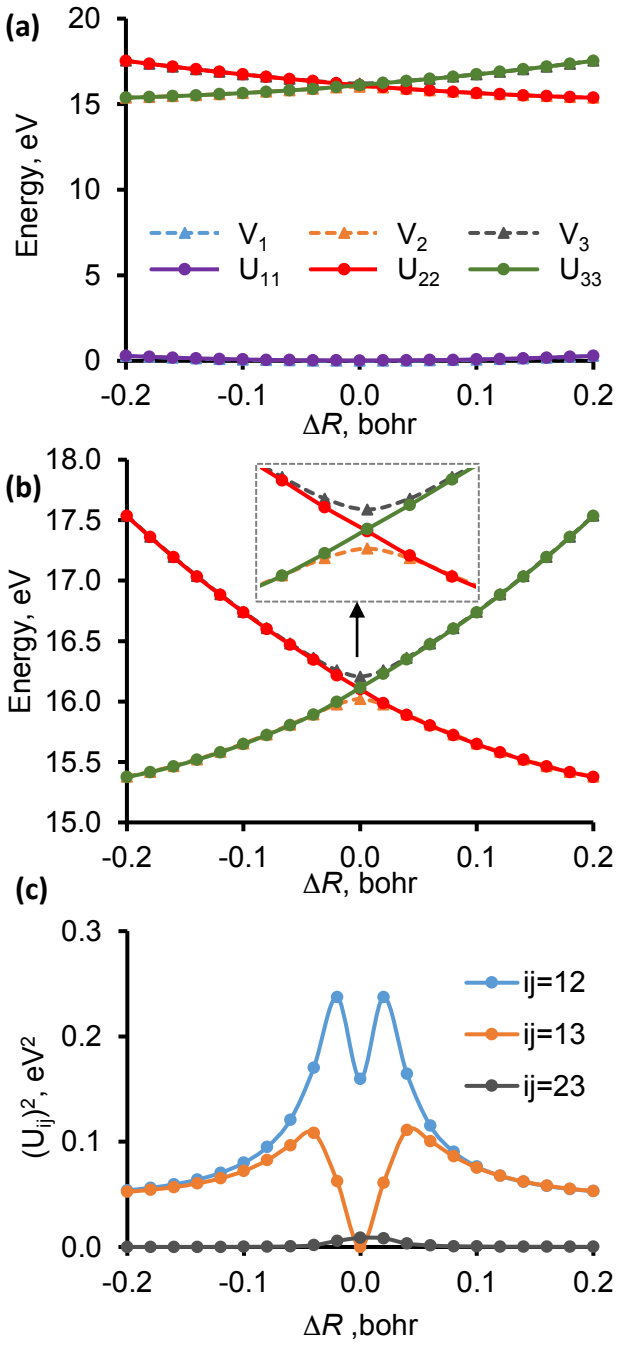

Figure 4.7. Adiabatic and diabatic potential energy curves (a) as well as their coupling (c) of H_2 dimer based on a three-by-three diabatization ("set 2" diabatization). Plot (b) enlarges the coupling region of state pair 23.

4.3.4 LiHF

The LiFH system involves the reaction: Li(^{2}S, ^{2}P) + FH $\rightarrow$ LiF + H. The ground and first excited states in the reactant region, 1 $^2A'$ and 2 $^2A'$, correspond to the Li atom in the ^{2}S and ^{2}P states, respectively. In the products region, the ground state has a singly occupied H(1*s*) orbital and the first excited state corresponds to electron donation from an in-plane lone pair on the F to the H atom, which becomes very high in energy along the product coordinate. The reaction coordinate has been previously defined in a fourfold way and DQΦ study.[69, 104] The zero of the coordinate is located at the saddle point of the lower adiabatic potential curve. The positive side of the coordinate corresponds to motion towards LiF + H, the products; the negative side corresponds to motion towards LiH + F, the reactants. Distances between successive points along the reaction coordinate are defined by

$$\Delta s = \sqrt{\sum_{\rho=\mathrm{Li,F,H}}\left(\Delta X_\rho^2 + \Delta Y_\rho^2 + \Delta Z_\rho^2\right)} \tag{23}$$

where ΔX_ρ, ΔY_ρ, and ΔZ_ρ corespond to differences in mass-weighted Cartesian coordinates of the atoms (this definition only affects the scale of the abscissa in plots; it has no effect on diabatization).

Previous calculations with the fourfold way and DQΦ diabatization method were successful.[69, 104] However, the fourfold way required a reference orbital, and the introduction has already pointed out that it would be desirable to avoid reference orbitals, because defining them may require an in-depth knowledge of the system. Three partial derivative differences for this two-state problem are shown in Fig. 4.8(b). These partial derivatives correspond to the LiF, LiH, and FH internuclear distances. Among these three curves, the FH data set, labeled set 1, ($W_{12,\mathrm{FH}} = 1$, $W_{12,\mathrm{LiF}} = 0$, and $W_{12,\mathrm{FH}} = 0$) and the LiF data set, labeled set 2, ($W_{12,\mathrm{LiF}} = 1$ and the other two weights are zero) can lead to useful diabatization, since these curves change sign near the saddle point. The two predicted diabatic energy sets are slightly different; when using set 1, the crossing is

shifted towards the reactant side as compared to set 2, see Fig. 4.9(a) and 4.9(b). We also investigated a linear combination of the three partial derivatives (set 3), where the $W_{12,\rho\rho'}$ weights in eqn (20) are 1.0, 1.0, and -1.0 for the LiF, LiH, and FH partial derivatives, respectively. For all three sets, g_{12} (which appears in the nominator) is shown in Fig. 4.8(a). Figures 4.9(a), 4.9(b), and 4.9(c) show very good agreement between the three sets of diabatization. As diabats are not unique, all three solutions to the diabatization problem can be acceptable, and one could choose which set of diabats to use based on other considerations, for example, on the behavior in other regions of geometry.

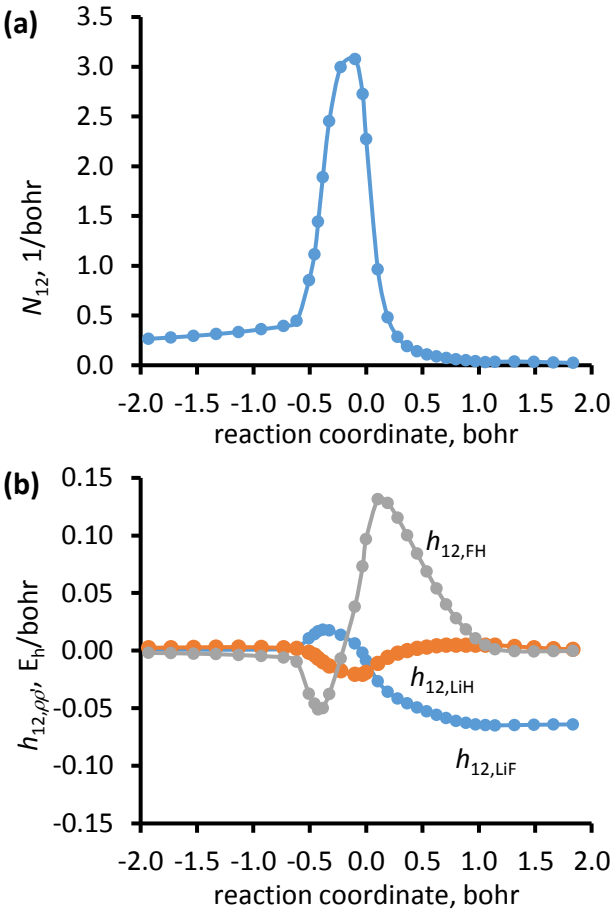

Figure 4.8. Input data for the N/D diabatization of reaction Li(^{2}S, ^{2}P) + FH → LiF + H: (a) magnitude of the NACs between the ground and the first excited states and (b) differences between adiabatic energy gradients of the ground and the first excited states with respect to the three internuclear distances.

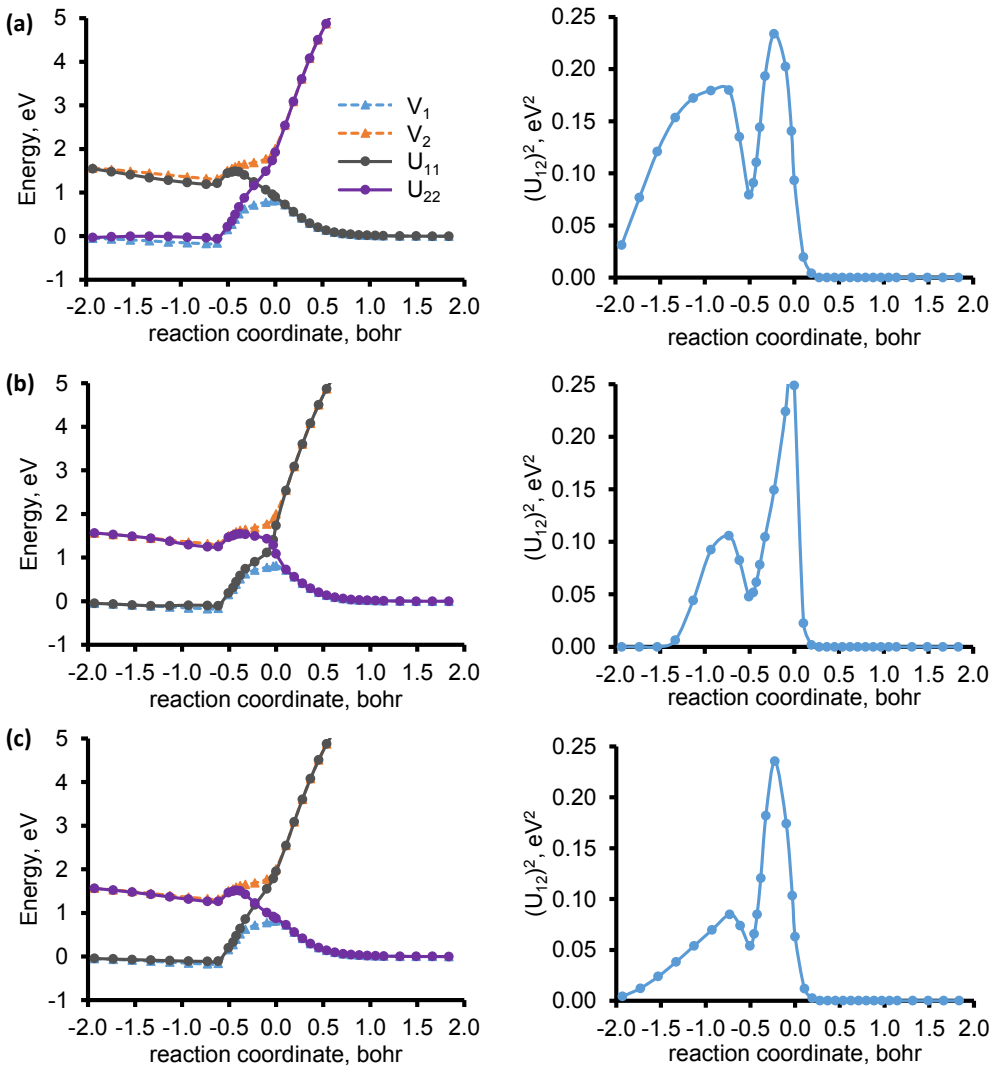

Figure 4.9. Adiabatic and diabatic potential energy curves and coupling of Li(^{2}S, ^{2}P) + FH → LiF + H. (a), (b), and (c) correspond to sets 1, 2, and 3, respectively. (b) enlarges the coupling region of state pair 23.

4.3.5 Phenol

The photodissociation of phenol has previously been modeled as a three-state process;[113] as the O-H bond dissociates, the system passes two conical intersections.[80] The electronic configuration of the ground adiabatic state at dissociation corresponds to the configuration of the third adiabatic state at the equilibrium bond distance of OH. The minimum energy pathway of the dissociation occurs in a planar structure, and the presence of conical intersections is clearly seen in the shapes of the adiabatic potential

energy curves. To show our results for a nonsymmetrical path, we distorted the geometry by turning the dissociating hydrogen out of the plane of the phenoxyl radical by the torsion angle θ, where $\theta = 45°$. Along the O–H bond dissociation path at this fixed torsion angle, the presence of one of the state crossings is no longer in the shapes of the adiabatic energy curves, so this provides a good test.

Phenol is a larger system than our previous examples, and it is used to illustrate that NAC components for atoms far from the reaction center are not essential for diabatization. The NAC components are typically nonzero even when we expect the diabats to be very similar the adiabats, and as we include more NAC components these nonzero components add up. However, most of those components could be considered to be "background noise", and, if included, that noise could obscure the useful NAC components that carry the physics of the state crossing. As an example, in Fig. 4.10 we compare the whole magnitude of NAC components of all atoms (plot 10a) with only the magnitude of NAC components of the oxygen atom and the dissociating hydrogen atom (plot 10b). In both plots, the NAC elements predict a sharp state crossing around 1.3 Å for states 2 and 3, and a wide state crossing around 1.9 Å for states 1 and 2. However, as we move away from the crossings, the curves in plot 4.10(b) approach zero along the OH dissociation, but in plot 10a we still see significant NAC values at large values of the dissociation coordinate. Therefore we carried out N/D diabatization by using in the numerator only the NAC components shown in Fig. 4.10(b).

The partial derivative differences used in the denominator for state pairs 1 and 2,1 and 3, and 2 and 3 are shown in Fig. 4.10(c) as functions of the OH distance.

Figure 4.11 shows the adiabatic potential energy curves and the diabatic potential energy curves and squares of the diabatic couplings obtained by the N/D method. Both of the avoided state crossings in the adiabatic representations have smooth state crossings in the diabatic representation. One can see a significant coupling for U_{13} at 1.3 Å. At this

geometry, the diabatic energy difference of the two coupled states is large (~ 4.2 eV), thus this coupling barely affects the shapes of the potential curves.

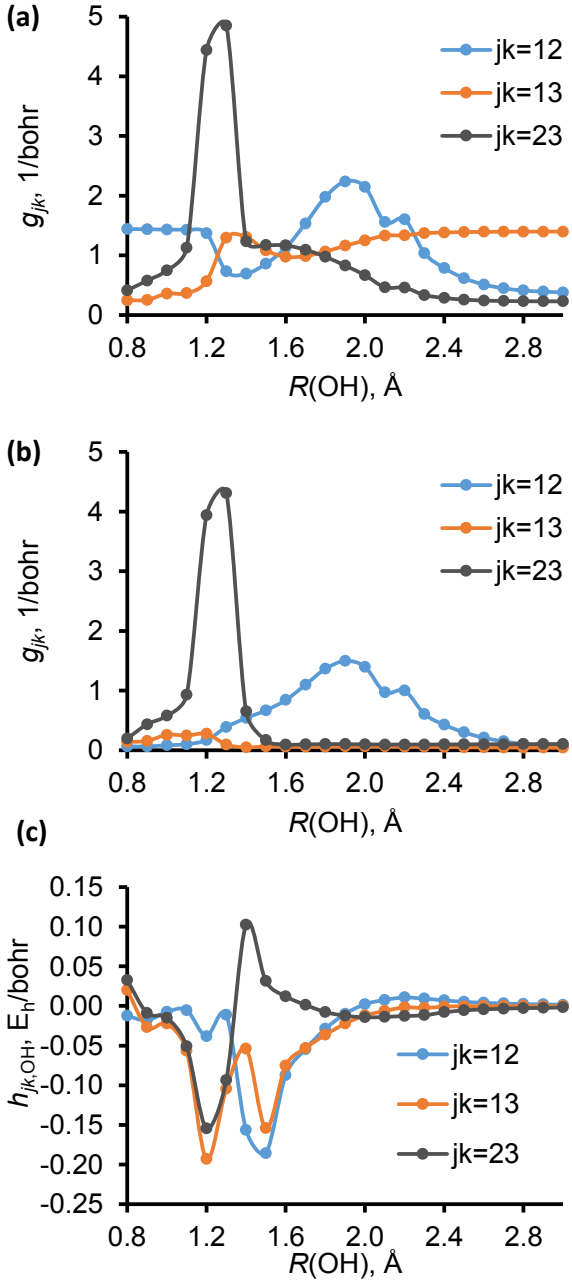

Figure 4.10. Input data for the N/D diabatization of phenol: (a) magnitude of all NAC components, (b) magnitude of the NAC components of oxygen and the dissociating hydrogen, and (c) differences between adiabatic energy gradients with respect to the dissociating OH internuclear distance.

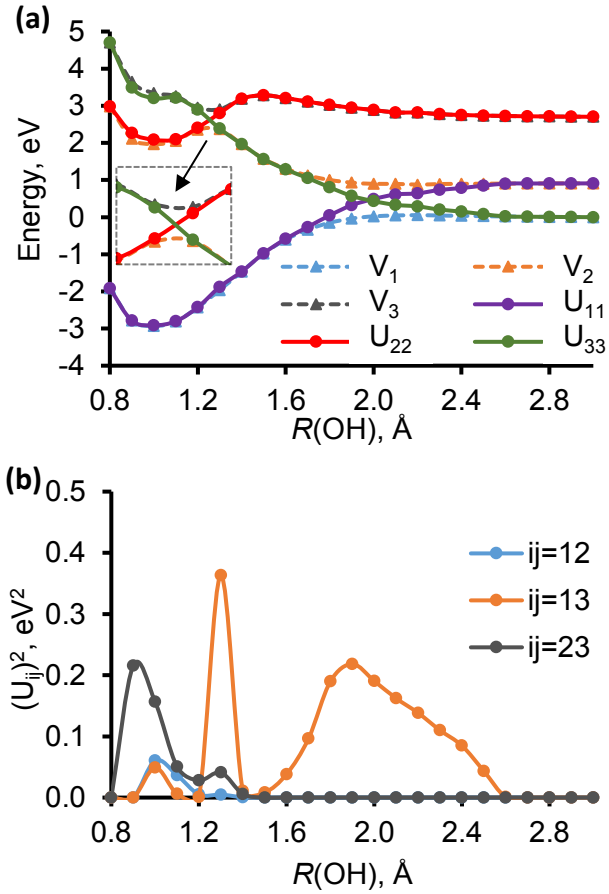

Figure 4.11. (a) Adiabatic and diabatic curves and (b) diabatic couplings of phenol dissociation ($\theta = 45°$).

4.3.6 O_3 system

The O_3 system was previously treated with DQΦ.[104] In that paper, two cuts of the first two $^1A''$ singlet states along the asymmetrical ozone stretch were shown where the three oxygen atoms were fixed at 120 and 100 degrees, and one of the bond lengths was also fixed. The other bond length was varied to show the avoided crossing of the first two $^1A''$ singlet states along the asymmetrical ozone stretch. In that article, the NAC curves along the bond stretch were presented (see Figs 19 and 22 in Ref.[104]) and they clearly show the coupling between the two states of interest. Here we apply the N/D method to this problem.

In the new calculations, the first three $^3A'$ states were calculated. The bond angle of the three oxygen atoms was fixed at 175 degrees, i.e., the atoms are almost collinear. One of the bond lengths was fixed at the equilibrium distance of O_2 molecule, R_e = 1.208 Å. The other bond length was varied between 1 and 3 Å. At large $O_2(\ ^3\Sigma_g^-) + O(^3P)$ distances, the first two $^3A'$ states correspond to the threefold degenerate ground state of $O(^3P)$ atom (the third component of the ground state is the first $^3A''$ state). The first excited asymptote corresponds to the $O_2(\ ^1\Delta_g\ ) + O(^3P)$ combination. This asymptote has six fold spatial degeneracy, with three $^3A'$ and three $^3A''$ states. The second excited $^3A'$ state is one of these six states in the $^3A'$ representation. For a complete treatment, one should include all low-energy states, but the three states considered here are enough to enough to compare DQΦ to the new N/D method.

Figure 4.12 shows that as the distance between the molecule and the atom is decreased, the adiabatic energy of the first excited state (orange dashed curve) increases more rapidly than the adiabatic energy of the ground state (blue dashed curve). Around 1.8 Å, there is a locally avoided crossing for the first and the second (gray dashed curve) adiabatic excited states. Both the first and the second adiabatic excited-state potentials show breaks at 1.3 Å. This is a clear sign of further avoided crossing with higher energy states not present in this plot.

Figure 4.12(a) shows a diabatization solution based on DQΦ method (in the notation of the DQΦ method,[104] the parameters are γ = 1.0 a.u. for the dipole, α = 1.0 a.u. and origin at center of mass for the quadrupole, and β = 1.0 a.u. for the electrostatic potential at the center of mass). Many other combinations of γ, α, β and origins were tried, but none of them could qualitatively improve the diabatization scheme. As it can be seen, the predicted diabatic energy curves (purple, red, and green) become degenerate, i.e., the DQΦ method is not successful.

The N/D diabats are much better; they smoothly cross, as shown in Fig. 4.12(b). For this diabatization the magnitude of the all NAC components was used; see Fig. 4.13(a). According to the NACs, we expect three state crossings along the O_2 + O reaction path. Starting from longer distance, there is a coupling for states two and three (g_{23}) at 1.8 Å. Then the ground and the first excited states should cross (g_{12}) around 1.6 Å. Finally, states two and three (g_{23}) have to cross, again, at 1.4 Å. We label the central O as atom 1; in the denominator the gradient difference from both r_{12} and r_{13} were used with 1.0 and -1.0 weights. Again the N/D method provides acceptable and useful results.

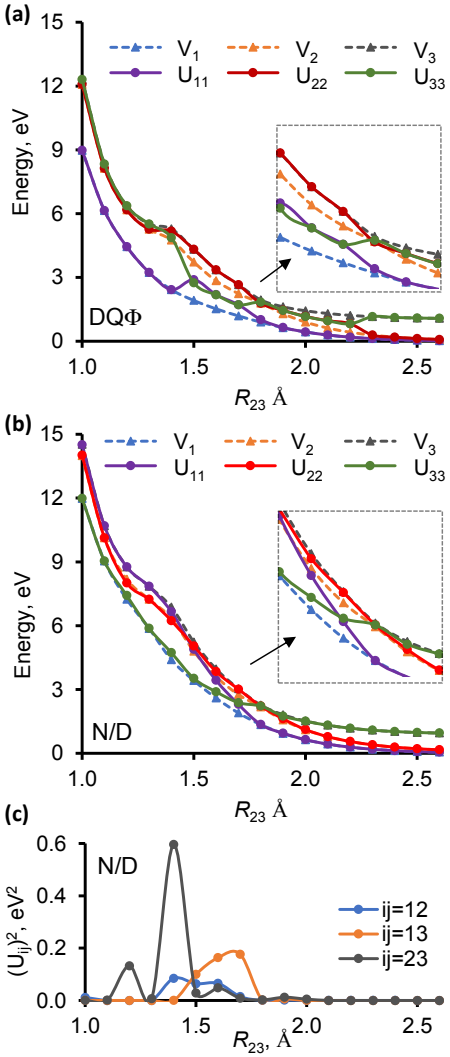

Figure 4.12. Adiabatic and diabatic potential energy curves of an $^3A'$ $O_2(\,^3\Sigma_g^-)$ + O(^{3}P) collision. Diabats calculated with (a) DQΦ, (b) N/D method, and (c) diabatic coupling from N/D

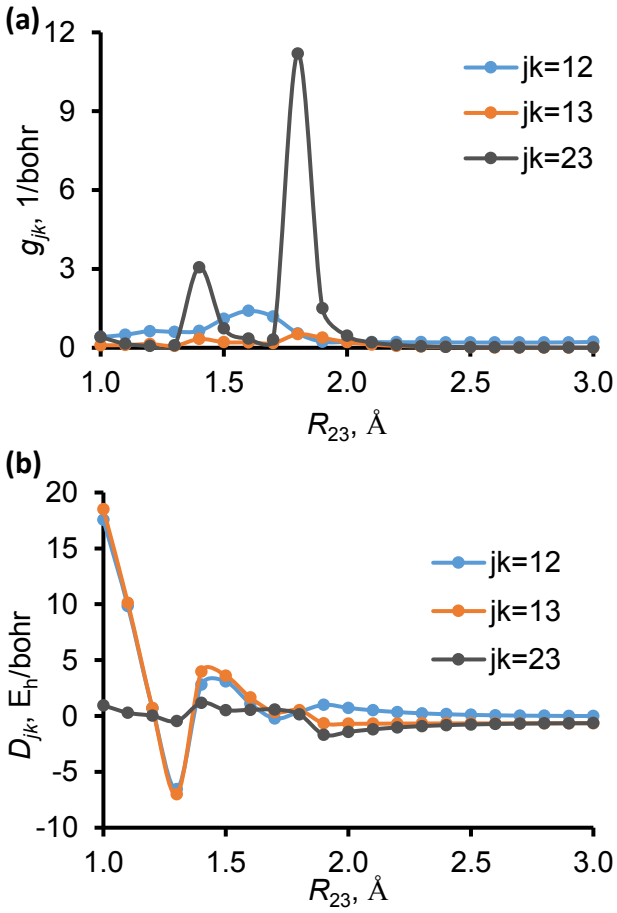

Figure 4.13. Input data for N/D diabatization for O_2 + O reaction: (a) magnitude of all NAC components and (b) selected denominators in eqn (20)

4.4 Conclusions

Diabatic states can provide chemical insight into an electronically adiabatic system by uncovering the smooth electronic configurations that underlie the adiabatic states. In principle, one could use only the nonadiabatic couplings to carry out diabatization; however, we show here that incorporation of the adiabatic energy gradients into the procedure makes the diabatization process very convenient because the difference of the energy gradients carries useful information about the underlying diabatic states. The

chapter shows how the nonadiabatic couplings and the gradients of the adiabatic states, when used together, provide a convenient way to uncover the underlying diabatic states. In addition to providing chemical insight, diabatization is useful for enabling fitting of potential energy surfaces and couplings so one may carry our simulations of dynamics.

The N/D method is a direct, orbital-independent diabatization scheme. It is adiabatic-equivalent and can therefore be converted back to an adiabatic representation by diagonalizing the diabatic Hamiltonian matrix. One can then use the adiabatic or diabatic representation to carry out dynamics simulations and study reaction rate constants, energy transfer rate constants, and photochemical mechanisms. We showed that the N/D method can be successfully applied to systems previously analyzed with the fourfold way and the DQΦ method including LiF, $(H_2)_2$, Li + HF, and phenol. We also provide successful applications to the H + H_2 reaction and O + O_2 interactions. The N/D method avoids working with orbitals, which makes the N/D scheme easier to use than the fourfold way. We applied the DQΦ and N/D methods to the three $^3A'$ triplet states of O_3 and showed that while the DQΦ method failed to give smooth, reasonable diabats, the N/D method was successful; the three adiabatic properties included in the DQΦ method failed to distinguish diabatic states, but the N/D method included sufficient information about the adiabatic states to discover underlying diabats.

The N/D method requires some system dependent decisions, but this is a common requirement for diabatization methods. For the N/D method these decisions include choosing the nonadiabatic coupling vector components and adiabatic gradient components and weights as well as thresholds and scaling factors. Although further analysis might lead to systematic ways to choose these parameters, in all six cases considered here we were able to find suitable values of the parameters.

5 Extended Hamiltonian molecular dynamics: Semiclassical trajectories with improved maintenance of zero point energy

Adapted with permission from Yinan Shu, Sijia S. Dong, Kelsey A. Parker, Junwei L. Bao, Linyao Zhang, and Donald G. Truhlar, Phys. Chem. Chem. Phys. **20**, 30209 (2018)

It is well known that classical trajectories do not maintain ZPE in the final states, which can lead to very unphysical behavior. In this chapter a new molecular dynamics method called extended Hamiltonian molecular dynamics (EHMD) is presented that improves the ZPE problem in classical molecular dynamics. In EHMD, two images of a trajectory are connected by one or more springs. The EHMD method is tested with the Henon-Heiles Hamiltonian in reduced and real units and with a Hamiltonian with quartic anharmonicity in real units, and the method is found to improve zero-point maintenance as intended.

5.1 Zero Point Energy Leakage

Advances in theoretical methods and computational power have made molecular dynamics (MD) simulations a powerful tool to investigate physical and chemical processes. Among various MD methods, classical trajectories and quasiclassical trajectories (which are classical trajectories with quantum mechanical selection of initial conditions) stand out as the most popular.[114-122] Despite the success of these methods, the use of classical trajectories suffers from two major problems, namely neglect of tunneling and failure to enforce the requirement of zero point energy (ZPE). To alleviate these problems, various semiclassical methods have been suggested, but these methods raise the cost and complexity of the calculations and sometimes have other limitations, for example they may be limited to simulating thermally averaged ensembles. Therefore, it is worthwhile to look for a simpler scheme that requires minimal changes to conventional classical trajectory propagation. In recent work we have shown how to include tunneling in classical trajectories.[123] Here we present a proposal to alleviate the ZPE problem.

The ZPE problem studied here is the phenomenon that in classical trajectories on anharmonic systems (and all real molecules are anharmonic), the high-frequency modes leak energies into the low-frequency modes or relative translation of fragments without the constraint of the quantum mechanical effect that the ZPE is the lowest allowed energy in a vibrational mode. The partition of ZPE into individual modes is not unique except for systems with no rotation and a quadratic (i.e., harmonic) vibrational potential; nevertheless most molecules have small enough anharmonicity that a harmonic calculation of the energy in a given mode should not yield an energy significantly below the harmonic zero point energy. Thus the dynamics of an isolated molecule should maintain ZPE in each mode to within the accuracy of the harmonic approximation. However, it is well known that classical mechanics does not maintain the ZPE in each mode. Strictly speaking, ZPE is required only for stationary states, such as the reactants and products of a chemical reaction, but it is reasonable to expect ZPE to be approximately maintained in spectator modes, and we know that approximate ZPE maintenance is important even in active modes at transition states.[124-126] Furthermore, the simulation of reactions by classical mechanics may produce species whose total vibrational energy is less than the total ZPE; in such a case, reactions may occur at energies that are energetically forbidden according to quantum mechanics. Such unphysical behavior of classical trajectories can also cause spurious energy transfer or artificial dissociation of a molecular system. These problems have been well studied.[127-135] The ZPE problem originates from the fact that the classical trajectories can enter regions of the phase space that correspond to energy distributions not allowed by quantum mechanics.[136-138]

Many strategies have been proposed to tackle the ZPE problem of classical trajectories. These strategies can be generally classified into three types: (i) active methods, in which individual trajectories or ensemble behaviors are altered such that the

regions of the phase space forbidden by QM are avoided in classical trajectories.[65, 139-148] (ii) passive methods, in which unphysical trajectories are simply discarded from the final statistics.[128, 149-156] (iii) methods that incorporate quantum mechanical effects in trajectories, for example, path-integral-based MD schemes,[121, 157-165] Bohmian dynamics,[166] and other semiclassical dynamics schemes.[167-171] Most of these methods deal with individual trajectories, although from one point of view ZPE maintenance is the property of an ensemble of trajectories.[137-138] A disadvantage of active methods is that they may have drastic effects on the time evolution of the classical trajectories.[141, 144-145]

Here we present a simple and computationally efficient ansatz that reduces the ZPE problem in classical trajectories. We call this new method extended Hamiltonian molecular dynamics (EHMD). The EHMD method maintains the simplicity of classical trajectories as much as possible. The goal of EHMD is not to achieve accurate quantum results, but rather to define semiclassical trajectories whose mode energies behave more quantum mechanically than those in purely classical trajectories, and thus to enable more realistic classical-like simulations of problems where the ZPE problem is a significant detriment to the ability of classical or quasiclassical simulations to interpret experimental results.

5.2 Extended Hamiltonian Theory

Consider a system with F vibrational degrees of freedom. Here we treat all degrees of freedom semiclassically; extensions to many-body Hamiltonians including translation and rotation and where some coordinates are treated semiclassically and others classically are possible but are relegated to possible later work. We use isoinertial coordinates with all masses scaled to a reduced mass of μ. Then the Hamiltonian is

$$H = \frac{1}{2\mu}\sum_{m=1}^{F} p_m^2 + V(q_1, \ldots, q_F) \tag{1}$$

where q_i is a vibrational coordinate, and p_i is its conjugate momentum. The extended Hamiltonian is then

$$H_{ext} = \sum_{\gamma=1}^{2}\left[\frac{1}{2\mu}\sum_{m=1}^{F}\left(p_m^{(\gamma)}\right)^2 + V\left(q_1^{(\gamma)}, \ldots, q_F^{(\gamma)}\right)\right] + \frac{1}{2}\sum_{m=1}^{F}\kappa_m\left(q_m^{(1)} - q_m^{(2)}\right)^2 \tag{2}$$

where κ_m is a user-defined spring constant. The first sum represents two images of a trajectory, and if the spring constants were zero, these would just be two independent trajectories. The second sum in eq 2 couples the images. The equations of motion for EHMD are purely classical, i.e.,

$$\dot{p}_m^{(\gamma)} = -\frac{\partial H_{ext}\left(p_1^{(1)}, \ldots, q_m^{(2)}\right)}{\partial q_m^{(\gamma)}} \tag{3}$$

$$\dot{q}_m^{(\gamma)} = \frac{\partial H_{ext}\left(p_1^{(1)}, \ldots, q_m^{(2)}\right)}{\partial p_m^{(\gamma)}} \tag{4}$$

5.3 The Henon-Heiles Hamiltonian

First we use the Henon-Heiles system to illustrate the behavior of EHMD because the Henon-Heiles system of two coupled oscillators[172-173] ($F = 2$) has been widely employed to investigate the ZPE problem in classical MD.[137, 139, 141, 144-145, 174] The Henon-Heiles Hamiltonian is given by eq 1 with

$$V(q_1, \ldots, q_F) = \frac{1}{2}k_1 q_1^2 + \frac{1}{2}k_2 q_2^2 + \lambda\left(q_1^2 q_2 - \frac{1}{3}q_2^3\right) \tag{5}$$

where

$$k_m = \mu\omega_m^2 \quad (6)$$

and ω_m is the vibrational frequency in radians/s. The frequencies in radians/s are related to the frequencies ν_m in wave numbers by $\omega_m = 2\pi c\nu_m$, where c is the speed of light.

In the present work, the initial conditions for an ensemble of trajectories are selected by random sampling of the harmonic part of the Hamiltonian. To be more specific, we assign a random number from a uniform distribution in the interval $(0,2\pi)$ to each vibrational phase $\phi_m^{(\gamma)}$ and assign the momenta and coordinates by

$$p_m^{(\gamma)} = \sqrt{(2n_m + 1)\hbar\mu\omega_m}\sin\phi_m^{(\gamma)} \quad (7a)$$

$$q_m^{(\gamma)} = \sqrt{(2n_m + 1)\hbar/(\mu\omega_m)}\cos\phi_m^{(\gamma)} \quad (7b)$$

where n_m is the vibrational quantum number. The mode energies along the trajectory are functions of time defined harmonically as

$$E_m^{(\gamma)} = \frac{1}{2\mu}\left(p_m^{(\gamma)}\right)^2 + \frac{1}{2}\mu\omega_m^2\left(q_m^{(\gamma)}\right)^2 \quad (8)$$

where the justification for using harmonic energies to monitor ZPEs was discussed in the introduction. We will consider two kinds of cases, first using the reduced units in which the Henon-Heiles system is usually studied and then using real units to make a connection with realistic levels of anharmonicity for real molecules. The reduced units are widely employed in previous work and hence provide a touchstone to connect to that work. The modeling results with real units will show how EHMD behaves for systems with realistic molecular parameters. For example, the Henon-Heiles model Hamiltonian can be employed to approximate the vibrations of linear CO_2.[175]

An ensemble of 500 trajectories was computed for each case with ,

which means the harmonic energy of each mode equals the harmonic ZPE at the beginning of the trajectory. For EHMD, the mode energies are computed as the average of the two images, and the ensemble averages are therefore averages over 1000 images.

5.3.1 Examples in reduced units

In the reduced unit case, $\mu = 1$ and $\hbar = 0.06$. The mode energies as functions of time are shown in Figure 5.1. The first two systems considered here correspond to (a) $\omega_1 = \omega_2 = \lambda = 1$ and (b) $\omega_1 = 1.7, \omega_2 = 1, \lambda = 1.5$. System (a) is a case that has been studied in previous work.[137, 141] For EHMD, we set $\kappa_1 = \kappa_2 = 0.1$ for system (a) and $\kappa_1 = 0.34, \kappa_2 = 0.15$ for system (b). The mode energies of the EHMD and classical MD results are shown in Figure 5.1.

In Figure 5.1(a), the modes have the same frequency; hence both modes have the same energy at the beginning of the trajectory. The classical MD mode energies show large energy flows between the modes, and the two mode energies end up differing by about 0.004 energy units after 500 time units. The EHMD mode energies are more stable than the classical ones, and – although we still see some level of ZPE leaking between the two modes – we do not see one mode losing a large amount of energy to the other. The EHMD results are much better than the passive methods reported before,[137] and they are comparable to the active method.[141]

Figure 5.1(b) shows an example where two modes have different frequencies. The mode energies start with ZPEs of 0.051 and 0.030. In about 200 reduced time units, the two mode energies of the classical simulation become very close to 0.041, which indicates a significant ZPE leakage from the high-frequency mode to the low-frequency mode. In contrast, in EHMD, although the two mode energies change rapidly at the beginning, they are stabilized after 100 time units, and they become close to 0.046 and 0.037 for modes 1 and 2 respectively. Thus at 500 time units the high-frequency mode has still not become classically equilibrated to the low-frequency one. Since the ratio of energy in the two modes stabilizes, it is possible that one could improve the results even

further by devising a better way to select the initial conditions of the ensemble, but we do not pursue that here.

In Figure 5.1(c), we show an example corresponding to Fermi resonance, where the ratio of the frequencies is 2:1; in particular we have $\omega_1 = 2.0, \omega_2 = 1, \lambda = 1$. The initial mode energies are 0.06 and 0.03. Classical MD results clearly show energy flow from the high-frequency mode to the low-frequency mode, and the two mode energies become nearly the same in about 400 time units; EHMD shows some leak from the high-frequency mode to the low-frequency mode in about 50 time units, but the mode energies are stable after that.

Thus the EHMD method is a significant improvement over classical MD in all three cases.

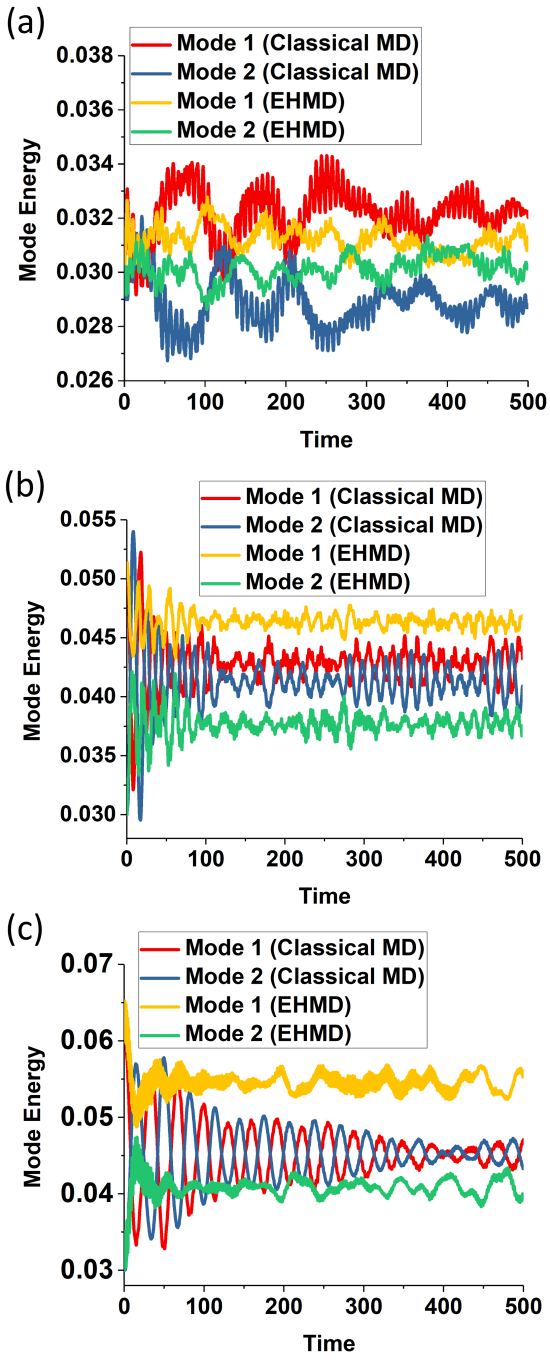

Figure 5.1. Two mode energies as a function of time for classical MD and EHMD with the Henon-Heiles system

5.3.2 Examples with cubic anharmonicity and real units

We next consider three systems with realistic units based roughly on real systems: (A3) a system with frequencies equal to the asymmetric and symmetric stretching modes of CO_2 with frequencies, $\nu_1 = 2565$ cm^{-1} and $\nu_2 = 1480$ cm^{-1} (1 cm^{-1} corresponds to 11.96 J/mol); (B3) a system with frequencies equal to the H_2O symmetric and asymmetric stretching modes with frequencies $\nu_1 = 3585$ cm^{-1} and $\nu_2 = 3506$ cm^{-1}; and (C3) a system with frequencies equal to the H_2O symmetric stretch and bending frequencies, $\nu_1 = 3585$ cm^{-1} and $\nu_2 = 1885$ cm^{-1}. We set μ equal to the reduced mass of CO for case A and to the reduced mass of OH for systems B and C. The numerical value of the anharmonic constant λ is set to $0.5(k_1 + k_2)/a_0$ (where a_0 is a bohr; 1 $a_0 = 0.5292 \times 10^{-10}$ m) in cases A3 and B3, which is a reasonable approximation to a higher-order force constant for the bond stretching modes.[176-177] For system C3, we set λ equal to $0.25(k_1 + k_2)/a_0$. The spring constants κ for the EHMD calculations are (in the usual units of mdyne/Å, where 1 mdyne/Å = 1 N/cm): (A3) $\kappa_1 = 1.713$, $\kappa_2 = 2.911$, (B3) $\kappa_1 = \kappa_2 = 0.623$, (C3) $\kappa_1 = 0.4050$, $\kappa_2 = 0.7784$.

Parts (a), (c), and (e) of Figure 5.2 show the classical MD mode energies as functions of time in red and blue and the EHMD mode energies as functions of time in yellow and green for systems A3, B3, and C3, respectively. The figures show that EHMD preserves ZPE much better than classical MD. The EHMD mode energies are stabilized after ~200 fs in all three systems. However, in classical MD, we can see a strong oscillatory energy flow between the two modes during the whole simulation time for systems A and B. For system C, the two mode energies become very close to each other after 300 fs.

To obtain a better quantitative understanding of the differences between the trajectories of classical MD and EHMD, we computed the histogram of mode energy

distribution along the trajectories, and these are shown in Figs. 5.2(b), 5.2(d), and 5.2(f). One can see that, in all cases, the mode energy distribution for EHMD is much narrower than classical MD. We do see some ZPE leaking from the most probable mode energies in EHMD; however, the leakage is much smaller than in classical MD.

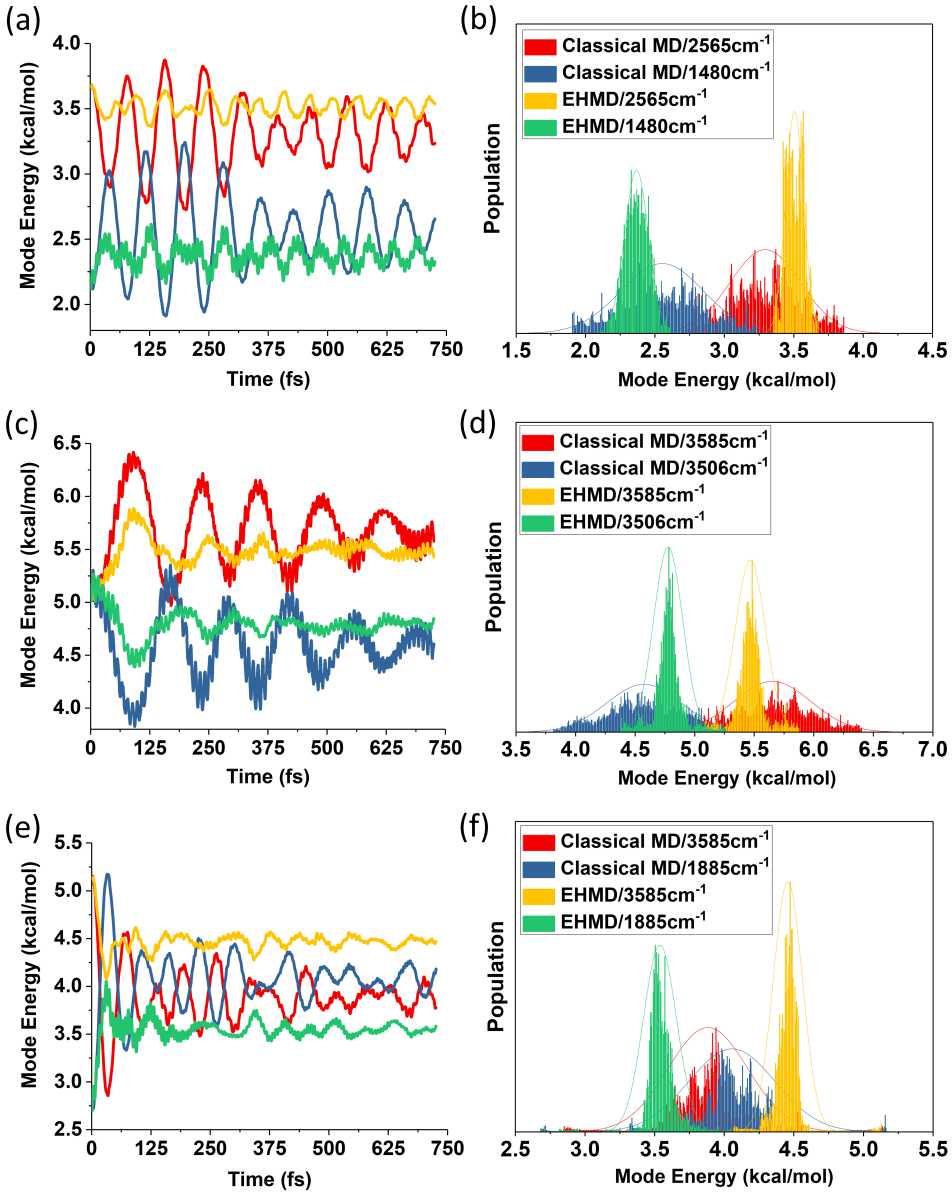

Figure 5.2. (a,c,e) Mode energies as functions of time for classical MD and EHMD for the Henon-Heiles system and (b,d,f) histograms of mode energies distribution for classical MD and EHMD where top, middle, and bottom plots correspond respectively to systems A3, B3, and C3, described in the text.

At the present time, we have not determined the optimum way to set the κ_m values. In our experience, the quality of the trajectory results is not overly sensitive to the κ_m values, by which we mean that the ensemble-averaged mode energies are stable within certain ranges of κ values. However, the best results are usually obtained with κ values that are about 10 to 20 percent of the quadratic force constant of the target mode. Here target mode means the mode into which the energy is leaking. All force constants used for Figure 5.2 are given in the Table 5.1, which shows that the three values of κ_1/ k_2 are all in the range 9–21%, and the three values of κ_2/ k_1 are all in the range 9–11%. Figure 5.3 shows an example for system A with three other sets of κ_m values, which differ by as much as 29% from those in in Figure 2(a); all the EHMD results show very similar behavior.

Table 5.1. The quadratic force constants k_1 and k_2 in units of N cm^{-1}, the cubic anharmonicity parameter λ in units of N cm^{-1} Å^{-1}, and the spring constants κ in units of N cm^{-1}.

System	A3	B3	C3
k_1	26.581	7.128	7.128
k_2	8.850	6.818	1.971
λ	33.478	13.177	4.299
κ_1	1.713	0.623	0.4050
κ_2	2.991	0.623	0.7784

Note that 1 N/cm is the same as the conventional force constant unit of 1 mdyn/Å, and 1 N cm^{-1} Å^{-1} is the same as 1 mdyn/Å^2.

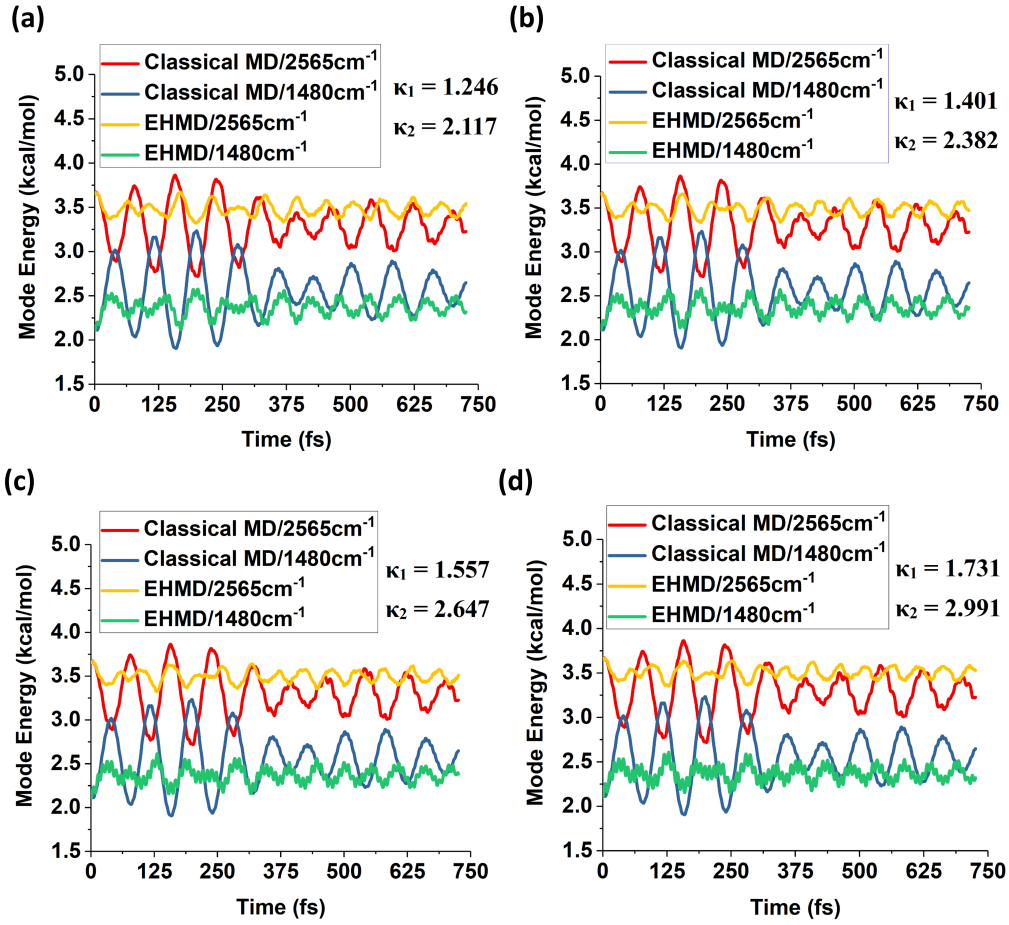

Figure 5.3. The classical and EHMD mode energies as functions of time for the Henon-Heiles system A with different κ parameters: (a) $\kappa_1 = 1.246$, $\kappa_2 = 2.117$; (b) $\kappa_1 = 1.401$, $\kappa_2 = 2.382$; (c) $\kappa_1 = 1.557$, $\kappa_2 = 2.647$; and (d) $\kappa_1 = 1.731$, $\kappa_2 = 2.991$, where force constants are in N/cm.

5.4 Test for a Hamiltonian with quartic anharmonicity

To further demonstrate the generality of our method, we have also tested a system with quartic anharmonicity. The Hamiltonian is given by eq 1 with the following potential

$$V(q_1, \ldots, q_F) = \frac{1}{2}k_1 q_1^2 + \frac{1}{2}k_2 q_2^2 + \lambda(q_1 - q_2)^4 \qquad (9)$$

where k_m is defined in eq 6, and q_m is defined in eq 8. As examples, we considered systems like A3 and C3 that were tested with the Henon-Heiles Hamiltonian with real

units. For both new systems, which will be called A4 and C4, the reduced mass and frequencies are defined in the same way as the real-unit examples for the Henon-Heiles Hamiltonian. The anharmonic constant λ is set to be $l(k_1 + k_2)/a_0^2$, where l is a parameter to be varied to see the effect on the results. The numerical values of the force constants are summarized in Table 5.2.

Table 5.2. The quadratic force constants k_1 and k_2 in units of N cm^{-1}, the quartic anharmonicity parameter λ in units of N cm^{-1} Å^{-2}, and the spring constants κ in units of N cm^{-1}.[a]

System	A4	C4
k_1	26.772	7.178
k_2	8.913	1.985
λ	63.717,[b] 127.434[c]	8.180d,[d] 16.360[b]
κ_1	2.335	0.1479
κ_2	0.7784	0.07784

[a] Note that 1 N/cm is the same as the conventional force constant unit of 1 mdyn/Å, and 1 N cm^{-1} Å^{-2} is the same as 1 mdyn/Å^3. [b] $l = 0.5$ [c] $l = 1$ [d] $l = 0.25$

Figure 5.4 compares the classical and EHMD mode energies of system A4 (l = 0.5, 1.0) and system C4 (l = 0.25, 0.5). As we can see from Figure 5.4, regardless of the choice of λ, the mode energies of the classical trajectories are more spread-out than those for EHMD, and the mode energies from EHMD are much more stable. Different choices of κ_m values have also been explored. Figures S1-S3 in the Electronic Supplementary Information (ESI) show that for each choice of the anharmonic constant λ, EHMD with a wide range of κ_m values can maintain the zero-point energy much better than classical MD. For system A4, for both $\lambda = 0.5(k_1 + k_2)/a_0^2$ and $\lambda = (k_1 + k_2)/a_0^2$, the EHMD mode energies are stable for κ_m/k_1 in the range 9–61% and for κ_m/k_2 in the range 3–20%. For system C4, for $\lambda = 0.25(k_1 + k_2)/a_0^2$, $\lambda = 0.5(k_1 + k_2)/a_0^2$, and $\lambda = (k_1 + k_2)/a_0^2$, the EHMD mode energies are stable for κ_1/k_1 in the range 2–42% and κ_2/k_2 in the range 4–80%. (For brevity, values outside these ranges are not discussed here.) From Figures S1 and S2, we notice that, if $k_1/k_2 > 1$, EHMD achieves better performance when $\kappa_1/\kappa_2 > 1$. These examples demonstrate that EHMD also works well for a system with quartic anharmonicity, and the result is robust with a wide range of force constants.

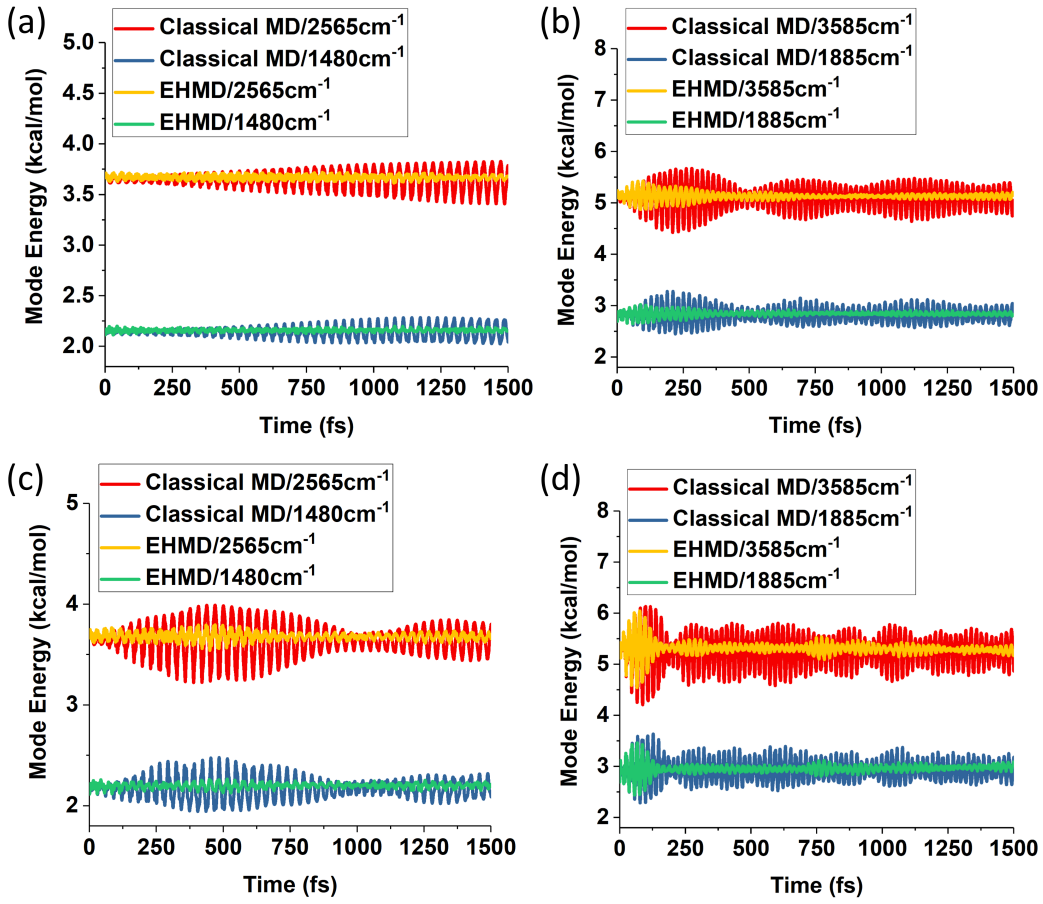

Figure 5.4. Comparison of the classical MD and EHMD with quartic anharmonicity for: (a) and (c): quartic system A4; and (b)and (d): quartic system C4. (a) $l = 0.5$, (b) $l = 0.25$, (c) $l = 1.0$, (d) $l = 0.5$.

5.5 Conclusions

The extended Hamiltonian is not designed to yield accurate quantum mechanical results, but rather to reduce the problem of ZPE leakage in the simplest possible way. The form of the spring term is motivated by the presence of harmonic springs in ring polymer MD (RPMD)[163-164] and by the linearized quantum force term in Bohmian dynamics with approximated quantum force (BD-AQP).[166, 178] These two simulation approximations have common elements, and our work has similar elements, in particular the use of

coupled trajectories to simulate the effect of the nonlocality of a quantum mechanical wave packet, but we have attempted to use these elements in a simpler way – by coupling only two trajectories. The RPMD equations involve all trajectories in a cyclic chain while the Bohmian approach developed by Garashchuk et al. connects all the trajectories to an averaged trajectory. In both cases, the individual trajectories experience a force from the other trajectories that can pull them closer together or push them further apart. The same is true for EHMD. Note that in EHMD, the restoring force of the spring ensures that the trajectories continue to remain close and affect one another. The comparison between RPMD, BD-AQP, and EHMD is schematically illustrated in Figure 5.5. Both RPMD and BD-AQP have had success in reducing ZPE leakage. Specifically, Habershon and Manolopoulos have shown that RPMD conserves ZPE for inter- and intramolecular modes of a water model better than the linearized semiclassical initial value representation,[160] and Garashchuk and Rassolov have shown BD-AQP conserves ZPE in a one-dimensional Morse oscillator as well as in modified multi-dimensional oscillators.[166] We emphasize the following important differences between EHMD and these methods: (i) The κ parameter in the EHMD extended term is not temperature dependent as in RPMD. (ii) The extended term (the potential energy in the springs) is associated with the difference of the coordinates in two trajectories, while in BD-AQP, the quantum force term is associated with the difference between the positions of individual trajectories and the center of a set of trajectories. (iii) EHMD is designed to be simpler than either of the more rigorous semiclassical methods, and the amount of work simply doubles, whereas it can go up by a large factor in the other methods.

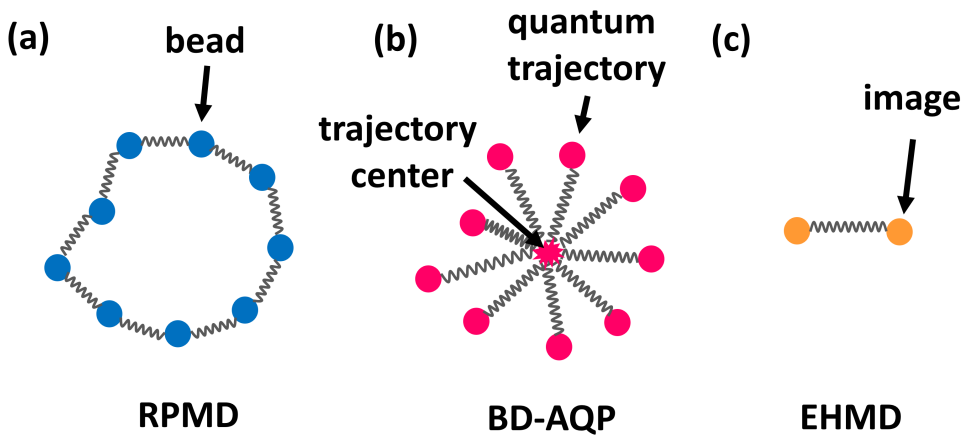

Figure 5.5. A conceptual illustration of the connected individual trajectories, in (a). RPMD, (b). BD-AQP, and (c). EHMD.

Another aspect of the similarity of the present method to a previous semiclassical method is the analogy to the displaced point path integral method;[179-180] here we have displaced trajectories rather than displaced points.

The strictly conserved energy in the extended Hamiltonian is the sum of the energies of two images plus the energy of the extended term. One can ask whether we see strong energy transfer between the extended term and the individual images. Figure 5.6 shows energies in the two springs and their sum for the A, B, and C systems with cubic anharmonicity with real units (Henon-Heiles systems of Figure 5.2). One can see that spring energies are roughly 10%-20% of the mode energies, and they are conserved very well during the time propagation. This indicates that although the energies of the individual images are not strictly conserved, they are approximately conserved very well in an average sense.

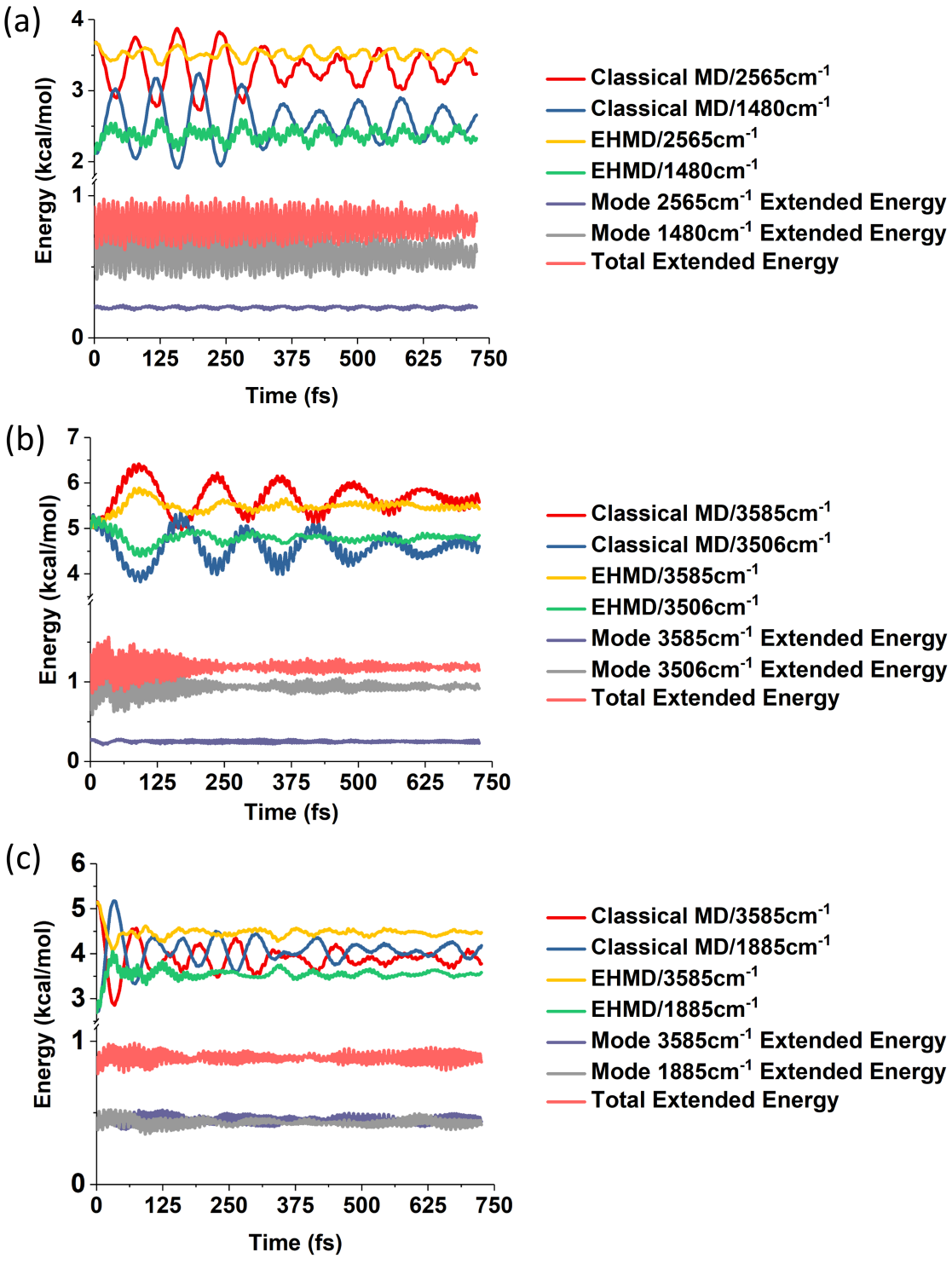

Figure 5.6. Classical MD and EHMD mode energies and the extended-term energy as functions of time for the Henon-Heiles systems: A3, B3, and C3 of Figure 5.2. The separate spring potential energies for the two modes the total energy of the extended term is also shown

We have interpreted the energies of the trajectories as being the energies of the images excluding the spring potentials. An alternative interpretation is shown in Figure 5.7, where we added half of each spring's potential energy into each of the two modes that are coupled by the spring. We can call the sums the augmented mode energies. Figure 5.7 shows the augmented mode energies the cubic A, B, and C systems of Figure 5.2. One sees the augmented mode energies are all shifted up for the EHMD, because we included the potential energy of the extended term here. This extra energy has similar behavior as in BD-AQP, where the quantum mechanical Gaussian will add some extra energy to the system. The augmented mode energies are much better conserved than the mode energies of classical MD.

In this chapter, we have presented a new semiclassical molecular dynamics method, called extended Hamiltonian molecular dynamics. The EHMD method is designed to improve the treatment of the ZPE in classical trajectories. In the extended Hamiltonian ansatz, a trajectory has two images coupled by springs. By employing the Henon-Heiles Hamiltonian as well as Hamiltonian with a quartic potential as test systems, we have shown that EHMD maintains ZPE much better than classical MD in eight test cases. Extensions and improvements are possible, but this work demonstrates the possibility to improve classical trajectory simulations in a very simple way.

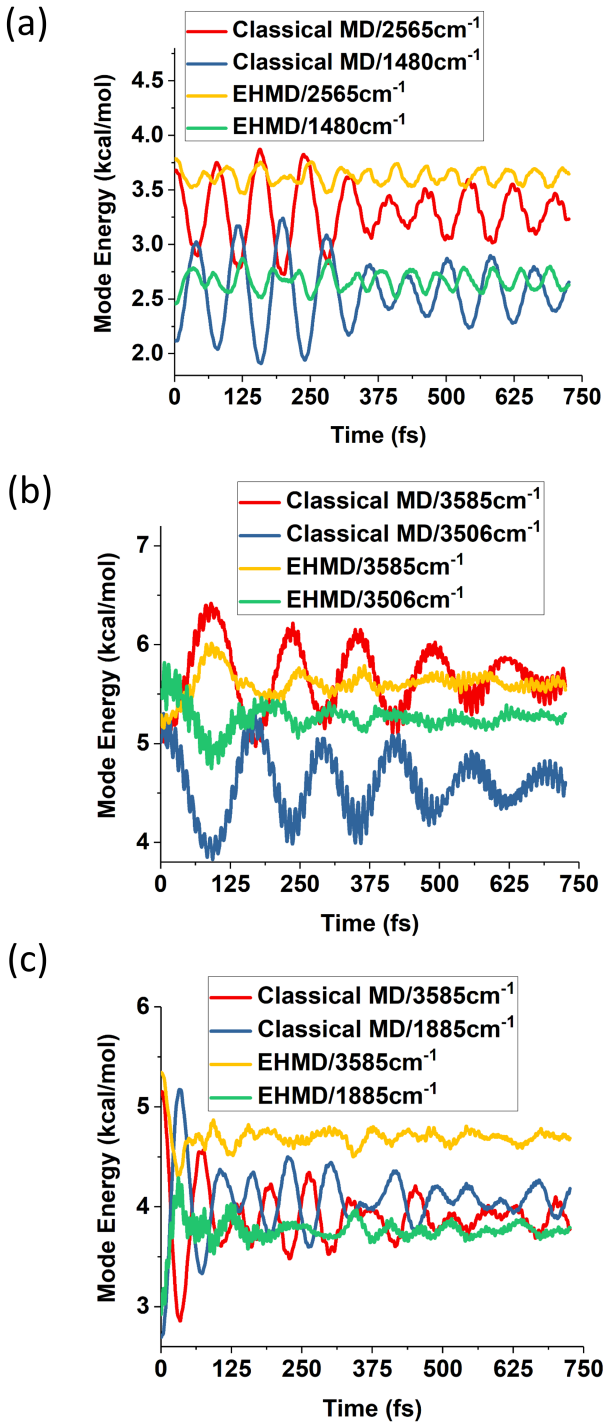

Figure 5.7. Classical and EHMD mode energies as functions of time for systems Henon-Heiles systems A3, B3, and C3 defined in the text. The mode energies for EHMD are defined by including one half of the potential energy of the spring for that mode.

6 Semiglobal Ground- and Excited-State Potential Energy Surfaces and the State Coupling for the N-H Photodissociation of Methylamine

Adapted from a manuscript under preparation for J. Chem. Phys. with authors Kelsey Parker and Donald Truhlar

We constructed an analytical, diabatic potential energy matrix (DPEM) that describes the N-H photodissociation of methylamine; the electronic state space includes the ground and first excited singlet states. Input for the fit was calculated by extended multi-state complete active space second-order perturbation theory (XMS-CASPT2). The data was diabatized using the dipole, quadrupole (DQ) diabatization method, in which we incorporated a coordinate dependent weighting scheme for the contribution of the quadrupole moments. To make the resulting surfaces semiglobal, we extended the anchor points reactive potential (APRP) method, a multiscale approach that assignes the internal coordinates to categories with different levels of computational treatment. Key aspects of the potential energy surfaces obtained by diagonalizing the DPEM agree with available experimental and theoretical data at energies relevant for photochemical studies.

6.1 Background

Upon photoexcitation with ultraviolet light, methylamine shows interesting dynamics that have been well studied but are not fully understood. The interesting photodynamics of methylamine coupled with its relatively small size make it a good test system to improve our understanding of photodynamic processes and to improve and test our computational methods for treating such systems. The first step in such a program of study is to obtain potential energy surfaces and their couplings, and that is the objective of this chapter.

Methylamine has been studied with many experimental and theoretical methods.[181-200] In 1963, Michael and Noyes detected dissociation reactions of methylamine after excitation to the first ultraviolet absorption band.[181] The dominate

dissociation pathway was found to be N-H dissociation, but C-H and C-N dissociations were also detected. These reactions were also detected by Butler and coworkers upon excitation at 222 nm in collision-less conditions.[182] Using Hartree-Fock calculations to study the ground and first excited singlet states (S_0 and S_1 respectively), Kassab et al. showed that S_1 corresponded to excitation of a nitrogen lone pair electron to a 3s Rydberg orbital.[183] Along N-H and C-N dissociation coordinates, this orbital assumes a σ^* character, and conical intersections (CIs) between the ground and first excited states were found along both dissociation coordinates. Building on this work, Dunn and Morokuma studied S_0 and S_1 along N-H, C-N, and C-H dissociation coordinates.[184] Along the N-H and C-N slices, they found barriers at short distances and conical intersections at larger distances in good agreement with Kassab. Both studies also noted a change in the amino structure from pyramidal to planar upon excitation to S_1. More recent work by Morokuma and coworkers[185] explored critical points on the two surfaces, which we compare to in our Results section. We are most interested in studying the N-H dissociation, but we will show that our diabatization method is also capable of treating the C-N and C-H dissociations.

The potential energy surfaces of methylamine can help us understand the system's interesting photodynamics. Ashfold and coworkers, using photofragment translational spectroscopy, studied the kinetic energy spectra of H photofragments, which they found to be bimodal.[186-187] They found that N-H dissociation dominates over C-H dissociation, and they assigned the fast and slow components of the H photofragments to two pathways for N-H dissociation with both pathways leading to ground-electronic-state products and with both pathways involving H atoms tunneling through or passing over a barrier at short N-H distances on the excited surface. More recent work supports their conclusion about the predominance of N-H dissociation.[188-193]

Several studies have looked into how vibrational excitation affects photodissociation,[188-195] including vibrational mode effects on reaction yields,[188-189] lifetimes,[191] average photofragment translation energy,[194] and branching ratios.[193-195] Comparison of deuterated verses non-deuterated species gives strong evidence of tunneling, which likely plays a major role for quick passage through the N-H barrier on the excited surface. Very recently Yarkony and coworkers[196] constructed a diabatic potential densrgy matrix (DPEM) for methylamine by fitting data collected via sampling the coordinate space with trajectories. Our approach is different from theirs but shares some key features with the methods they used; in particular, we both make use of a diabatic representation and we both prioritize regions of the DPEM that are important for dynamics.

To generate data for our fitting procedure we used extended multi-state complete active space second-order perturbation theory (XMS-CASPT2).[15] This data is in the adiabatic representation, which results from separating nuclear and electronic motion known as the generalized Born-Oppenheimer approximation. In the adiabatic representation, the energies (adiabats) are diagonal elements of the electronic Hamiltonian. Adiabatic states are coupled by the nuclear momentum and nuclear kinetic energy operators. For semiclassical calculations, one usually only deals with the coupling due to the nuclear momentum operator, and this vector is called the nonadiabatic couplings or NACs.[2] When adiabatic states approach one another, which is ubiquitous in photochemistry, the adiabatic state functions change rapidly and the adiabatic potentials become equivalent at conical intersection seams. These properties result in the adiabatic potentials having high-dimensional cuspidal ridges (called conical intersections or conical intersection seams) along nuclear coordinates and the NACs become large as the states approach and becoming singular along conical intersection seams.

In a diabatic representation, which is not unique, the NACs are negligible and the electronic wave functions change smoothly along the nuclear coordinates. The electronic Hamiltonian in a diabatic representation is nondiagonal and is called the diabatic potential energy matrix (DPEM); the elements of this matrix are the diabatic potentials on the diagonal and the diabetic couplings off the fiagonal and they are all smooth functions of nuclear coordinates.[2, 16] For fitting purposes, a diabatic representation is preferable compared to the adiabatic representation because the diabats and diabatic couplings can be fit to analytical functions and the NACs can be neglected. Throughout this work, the ground state and excited state will be referred to as S_0 and S_1 respectively, the adiabats for the ground and excited state will be referred to as V_1 and V_2 respectively, the ground and excited diabats as U_{11} and U_{22} respectively, and the diabatic coupling as U_{12}.

Converting from the adiabatic representation to a non-unique diabatic representation is called diabatization. Many diabatization methods have been developed without any method being considered the best approach in all circumstances. In this study, we used the dipole, quadrupole (DQ) diabatization method,[3, 104] which was developed in the Truhlar group. The DQ diabatization method makes use of two properties, the dipole and quadrupole, to distinguish diabatic states. The quadrupole contribution has an origin dependence, and the DQ method allows multiple quadrupole origins to be chosen. The contribution of the properties are weighted and the weights are chosen for the system of interest. In this study, we introduced coordinate dependent weights on the quadrupole contributions, and we show that this further generalizes the applicability of the DQ diabatization approach.

Analytical DPEMs and adiabatic potential energy surfaces (PESs), which are obtained by diagonalizing the DPEM, are very useful for dynamics as they are extremely cost effective, especially compared to direct dynamics. However, full DPEM are high-dimensional for any system larger than a couple of atoms. The number of degrees of

freedom of a DPEM, i.e., the number of independent variables upon which it depends, equals three times the number of atoms minus six. This means that methylamine has 15 degrees of freedom. If we planned to collect five data points along each degree of freedom, this would amount to 5^{15} data points in total, which is unfeasible. Collecting this much data would also be unnecessary for dynamics studies; many regions of the full DPEM are inaccessible at the energies reached by excitation to the first UV absorption band. Based on these considerations, we can see that this problem is a multiscale issue, where certain regions of the surface require consideration at a higher level of theory compared to regions which are less important and regions that are entirely unimportant for dynamics studies. In order to address these issues, the Truhlar group developed the anchor points reactive potential (APRP) scheme.[4]

The APRP scheme requires distinguishing the internal coordinates of the system into primary, secondary, and tertiary coordinates. The primary coordinates are the most important. Along these coordinates, electronic structure calculations are performed and the results (once diabatized) are fit to analytical functions to insure high accuracy. The secondary and tertiary coordinates depend on the primary coordinates. The secondary coordinates are treated in a similar fashion to the primary; electronic structure calculations are collected and the data is fit to analytical functions, which also depend on the primary coordinates. The tertiary coordinates do not depend on the secondary coordinates. The tertiary coordinates are treated at different 'anchor points', which are locations along the primary coordinate space. Between the anchor points, a tent function interpolates the tertiary contribution.

For our DPEM, we have two primary coordinates and all other coordinates were tertiary. In previous APRP studies,[4, 201-203] the tertiary contribution was derived by using Hessian data collected at the anchor points. In this work, at the anchor points we collected data along the tertiary coordinates. We then fit the energies to analytical

functions dependent on the tertiary coordinates. This made the tertiary coordinates approach more similar to the approach for secondary coordinates. Because we only collected data at anchor points, this modified scheme was still inexpensive. We made another modification to the APRP scheme with regards to the tent function. In previous work, to interpolate between the anchor points our group has used one or more one-dimensional tent function(s). This means that for a system with two primary coordinates, the anchor points were located along two independent primary coordinate spaces. The tertiary contribution would depend on both primary coordinates but the contribution along one primary coordinate was independent of the other primary coordinate. As an example, if there were three anchor points along one primary coordinate and three along the other, there were six anchor points in total. In this study, we used a two-dimensional tent function, which means that the tertiary contribution would depend on a two-dimensional primary coordinate space. In the example stated above, this means there would be a total of nine anchor points along the two-dimensional primary coordinate space.

In this paper, Section II briefly describes the DQ diabatization scheme and APRP method including modifications made to these methods. Section II also describes all the specifics of the analytical DPEM. Section III gives results of the DQ method and compares the adiabatic PESs resulting from our DPEM to XMS-CASPT2, density functional, and previous theoretical and experimental studies. Section IV summarizes the paper.

6.2. Methods and computational details

6.2.1. Electronic structure calculations

Electronic structure calculations were performed with the Molpro program package[63, 101] for the ground and first excited state by XMS(2)-CASPT2(6,6)[15] and the 6-31++G(d,p)

basis set.[102, 204-207] Symmetry was turned off. To avoid intruder states, a level shift of 0.3 E_h was applied. At this level of theory, the orbitals appear reasonable, and the calculations are fast enough to enable the optimization of the geometry of the ground state and to calculate adiabatic energies at the large number of geometries required as input for diabatization and fitting.

6.2.2. Diabatization

The calculations described in the previous subsection yield electronically adiabatic energies. These are not smooth functions of nuclear coordinates; the adiabatic potential energy surfaces approach one another and can become degenerate, resulting in cuspidal ridges at conical intersections. Furthermore, the adiabatic states are coupled by nonadiabatic couplings (NACs), which are vectors resulting from the action of the nuclear momentum operator on the adiabatic electronic wave functions, and these become singular at conical intersections. These features make the NACs and adiabatic PESs impractical to fit.

In this study, there are two adiabatic surfaces, which are transformed to a 2×2 diabatic potential energy matrix (DPEM) whose elements are matrix elements of the electronic Hamiltonian in the diabatic basis, in which this Hamiltonian is not diagonal. The diagonal elements are the diabatic surfaces U_{11} and U_{22}; the off-diagonal element is the diabatic coupling U_{12}. If the diabatization is successful, it circumvents this problem of the previous paragraph by producing a DPEM where the matrix elements are smooth functions of the nuclear coordinates, and the electronic states are smooth enough that the operation of the nuclear momentum operators on them may be neglected. Thus, in the diabatic representation, the coupling is provided by the smooth scalar off-diagonal elements of the electronic Hamiltonian (the diabatic couplings) rather than by the singular NAC vectors, and the potential energy surfaces (the diabatic potentials) are smooth

enough to be fit by analytical functions. The diabatic Hamiltonian can be transformed back to the adiabatic Hamiltonian by diagonalization, and the diabatization procedure we use is adiabatic equivalent, which means that the diabatic state functions span the same space as the two lowest adiabatic state functions so that the adiabatic potentials one gets by diagonalization are the original ones.

Diabatization was done using the DQ diabatization method published previously.[3, 104] This method makes use of two electronic properties, the dipole moment and the quadrupole moment, to distinguish diabatic states. These properties are defined as

$$\boldsymbol{\mu} = \sum_{i=1}^{N_{el}+N_{nuc}} q_i \boldsymbol{r}_i \tag{1}$$

$$Q^{(j)} = \sum_{i=1}^{N_{el}+N_{nuc}} q_i \left|\boldsymbol{r}_i - \boldsymbol{r}_j\right|^2 \tag{2}$$

where $\boldsymbol{\mu}$ is the dipole operator, q_i is the charge of particle i, $\mathbf{r}_i$ is the coordinate of particle i, and $Q^{(j)}$ is the traceless quadrupole at an origin, $\mathbf{r}_j$. The DQ method is carried out by maximizing

$$f_{\mathrm{DQ}} = \sum_{s=1}^{N_{states}} \left(w_\mu |\langle \psi_s | \boldsymbol{\mu} | \psi_s \rangle|^2 + \sum_{j=1}^{N_Q} w_j \left| \langle \psi_s \left| Q^{(j)} \right| \psi_s \rangle \right|^2 \right) \tag{3}$$

where ψ_s is diabatic state s, w_μ is a user determined weight on the dipole moment and w_j is a user determined weight at the quadrupole term at origin j, and N_{states} is the total number of states. Diabatic states are defined as linear combination of adiabatic states

$$\psi_s = \sum_{I=1}^{N_s} \phi_s T_{sA} \tag{4}$$

where ϕ_s are adiabatic states and $\mathbf{T}$ is a transformation matrix. The DQ method solves for the transformation that maximizes f_{DQ}.

In this work, quadrupole, origins were placed at each hydrogen (five sites) and at the carbon atom. Previous work with the DQ method on smaller systems mainly utilized constant weights on the different quadrupole contributions. For the present system, no constant weight we tried could give good diabats for all the regions tested. To overcome this problem, we used coordinate-dependent weights. The weights for the quadrupole moments at the hydrogen atoms are defined as,

$$w_{\mathrm{HX}}(r_{N-\mathrm{HX}}) = \omega_{QH} \cdot e^{-a_{N-H}\cdot\left(r_{N-\mathrm{HX}}-r_{N-H}^{[0]}\right)} \tag{5}$$

where w_{HX} is the weight term in eq. (3) for the quadrupole contribution at HX (X can be 1, 2, 5, 6, and 7; see Figure 6.1), $r_{N\text{-}HX}$ is the N–HX distance, ω_{QH} and a_{NH} are parameters, and $r_{NH}^{[0]}$ is the ground-state equilibrium N-H distance. The parameters are given in Table 6.1.

Table 6.1. Parameters for eq. (5)

Parameter	Values
ω_{QH} (a_0^{-2})	2.0
a_{NH} (Å^{-1})	3.0
$r_{NH}^{[0]}$ (Å)	1.01575

The weight on the quadrupole moments with their origin at the carbon is

$$w_{\mathrm{C}}(r_{C-N}) = \omega_{QC} \cdot e^{-b_{C-N}\cdot\left(r_{C-N}-r_{C-N}^{[0]}\right)^2} \tag{6}$$

where w_C is the weight term in eq. (3) for the quadrupole contribution at C, r_{C-N} is the C–N distance, ω_{QC} and b_{CN} are parameters and $d_{CN}^{[0]}$ is the ground-state equilibrium C-N distance. The parameters are given in Table 6.2.

Table 6.2. Parameters for eq. (6)

Parameter	Values
ω_{QC} (a_0^{-2})	10.0
b_{CN} (Å^{-2})	7.0
$r_{CN}^{[0]}$ (Å)	1.459744

The dipole weight, w_μ was 1 a_0^{-1} for all diabatization calculations in this study. Diabatization with these specifications lead to smooth diabats in the regions tested.

6.2.3 Analytic potential energy matrix

For fitting the diabatic potential energy matrix (DPEM), we calculated diabatic energies and couplings at a large number of geometries by the method discussed in the previous section. Methyamine has 15 internal digress of freedom, which is too many for a fully global fit, and so it was necessary prioritize certain regions of geometry to be fit with faithful accuracy; this determination was based on the goal of creating a DPEM suitable for simulating photodissociation. Upon photoexcitation, methylamine can dissociate via multiple pathways to different products; it can dissociate by breaking an N–H, N–C, or C–H bond. The N–H bond dissociation gives the highest yield in experiments with excitation into the first ultraviolet absorption band. The dissociated hydrogens have a bimodal translational energy distribution and the dynamics show mode dependency. The motion of the NH_2 'wag' is hypothesized to be important in explaining this behavior, and we use the H1-N-C-H2 improper torsion angle as a measure of the wag coordinate. The goal of this work is to obtain a PEM suitable for simulating these experiments. For this reason, the N–H1 bond coordinate and H1-N-C-H2 improper torsion angle are considered to be primary coordinates for the fit.

By classifying the coordinates as primary coordinates vs. other coordinates, we can convert an unfeasible problem of fitting a high-dimensional DPEM into a multiscale problem that is manageable. To do this, we use the anchor points reactive potential (APRP) method.[4] In APRP, coordinates important for dynamics are called primary and the less important, or spectator, coordinates are called secondary or tertiary. Here we only use the coordinates called primary and tertiary in the notation established for APRP. Electronic structure data points are collected along the primary coordinates with the tertiary coordinates unchanged. These energy data points are then fit with analytical functions. The energy contributions along tertiary coordinates are fit locally at certain points along the primary coordinates; these points are called anchor points. The tertiary

fits depend parametrically on the primary coordinates. For the present fit, the N–H1 stretch coordinate and H1-N-C-H2 improper torsion angle are primary coordinates, and the N–H2 stretch, two C–N–H bends, the C–N stretch, and multiple N–C–H bends, C–H stretches, H-C-H bends and torsions of the methyl and carbonyl hydrogens are tertiary coordinates.

6.2.4. General information about the fit

The notation in Figure 6.1 will be used to describe different structures. The figure also shows the value of the H1-N-C-H2 improper torsion angle, $\tau_{H1-N-C-H2}$, when CNH_2 is flat in a plane. Motion that simultaneously takes both H1 and H2 above or below this plane is referred to as the amino wag.

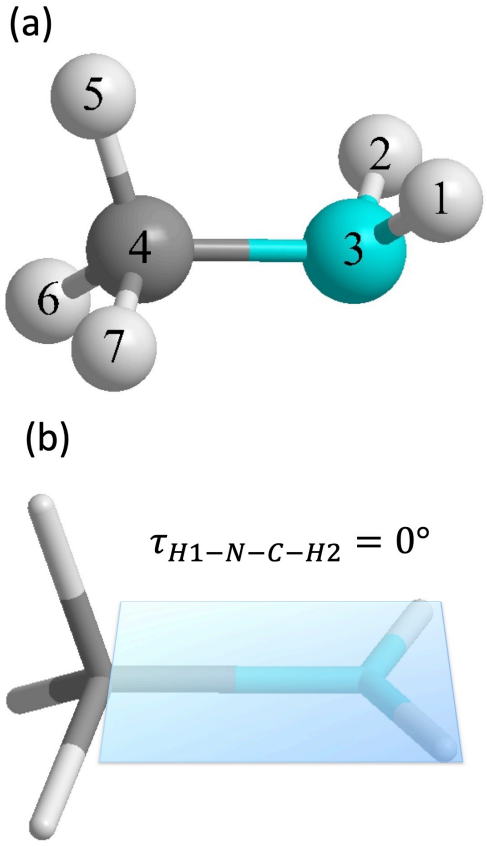

Figure 6.1. Methylamine with naming conventions at (a) the optimized ground-state geometry and (b) with the H1-N-C-H2 improper torsion set to 0°

Data was collected along a two-dimensional coordinate grid with the methyl group geometry fixed at the optimized ground-state equilibrium geometry. The grid has the N–H1 stretch varied from approximately 0.6 to 12 Å and the H1-N-C-H2 improper torsion varied from approximately 170° to 0°. The stretch coordinate was varied by 0.1 Å increments at small bond distances and by larger increments at larger bond distances. The improper torsion was varied by 10° increments. The improper torsion coordinate is convenient because it does not depend on N–H stretches and C–N–H bends of the amino group, which are accounted for in the other primary coordinate and in the tertiary coordinates.

In contrast to previous APRP studies,[4, 201-203] which used Hessian data and harmonic approximations for the tertiary coordinates, in this study, slices along tertiary coordinates were collected and fit locally to system-specific functional forms. This was done to give greater flexibility to the dependence of the DPEM on tertiary coordinates. The full list of tertiary coordinates studied via electronic structure data collection is: the H1-N-C bend, H2-N-C bend, H2-N stretch, C-N stretch, H7-C stretch, and H6-C-N bend. Tertiary stretches were varied by 0.1 Å at small bond distances with larger spacing as the bond distance increases. The bends were varied by increments of 2° to 10°. These calculations were performed with the primary coordinates at the different anchor point structures as detailed in the section below on the tertiary fit.

6.2.5. Primary fit

Parameters for all primary fit equations can be found in the Fortran subroutine available online at: https://comp.chem.umn.edu/potlib/. U_{11} data was fit to

$$U_{11}(r_{N-\mathrm{H1}}, \tau_{\mathrm{H1}-N-C-\mathrm{H2}}) = \kappa_x{}^{[11]}\left(1 - e^{-a_x{}^{[11]}(r-r_0)}\right)^2 + \kappa_y{}^{[11]} e^{-b_y{}^{[11]}\left(r-l_y{}^{[11]}\right)^2} + \kappa_z{}^{[11]}(cos(\tau) - cos(\tau_0))^2 \cdot e^{-b_z{}^{[11]}\left(r-l_z{}^{[11]}\right)^2} + \sum_{i=1}^{4} \kappa_i{}^{[11]}\left(e^{-\beta_i{}^{[11]}\left(cos\,(\tau)-t_i{}^{[11]}\right)^2}\right) \cdot \left(e^{-b_i{}^{[11]}\left(r-l_i{}^{[11]}\right)^2}\right) \quad (7)$$

In eq. (7), U_{11} depends on the N–H1 distance (r_{N-H1}) and the H1-N-C-H2 improper torsion coordinate ($\tau_{H1-N-C-H2}$). For these coordinates, subscripts are removed from the right hand side for brevity. In the first term, r_0 is the N–H1 equilibrium bond distance. The first and second terms are a Morse potential and Gaussian that fit the NH bond stretch with all other coordinates fixed at the ground-state equilibrium geometry. In the third term, the parameter, τ_0, is the improper torsion angle of the ground-state equilibrium structure. At small N-H1 bond distances, this term grows along amino wag motion that pushes the two hydrogen atoms away from the ground-state equilibrium structure. As the N-H1 bond distance increases, this term goes to zero due to the Gaussian multiple, which corresponds to the absence of interactions between the two hydrogens when H1 dissociates. The forth term is a summation of four Gaussian. This term also goes to zero as the N-H1 bond distance increases. The parameters were determined using Solver in Excel. (Solver was used for all the following fits as well.) The cosine of the improper torsion angle is used rather than the angle itself, which means U_{11} does not depend on the sign of the improper torsion. (All the following primary fits are also independent of the sign of the improper torsion.)

U_{22} data was fit to

$$U_{22}(r_{N-H1}, \tau_{\mathrm{H1}-N-C-\mathrm{H2}}) = c_x{}^{[22]} + \kappa_x{}^{[22]} e^{-a_x{}^{[22]}\left(r-l_x{}^{[22]}\right)} + \left(\kappa_y{}^{[22]}\left(r - d_x{}^{[22]}\right)^2\right) e^{-b_y{}^{[22]}\left(r-l_y{}^{[22]}\right)^2} \quad (8)$$

$$+\kappa_z{}^{[22]}(cos(\tau)-1)^2\cdot e^{-b_z{}^{[22]}\left(r-l_z{}^{[22]}\right)^2}$$
$$+\sum_{i=1}^{5}\kappa_i{}^{[22]}\left(e^{-\beta_i{}^{[22]}\left(cos\,(\tau)-t_i{}^{[22]}\right)^2}\right)\cdot\left(e^{-b_i{}^{[22]}\left(r-l_i{}^{[22]}\right)^2}\right)$$

In eq. (8), the first three terms are a fit along the N-H1 bond stretch with the amino hydrogens flat in a plane (Figure 6.1(b)) and all other coordinates at the ground-state equilibrium structure. In the forth term, the value, 1, comes from taking the cosine of the improper torsion angle when the amino structure is flat (cos(0°)=1). This term grows as the amino hydrogens approach one another. Similar to the U_{11} equation, the contribution from this term goes away along the N-H1 bond dissociation. The final term is a summation of five Gaussian, which also goes to zero as the N-H1 bond distance increases.

The diabatic coupling data, U_{12} is described along the two-dimensional primary coordinate grid by eq. (9). Similar to the equations for the diabats, this equation uses Gaussians along the stretch and improper torsion coordinates. The improper torsion angle also makes use of a semicircle-like equation with radius $(1.1)^{1/2}$. By setting the radius to $(1.1)^{1/2}$ instead of 1, the derivative is defined at 0° and 180°. U_{12} goes to zero as the N–H1 stretch distance increases to dissociation, which means the diabats approach the adiabats in that limit.

$$U_{12}(r_{N-\mathrm{H1}},\tau_{\mathrm{H1}-N-C-\mathrm{H2}}) \tag{9}$$
$$=\sum_{j=1}^{4}\left(e^{-b_j{}^{[12]}\left(r-l_j{}^{[12]}\right)^2}\right)$$
$$\cdot\left[\kappa_j{}^{[12]}+\zeta_j{}^{[12]}\sqrt{1.1-cos(\tau)^2}+\sum_{i=1}^{2}\xi_{ij}{}^{[12]}\left(e^{-\beta_{ij}{}^{[12]}\left(\cos\,(\tau)-t_{ij}{}^{[12]}\right)^2}\right)\right]$$

6.2.6 Tertiary fit

The tertiary coordinates for this surface are: the N-H2 stretch, C-N-H1 and C-N-H2 bends, C-N stretch, three C-H stretches, three N-C-H bends, three H-C-H bends and the H2-N-C-H1 torsion. In the original APRP paper, harmonic terms parameterized with Hessians were used for tertiary contributions, which made dissociation of the tertiary bonds impossible. In this work, the tertiary contributions were derived by fitting electronic structure data points. The tertiary fit parameters were determined at different locations along the two primary coordinates called anchor points. Two-dimensional tent functions that depend on the primary coordinates were used to interpolate the tertiary contribution between the anchor points making the tertiary contribution parametrically dependent on the primary coordinates.

The equations for the tertiary coordinates are enumerated below in eq. (10)-(18). The parameters for these equations at all the anchor points are given in the Fortran subroutine available in the Truhlar group's POTLIB database. In the equations, the superscripts in square brackets, $[n, m]$, are an indexing system for the anchor points. The functional forms of the tertiary contributions are the same for U_{11} and U_{22}, but the parameters are different. The diabatic coupling contribution, U_{12} takes a different form than U_{11} and U_{22} for all tertiary coordinates.

Eq. (10) shows the functional form for the N-C-HX bends, where X can be 5-7. The subscript in front of the U indicates the surface (JJ = 11 or 22). This notation is removed from the right hand side for brevity. In this equation, $F_{N-C-H}^{[n.m]}$ is an anchor point dependent parameter; ${\theta_{N-C-H}^{0}}^{[n,m]}$ is the angle of minimum energy as a function of bending at anchor point $[n, m]$ (this is a simplification for the three bends because they have slightly different values along the anchor points). The parameters at every anchor

point can be found in the Fortran subroutine. The U_{12} contribution was set to zero because the adiabats are essentially equal to the diabats along the N-C-H bends.

$$ {}_{JJ}U_{\mathrm{N-C-HX}}^{[n,m]} = F_{N-C-H}^{[n,m]} \cdot \left(\theta_{\mathrm{N-C-HX}} - {\theta_{N-C-H}^{0}}^{[n,m]}\right)^2 \tag{10} $$

Eq. (11) shows the form for the C-HX stretches, where X can be 5-7. This equation has parameters: $F_{C-H}^{[n.m]}$ and ${a_{C-H}}^{[n,m]}$. The parameter, ${r_{C-H}^{0}}^{[n,m]}$ is the minimum energy stretch distance at anchor point $[n, m]$ (this is a slight simplification as the three stretches have slightly different values). The parameter values can be found in the Fortran subroutine. The equation is a Morse potential, which allows the bond to dissociate. The U_{12} contribution was set to zero because the adiabats are essentially equal to the diabats along the C–H stretch.

$$ {}_{JJ}U_{\mathrm{C-HX}}^{[n,m]} = F_{C-H}^{[n,m]} \cdot \left(1 - e^{-{a_{C-H}}^{[n,m]}\left(r_{C-\mathrm{HX}} - {r_{C-H}^{0}}^{[n.m]}\right)}\right)^2 \tag{11} $$

The functional form of contributions along the N-H2 stretch for U_{11} and U_{22} is shown in eq. (12). The first term is a Morse potential with parameters $F_{N-H2}^{[n,m]}$, ${a_{N-H2}}^{[n,m]}$, and ${r_{N-H2}^{0}}^{[n.m]}$ which is the minimum energy stretch at anchor point $[n, m]$. The second term is a simple quartic function of $r_{N-\mathrm{H2}}$ centered at ${r_{N-H2}^{0}}^{[n.m]}$, with leading coefficient, $G_{N-\mathrm{H2}}^{[n.m]}$. This first term prevents the N-H2 bond from dissociating, which is a major restriction made for our DPEM to be discussed in more detail in the Results and Discussion sections, but we mention here that this means the DPEM is semiglobal rather than being globally accurate for all possible geometries. The parameter values can be found in the Fortran subroutine.

$$ {}_{JJ}U_{\mathrm{N-H2}}^{[n,m]} = F_{N-\mathrm{H2}}^{[n,m]} \cdot \left(1 - e^{-{a_{N-H2}}^{[n,m]}\left(r_{N-\mathrm{H2}} - {r_{N-H2}^{0}}^{[n.m]}\right)}\right)^2 + G_{N-\mathrm{H2}}^{[n.m]} \cdot \left(r_{N-\mathrm{H2}} - {r_{N-H2}^{0}}^{[n.m]}\right)^4 \tag{12} $$

Eq. (13) is the contribution along the N-H2 stretch for U_{12}. This equation is a Gaussian with parameters, $H_{N-H2}^{[n.m]}$, ${\omega_{N-H2}}^{[n.m]}$, and ${\lambda_{N-H2}}^{[n.m]}$, and the values can be found in the Fortran subroutine.

$$ {}_{IJ}U_{\mathrm{N-H2}}^{[n,m]} = H_{N-\mathrm{H2}}^{[n.m]} \cdot e^{-\omega_{N-\mathrm{H2}}{}^{[n.m]}\left(r_{N-\mathrm{H2}}-\lambda_{N-\mathrm{H2}}{}^{[n.m]}\right)^2} \tag{13} $$

The tertiary contribution to the diabats and diabatic coupling for the C-N stretch has the same functional form as N-H2 (eq. (12) and eq. (13)). The values for these parameters at all the anchor points can be found in the Fortran subroutine.

The functional form of the C–N-HX tertiary contributions for U_{11} and U_{22} are given in equation 10. The X indicates 1 or 2; the parameters for these two bends are very similar for anchor points at small N-H1 distances, but the C-N-H1 contribution goes to zero at large N-H1 distances. The equation has parameters $F_{C-N-HX}^{[n,m]}$ and ${\theta_{C-N-HX}^{0}}^{[n.m]}$, which is the minimum energy bend at anchor point $[n,m]$ for bend, C-N-HX. The tertiary contribution to U_{12} for both bends has a Gaussian form as shown in Equation 11, with parameters, $H_{C-N-HX}^{[n.m]}$, ${\omega_{C-N-HX}}^{[n.m]}$, and ${\lambda_{C-N-HX}}^{[n.m]}$, which can be found in the Fortran subroutine.

$$ {}_{JJ}U_{\mathrm{C-N-HX}}^{[n,m]} = F_{\mathrm{C-N-HX}}^{[n,m]} \cdot \left(cos(\theta_{\mathrm{C-N-HX}}) - cos\left({\theta_{\mathrm{C-N-HX}}^{0}}^{[n.m]}\right)\right)^2 \tag{14} $$

$$ {}_{IJ}U_{\mathrm{C-N-HX}}^{[n,m]} = H_{\mathrm{C-N-HX}}^{[n.m]} \cdot e^{-\omega_{\mathrm{C-N-HX}}{}^{[n.m]}\left(cos(\theta_{\mathrm{C-N-HX}})-\lambda_{\mathrm{C-N-HX}}{}^{[n.m]}\right)^2} \tag{15} $$

In addition to the tertiary equations above derived from fitting data, we also included two tertiary functions based on chemical intuition about our system. To account for ammino group rotation relative to the methyl group, eq. (16) was included in the tertiary scheme. In this equation, the ammino and methyl hydrogens interact through a torsion term. The term becomes smaller at larger H2-H5 bond lengths due to the Gaussian term. The contribution from this equation was very small, but we saw a clear

improvement in frequency calculations with its addition. The N-H1 torsion is not included in this tertiary contribution because it caused small but unphysical adjustments to the minimum energy structures. The parameters ($H^{[n.m]}_{\mathrm{H2-N-C-H5}}$, $d_{\mathrm{H2-H5}}$, τ_T, and $\omega_{\mathrm{H2-H5}}$) for U_{11} and U_{22} are can be found in the Fortran subroutine. Only the parameter, $H^{[n.m]}_{\mathrm{H2-N-C-H5}}$, is dependent on the anchor point. No contribution was included for U_{12} for this tertiary coordinate.

$$ {}_{II}U^{[n,m]}_{\mathrm{H2-N-C-H5}} = H^{[n.m]}_{\mathrm{H2-N-C-H5}} \cdot (1 - cos3(\tau_{H2-N-C-H5} - \tau_T)) \cdot e^{\frac{(r_{\mathrm{H2-H5}} - d_{\mathrm{H2-H5}})^2}{-\omega_{\mathrm{H2-H5}}}} \quad (16) $$

The contribution from the three H-C-H bends on the methyl was included via eq. 17, which is a pairwise summation of the three interactions. In the equation, X and Y can be 5, 6, or 7, but X cannot equal Y. The contribution from these terms is small, but again we saw an improvement in our frequency calculations with its inclusion. The contributions from the HCH interactions can go to zero if a C-H bond breaks due to the Gaussian term. The parameters ($H^{[n.m]}_{\mathrm{H-C-H}}$, $\lambda_{\mathrm{H-C-H}}$, $d_{\mathrm{H-H}}$, and $\omega_{\mathrm{H-H}}$) for U_{11} and U_{22} can be found in the Fortran subroutine. Only the parameter, $H^{[n.m]}_{\mathrm{H-C-H}}$, is dependent on the anchor point. No contribution was included for U_{12} for this tertiary coordinate.

$$ {}_{II}U^{[n,m]}_{\mathrm{H-C-H}} = \sum_{X<Y} H^{[n.m]}_{\mathrm{H-C-H}} \cdot (\theta_{\mathrm{HX-C-HY}} - \lambda_{\mathrm{H-C-H}})^2 \cdot e^{\frac{(r_{\mathrm{HX-HY}} - d_{\mathrm{H-H}})^2}{-\omega_{\mathrm{H-H}}}} \quad (17) $$

As shown in eq. (18), the tertiary potential at an anchor point is the sum of all the tertiary contributions at that anchor point and a constant, ${}_{IJ}const^{[n,m]}$. The constants can be found in the Fortran subroutine. They were calculated by solving for the tertiary contribution at each anchor point with the tertiary coordinates at the ground state minimum values. The constant adjust the zero of energy for the tertiary contribution at

each anchor point. When the tertiary coordinates are at the ground state optimized values (as they were for data collection and fitting along the primary coordinates), the total energy will equal the energy of the primary coordinate fit. The tertiary coordinates could lower or raise the energy from the primacy contribution depending on how that tertiary coordinate changes relative to its minimum energy structure at every anchor point.

$$ {}_{IJ}U^{[n.m]}(\boldsymbol{R}) = \sum_{stretches} {}_{IJ}U^{[n,m]}_{stretch} + \sum_{bends} {}_{IJ}U^{[n,m]}_{bend} + {}_{IJ}const^{[n,m]} \tag{18} $$

${}_{IJ}U^{[n,m]}(\boldsymbol{R})$ is the tertiary energy contribution at anchor point $[n, m]$ for diabatic state, *IJ* where *I* can equal *J*. The **R** stands for all the tertiary coordinates. The tertiary contribution along the two primary coordinates (${}_{IJ}U_{Tertiary}$) is calculated with the contribution from the different anchor points and tent functions as shown in eq. (19). In this equation, $T^{[n,m]}(r_{N-H1}, \tau_{H1-N-C-H2})$ is the tent function, and N_n and N_m are the total number of anchor points along the N–H1 bond distance and H1-N-C-H2 improper torsion angle, respectively.

$$ {}_{IJ}U_{Tertiary} = \sum_{n=1}^{N_n} \sum_{m=1}^{N_m} {}_{IJ}U^{[n,m]}(\boldsymbol{R}) \cdot T^{[n,m]}(r_{N-\mathrm{H1}}, \tau_{\mathrm{H1-N-C-H2}}) \tag{19} $$

Previous work with APRP has involved one-dimensional tent functions.[4, 201-203] For this system, we've generalized that approach to two dimensions. As can be seen in the equations above, the tertiary contributions and tent functions have a two index naming convention; the first term in brackets, n corresponds to the index along r_{N-H1} and the second term, m is the index along $cos(\tau_{H1-N-C-H2})$. These anchor points are located along four N–H1 bond distances and three H1-N-C-H2 improper torsions resulting in twelve total anchor points. The distances along N–H1 are approximately 0.7, 1.0, 2.2, and 3.5 Å and the improper torsion angles were approximately 0° (which corresponds to planar CNH_2), 61° (the optimized improper torsion), and 100° (a higher-energy structure with H1 and H2 closer to each other).

A schematic of the anchor points is shown in Figure 6.2. The cosine of the improper torsion angle was used, so the left most anchor points are located at cos(100°) and the right most points are at cos(0°). All three anchor points with N–H1 at 3.5 Å along the torsion coordinate had equivalent parameters and therefore equivalent tertiary contributions, or restated, ${}_{IJ}U^{[4.m]}(\boldsymbol{R})$ was the same for all m. At this distance along the N–H1 bond length, the improper torsion has negligible effect because the two hydrogens stop interacting. In Figure 6.2, these anchor points at N–H1 = 3.5 Å are shown along a red doted line.

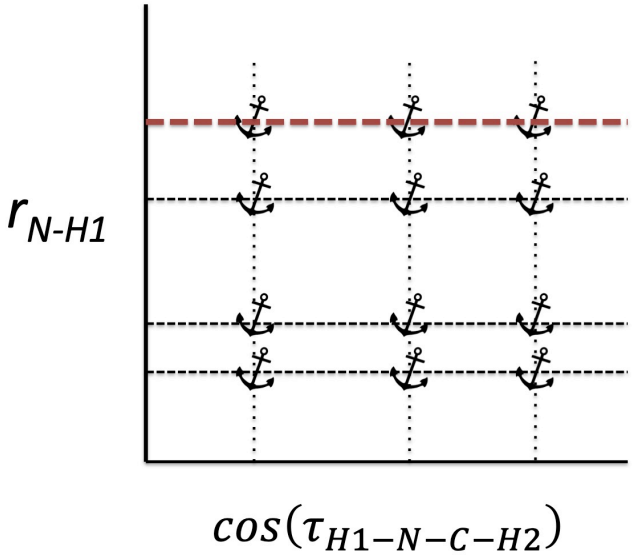

Figure 6.2. Schematic of anchor point locations along the primary coordinates

An example is shown below of the four nonzero tent functions, *T*, at the [1,1] anchor point, which depends on the values of the two primary coordinates (shortened to r and τ). The tent function for a general anchor point, (p, q) is given in Equation 21. When the coordinates do no fall between a tent function's anchor points, that tent function is zero. For example, when the primary coordinates are smaller than $r^{[1]}$ and $cos(\tau)^{[1]}$

(Equation 20(A)), all the tent terms except for $T^{[1,1]}$ are equal to zero ($T^{[1,2]}$, $T^{[1,3]}$, $T^{[2,2]}$, … ,$T^{[3,3]}$=0).

$$T^{[1,1]} = 1 \qquad \begin{cases} r < r^{[1]} \\ cos(\tau) < cos(\tau)^{[1]} \end{cases} \tag{20A}$$

$$T^{[1,1]} = \frac{\left(r - r^{[2]}\right)^4 \left(cos(\tau) - cos(\tau)^{[1]}\right)^4}{\sum_{\chi=1}^{2} (r - r^{[\chi]})^4 (cos(\tau) - cos(\tau)^{[1]})^4} \quad \begin{cases} r^{[1]} \le r < r^{[2]} \\ cos(\tau) < cos(\tau)^{[1]} \end{cases} \tag{20B}$$

$$T^{[1,1]} = \frac{\left(r - r^{[1]}\right)^4 \left(cos(\tau) - cos(\tau)^{[2]}\right)^4}{\sum_{\eta=1}^{2} (r - r^{[1]})^4 (cos(\tau) - cos(\tau)^{[\eta]})^4} \quad \begin{cases} r < r^{[1]} \\ cos(\tau)^{[1]} \le cos(\tau) < cos(\tau)^{[2]} \end{cases} \tag{20C}$$

$$T^{[1,1]} = \frac{\left(r - r^{[2]}\right)^4 \left(cos(\tau) - cos(\tau)^{[2]}\right)^4}{\sum_{\chi=1}^{2} \sum_{\eta=1}^{2} (r - r^{[\chi]})^4 (cos(\tau) - cos(\tau)^{[\eta]})^4} \quad \begin{cases} r^{[1]} \le r < r \\ cos(\tau)^{[1]} \le cos(\tau) < cos(\tau)^{[2]} \end{cases} \tag{20D}$$

$$T^{[p,q]} = \frac{\left(r - r^{[p-1]}\right)^4 \left(cos(\tau) - cos(\tau)^{[q-1]}\right)^4}{\sum_{\chi=p-1}^{p} \sum_{\eta=q-1}^{q} (r - r^{[\chi]})^4 (cos(\tau) - cos(\tau)^{[\eta]})^4} \quad \begin{cases} r^{[p-1]} \le r < r^{[p]} \\ cos(\tau)^{[q-1]} \le cos(\tau) < cos(\tau)^{[q]} \end{cases} \tag{21A}$$

$$T^{[p,q]} = \frac{\left(r - r^{[p+1]}\right)^4 \left(cos(\tau) - cos(\tau)^{[q-1]}\right)^4}{\sum_{\chi=p}^{p+1} \sum_{\eta=q-1}^{q} (r - r^{[\chi]})^4 (cos(\tau) - cos(\tau)^{[\eta]})^4} \quad \begin{cases} r^{[p]} \le r < r^{[p+1]} \\ cos(\tau)^{[q-1]} \le cos(\tau) < cos(\tau)^{[q]} \end{cases} \tag{21B}$$

$$T^{[p,q]} = \frac{\left(r - r^{[p-1]}\right)^4 \left(cos(\tau) - cos(\tau)^{[q+1]}\right)^4}{\sum_{\chi=p-1}^{p} \sum_{\eta=q}^{q+1} (r - r^{[\chi]})^4 (cos(\tau) - cos(\tau)^{[\eta]})^4} \quad \begin{cases} r^{[p-1]} \le r < r^{[p]} \\ cos(\tau)^{[q]} \le cos(\tau) < cos(\tau)^{[q+1]} \end{cases} \tag{21C}$$

$$T^{[p,q]} = \frac{\left(r - r^{[p+1]}\right)^4 \left(cos(\tau) - cos(\tau)^{[q+1]}\right)^4}{\sum_{\chi=p}^{p+1} \sum_{\eta=q}^{q+1} (r - r^{[\chi]})^4 (cos(\tau) - cos(\tau)^{[\eta]})^4} \quad \begin{cases} r^{[p]} \le r < r^{[p+1]} \\ cos(\tau)^{[q]} \le cos(\tau) < cos(\tau)^{[q+1]} \end{cases} \tag{21D}$$

6.3. Results

6.3.1. Diabatization

The XMS(2)-CASPT2 and DQ diabatization results are shown in Figure 6.3 for three different slices along the potential energy surfaces. The three slices are the: (a) N-H1 stretch, (b) C-H7 stretch, and (c) C-N stretch. All other internal coordinates are at the ground state minimum geometries. For all three slices, the adiabatic energies are widely separated, as expected.[184] For the N-H and C-N stretches, the diabats calculated with the DQ diabatization method show a diabatic crossings, while along the C-H stretch, there

isn't a crossing and the diabats are approximately equal to the adiabats. This is in agreement with previous findings that the N-H and C-N dissociation channels involve a change in character of the S_0 and S_1 states, while C-H does not.[183-184] This change in character comes from the rearrangement of the p-orbital energetics along the N-H and C-N dissociation pathways. The character of the ground state at the optimized structure matches with the character of the excited state at dissociation while the character of the excited state at the optimized structure matches with the character of the ground state at dissociation.

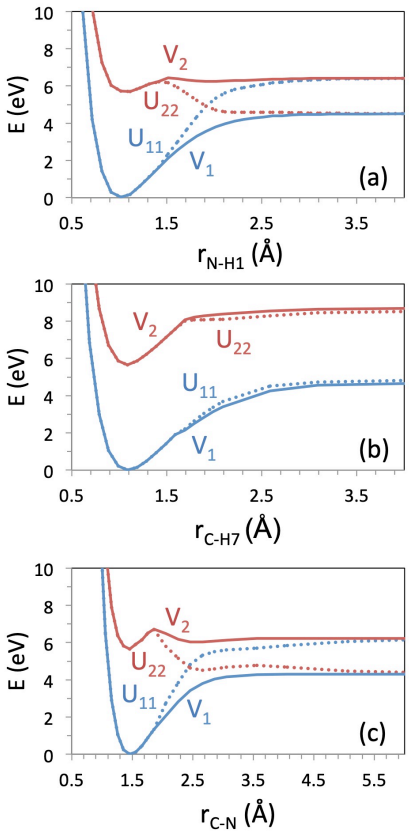

Figure 6.3. Adiabats and DQ derived diabats along three bond dissociation slices, (a) N-H1, (b) C-H7, and (c) C-N. The DQ method made use of coordinate dependent weights on the quandrupole contribution.

In previous work where we studied small test systems using the DQ method, we predominately used constant weights on the quadrupole terms.[3, 104] For this system, we

were not able to find constant weights that worked along different slices and therefore switched tactics to coordinate dependent weights described in the Methods and Computational Details section. The results of the DQ diabatization method with coordinate dependent weights are very encouraging. This application to methylamine supports previous findings that the DQ diabatization method can generally produce reasonable diabats and further showcases this method applied for generating DPEMs on systems with more degrees of freedom than those previously studied. This work also demonstrates the usefulness of coordinate dependent weights on the quadrupole contribution for a polyatomic system.

6.3.2. Excitation energies

Table 6.3 compares the vertical excitation energies of our APRP fit surface with XMS-CASPT2 results and previous work. The vertical excitation is the difference of the ground and first excited states energies at the ground state minimum geometry. Our APRP fit shows good agreement with our XMS-CASPT2 calculations indicating a good fit in this region. Our vertical excitation energies are slightly higher than those calculated by Morokuma[185] and more recently by Yarkony[196] with his PESs for methylamine.

Table 6.3. Vertical excitation energies on the adiabatic PESs

Method	S_0-S_1 (eV)	Ref.
APRP	5.70	This work
XMS-CASPT2(6,6)	5.65	This work
XMS-CASPT2(8,8)	5.57	[185]
E(H^d)	5.41	[196]

In Table 6.4, we compare our bond dissociation energy with experiment by taking into account zero point energy and temperature. Our APRP results are considerably lower than the experimental value derived with the Active Thermochemical Tables from Argonne National Labs.[208-213] Comparing our APRP fit to the XMS-CASPT2(6,6) data

that was used in the fitting procedure, we see good agreement (the BDEs differ by only 0.03eV without ZPE or temperature considerations). This indicates that the discrepancy with experiment comes from the electronic structure calculation.

Table 6.4. Bond dissociation energy of the ground state of methylamine at 298 K including the change in zero point energy

Method	ΔH_{298} (eV)	Ref.
APRP	4.12	This work
Expt.	4.58	[213]

In Table 6.5 we compare our APRP BDE results with zero point energy included to other methods. The surface derived in ref[196] is slightly higher, but all three methods show lower BDEs than expected. Concerning our fit, this noted difference from experiment should be taken into consideration for dynamics studies.

Table 6.5. Bond dissociation energy of the ground state of methylamine including zero point energy

Method	ΔH_0 (eV)	Ref.
APRP	4.06	This work
(EOM-)CCSD	4.00	[197]
$E(H^d)$	4.17	[196]

In Table 6.6, we compare the classical adiabatic and 0-0 excitation energies from the APRP surface, electronic structure calculations, and experiment. The classical adiabatic energy is the difference in energy of the ground state minimum and excited state minimum. The 0-0 excitation is the same as the classical adiabatic, but with zero point energy included. For the APRP surface, this involved adding back the zero-point vibrational energy of V_1 and V_2 calculated at their equilibrium geometries using the harmonic approximation. For the classical adiabatic energy, the APRP results agree well with the XMS-CASPT2(8,8) calculations, but are smaller than those in ref[196]. For the 0-0

excitation, the experimental value has been debated,[191] which is why two values are given in Table 6.6. The APRP surface is in better agreement with the lower 0-0 excitation.

Table 6.6. Adiabatic and 0-0 excitation energies for the ground to first excited state of methylamine

Method	Classical Adiabatic (eV)	0-0 (eV)	Ref.
APRP	5.08	4.89	This work
XMS-CASPT2(8,8)	5.03	…	185
E(H^d)	5.41	5.26	196
Expt.	…	5.17/4.93	190, 198

6.3.3. Equilibrium geometry and frequencies

The equilibrium geometric parameters of the S_0 state calculated with our APRP surface and with density functional theory (DFT) are shown in Table 6.7. The DFT calculations were performed with the M06-2X functional[214] and the 6-31++G** basis set.[102, 204-207] Comparing the two methods, all geometric parameters are in good agreement. For the DFT optimized parameters, the C-H5 bond length and N-C-H5 bend is slightly larger than the other C-H lengths and N-C-H angles. The three C-H bond lengths and three N-C-H bond angles from APRP are equivalent, which is expected based on the functional form of the APRP DPEM. As stated in the Methods and Computational Details section, this was a simplification we employed. We do not anticipate that this approximation will have a significant effect on future studies involving the surfaces.

Table 6.7. Geometric parameters of the S_0 equilibrium geometry of methylamine calculated with the APRP surfaces and DFT

	APRP	M06-2X
Bond lengths (Å)		
N-H1	1.02	1.01
N-H2	1.02	1.01
C-N	1.46	1.46
C-H5	1.09	1.10
C-H6	1.09	1.09
C-H7	1.09	1.09
Bond angles (deg)		
C-N-H1	111	111
C-N-H2	111	111
N-C-H5	110	115
N-C-H6	110	109
N-C-H7	110	109
Improper torsion (deg)		
H1-N-C-H2	63	61

The optimized structure of the methylamine excited state has, for a long time, been assigned as having a pyramidalization change from the optimized ground state.[183] This means the amino group moves towards a more planar structure. We calculated the optimized excited state using our APRP surface and time-dependent density functional theory (TDDFT). The geometric parameters are shown in Table 6.8. The TDDFT calculations were preformed with the τHCTHhyb functional[215] and the 6-31++G** basis set.[102, 204-207] Before comparing the parameters, we note an interesting, but energetically irrelevant difference in structure between the two calculations. The APRP excited structure has a "ciscoid" geometry, as defined by Morokuma,[185] where H5 is approximately in a plane with C, N, H1, and H2. This geometry was also found when optimizing the excited state using XMS-CASPT2(6,6). The TDDFT results are more similar to what Morokuma describes as a "planar" geometry, where no methyl hydrogens are in the amino plane. Morokuma found that the ciscoid structure was 0.2 kj/mol (~0.002 eV) higher in energy than the planar geometry.[185] As this energy difference between the structures is very small, we believe this discrepancy is not problematic.

Comparing the geometric parameters in the table, the APRP results and TDDFT are mostly very similar, except for the H1-N-C-H2 improper torsion; for TDDFT this parameter is 10° and for APRP it is 1°. These measurements translate to the amino wag coordinate being slightly out of the plane for TDDFT vs. the CNH_2 essentially in a plane for the APRP. Once again, the APRP results are in agreement with the XMS-CASPT2(6,6) data that was used for the fit, which had an improper torsion value of ~1°. This means that the difference in this parameter was a difference in TDDFT calculations and XMS-CASPT(6,6) calculations of the S_1 minimum. Morokuma found the S_1 optimized state to have an improper torsion of 6°,[185] which falls between our results from the two electronic structure optimizations.

A small discrepancy is noted for the C-H bond lengths and N-C-H angles; similar to the ground state, these parameters differ slightly for TDDFT while the APRP surface treats these bond lengths and angles as being equivalent.

Table 6.8. Geometric parameters of the S_1 equilibrium geometry of methylamine calculated with the APRP surfaces and TD-DFT

	APRP	τHCTHhyb
Bond lengths (Å)		
N-H1	1.06	1.03
N-H2	1.06	1.03
C-N	1.43	1.42
C-H5	1.09	1.11
C-H6	1.09	1.10
C-H7	1.09	1.10
Bond angles (deg)		
C-N-H1	120	121
C-N-H2	122	121
N-C-H5	108	106
N-C-H6	108	110
N-C-H7	108	110
Improper torsion (deg)		
H1-N-C-H2	1	10

Figure 6.4 compares the vibrational frequencies of the APRP adiabatic PESs and DFT methods for S_0 (Fig. 6.9(a)) and S_1 (Fig. 6.9(b)). The data shows good qualitative

agreement. For the S_0 frequency data, the mean unsigned percentage difference between the two methods is 8%. Removing the frequencies lower than 1000 cm^{-1}, the unsigned percentage difference improves to 5%. For the S_1 data, the mean unsigned percentage difference is 16% and removal of frequencies lower than 1000 cm^{-1} gives an improved mean unsigned percentage difference of 6%. These results are encouraging for our modified APRP approach. Previous APRP studies relied on Hessian data from DFT calculations and showed good agreement between DFT derived frequencies and the APRP surfaces. Here we did not use DFT data, but still have fairly good agreement with DFT frequencies and DFT calculated geometric parameters.

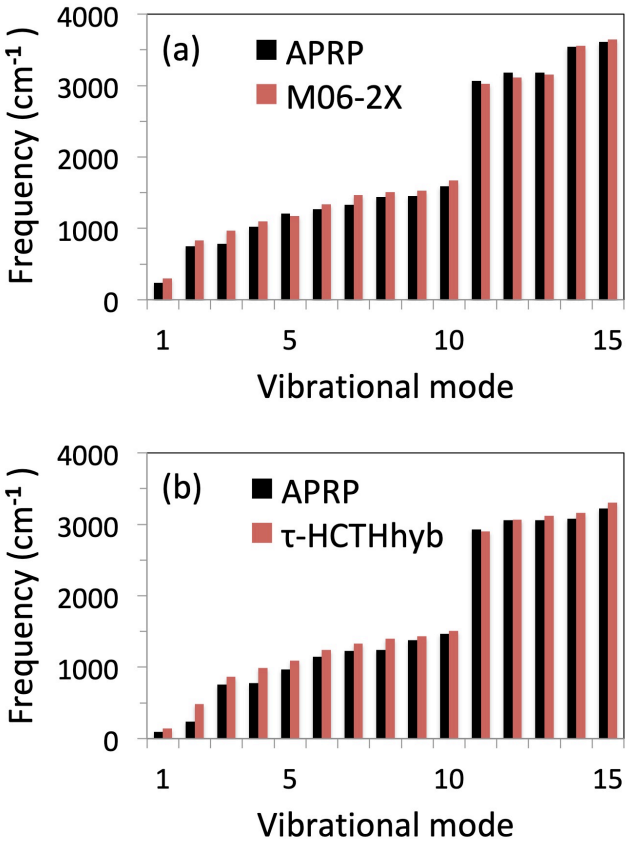

Figure 6.4. Frequencies of the S_0 and S_1 equilibrium geometry of methylamine computed with APRP and with DFT for the ground state and TD-DFT for the excited state

The optimized geometric parameters and frequencies of the N-H dissociated species also show good agreement with DFT calculations; these results will be given in the Supplementary Material (Section S2) of the published work.

6.3.4. Barrier on the excited surface and minimum energy conical intersection

The existence of a barrier, or saddle point, on S1 along the N-H stretch has been well documented in previous work.[183-187] We optimized this structure with our APRP surface and compare it to other methods in Table 6.9. The height of our barrier is smaller than previous XMS-CASPT2(8,8) results[185] and larger than the fitted surface recently developed in ref[196], but it's in good agreement with the (EOM-)CCSD calculations from ref[197]. All the methods show similar N-H bond distances, although again we have the best agreement with ref[197]. The reported H1-N-C-H2 improper torsions are all in good agreement; the amino group was found to have a flat structure at the saddle point. All four methods have a ciscoid structure, i.e. H5 is in the same plane as the flat amino group. For all four methods, H5 is cis relative to the H1 around the C-N bond stretch.

Table 6.9. Energy difference from the optimized excited state to the saddle point and geometric parameters of the saddle point calculated for the adiabatic PES by various methods

Method	Δ (eV)	$r_{N\text{-}H1}$ (Å)	$\tau_{H1\text{-}N\text{-}C\text{-}H2}$ (deg)	Ref.
APRP	0.37	1.39	0	This work
XMS-CASPT2(8,8)	0.76	1.34	0	[185]
(EOM-)CCSD	0.42	1.37	0	[197]
$E(H^d)$	0.28	1.31	…	[196]

The minimum energy conical intersection (MECI) is another important structure to consider. We found the MECI geometry for our APRP surfaces using BFGS, as described in previous work.[201-203] These results, along with the MECI results from other methods, are reported in Table 6.10. Our MECI is a little lower in energy compared to the other methods and our N-H bond length is shifted to slightly smaller distances. The

reported H1-N-C-H2 improper torsions show good agreement; the amino structure was approximately planar. The C-N-H1 bond angles are similar between the three method; these values are all close to 120°. For all three methods, the MECI geometries appear to be ciscoid, with H5 in plane with the amino group and cis to H1.

Table 6.10. Minimum energy conical intersection (MECI) energies and geometric parameters from different methods

Method	MECI (eV)	$r_{N\text{-}H1}$ (Å)	$\tau_{H1\text{-}N\text{-}C\text{-}H2}$ (deg)	$\Theta_{C\text{-}N\text{-}H1}$ (deg)	Ref.
APRP	4.81	1.88	3	120	This
XMS-CASPT2(8,8)	5.04	1.93	0	124	[185]
$E(H^d)$	4.99	1.95	…	122	[196]

Levi et. al.[199-200] came across a CI seam for methylamine by exploring the surface around a structure with N-H1 at 1.83 Å, N-H2 at 1 Å, and both C-N-HX angles around 120°. The structure was ciscoid with the amino flat. By keeping all atoms positions fixed except for H1, they found a seam along the C-N-H1 angle. We have found a similar CI seam in our APRP surfaces. The energies and geometric parameters of our seam are given in Table 6.11 along with XMS-CASPT2(6,6) calculations at the same structures.

As shown in Table 6.11, we calculated the MECI at fixed C-N-H1 angles. Along this range, the structure was consistently ciscoid with the amino group in a plane with H5. Most bond distances and angles were almost identical for all points on the seam, the one exception being the C-N-H2 angle. For the first two entires, (C-N-H1 = 90° and 100°), the C-N-H2 angle is close to 120°. At C-N-H1 = 120° and larger bends, the C-N-H2 angle is consistently close to 110°. The XMS-CASPT results have a higher S_1 value, but the two states are close in energy for the entire range.

Table 6.11. Adiabatic PESs and geometric parameters of the S_0/S_1 conical intersection calculated with the APRP surface along a path with selected $\Theta_{C\text{-}N\text{-}H1}$ and CASPT2 results at the same coordinates.

	APRP		XMS-CASPT2					
$\Theta_{C\text{-}N\text{-}H1}$ (deg)	V_1 (eV)	V_2 (eV)	V_1 (eV)	V_2 (eV)	$r_{N\text{-}H1}$ (Å)	$r_{N\text{-}H2}$ (Å)	$\Theta_{C\text{-}N\text{-}H2}$ (deg)	$\tau_{H1\text{-}N\text{-}C\text{-}H2}$ (deg)
90	5.19	5.22	5.28	5.42	1.88	0.99	124	0
100	5.09	5.10	5.12	5.30	1.88	1.00	121	0
110	4.82	4.82	4.85	4.94	1.88	1.01	111	1
120	4.81	4.81	4.75	4.95	1.88	1.01	110	3
130	4.82	4.82	4.72	4.95	1.88	1.01	110	3
140	4.85	4.85	4.75	4.96	1.88	1.01	111	4

6.3.5. Selected cuts and subsurfaces of the adiabatic and diabatic potentials and diabatic couplings

In this section, we show various slices of our APRP surfaces and compare the results to XMS-CASPT2(6,6) calculations at the same geometries. We discuss both diabatic PESs (the diagonal elements of the DPEM, also called diabats) and adiabatic PESs (the eigenvalues of the DPEM, also called adiabats).

Figure 6.5 shows adiabatic slices along the primary coordinates. Figure 6.5(a) has the H1-N-C-H2 improper torsion set to 101°, (b) has it at 61°, and (c) 0°. These are the three improper torsion parameters for our anchor points. The N-H bond distance ranges from ~0.6 Å to 3.5 Å. The APRP results show a little bumpiness, but otherwise are in good agreement with the XMS-CASPT2(6,6) results.

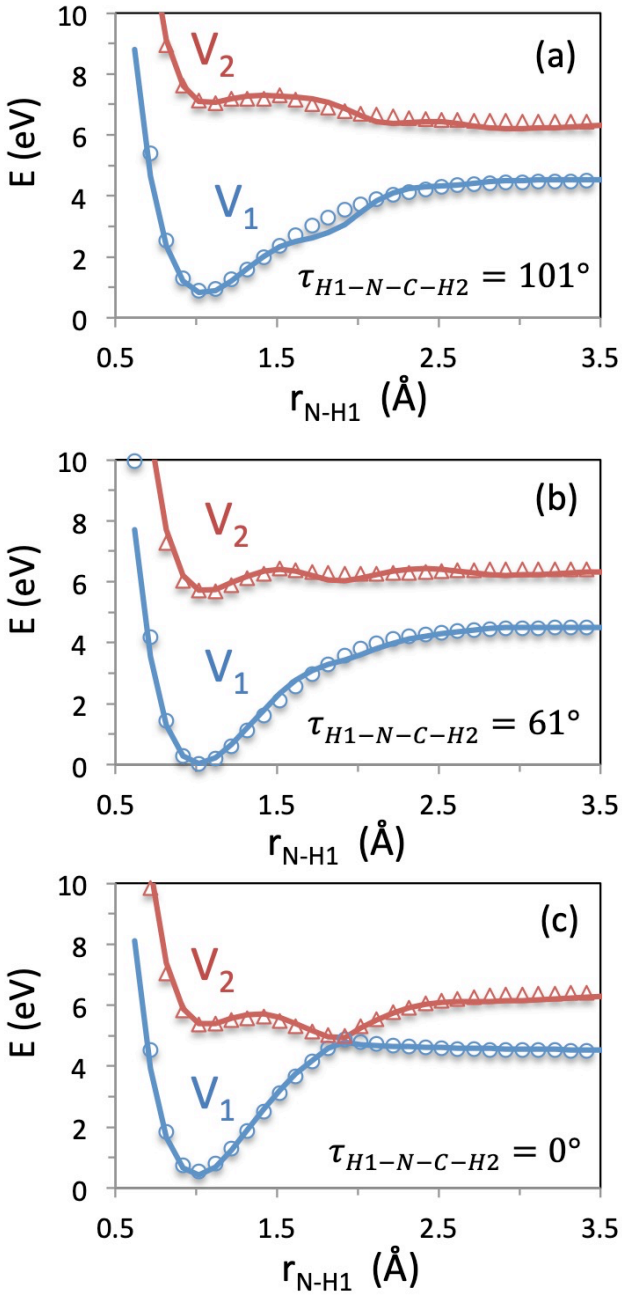

Figure 6.5. Adiabatic PESs along the N-H1 dissociation with the H1-N-C-H2 improper torsion at (a) 101°, (b) 61°, and (c) 0° calculated with APRP and CASPT2.

Figure 6.6 shows the diabats and diabatic coupling for the same coordinates as Fig. 6.5. The APRP diabatic coupling shows small differences compared to the data but overall the APRP surfaces agree well with the XMS-CASPT(6,6) results.

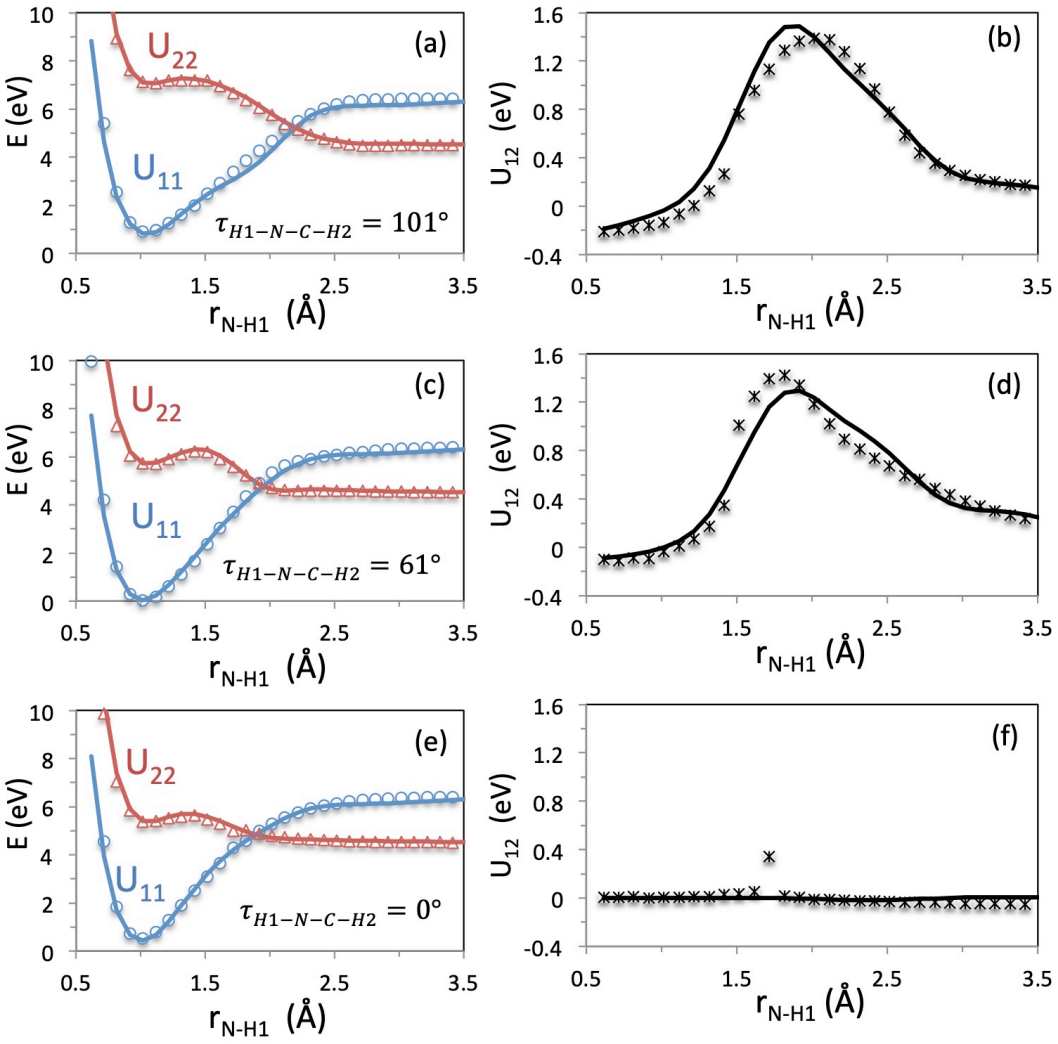

Figure 6.6. Diabatic energies (a,c,e) and diabatic couplings (b,d,f) along the N-H1 dissociation with the H1-N-C-H2 improper torsion at 101°, 61°, are 0° respectively calculated with APRP and CASPT2

Figure 6.7 shows APRP and XMS-CASPT(6,6) derived adiabats along with N-H1 stretch with the C-N-H2 angle at two different values, (a) 130°, and (b) 80°. The C-N-H2 coordinate is a tertiary coordinate in our APRP fit, so these slices demonstrate the tertiary contribution to the APRP fit. There is some bumpiness in our fit around N-H1 = 2.5 Å, but overall the fit shows good agreement with the XMS-CASPT(6,6) data. For both methods, the ground and excited surfaces are well separated at 80° and closer in energy at 130°. This difference in energy separation between the states is likely due to there being

less distinction between p-orbitals on the N as the bend gets larger. The good agreement between APRP and XMS-CASPT(6,6) for this data not included in our fitting procedure is encouraging.

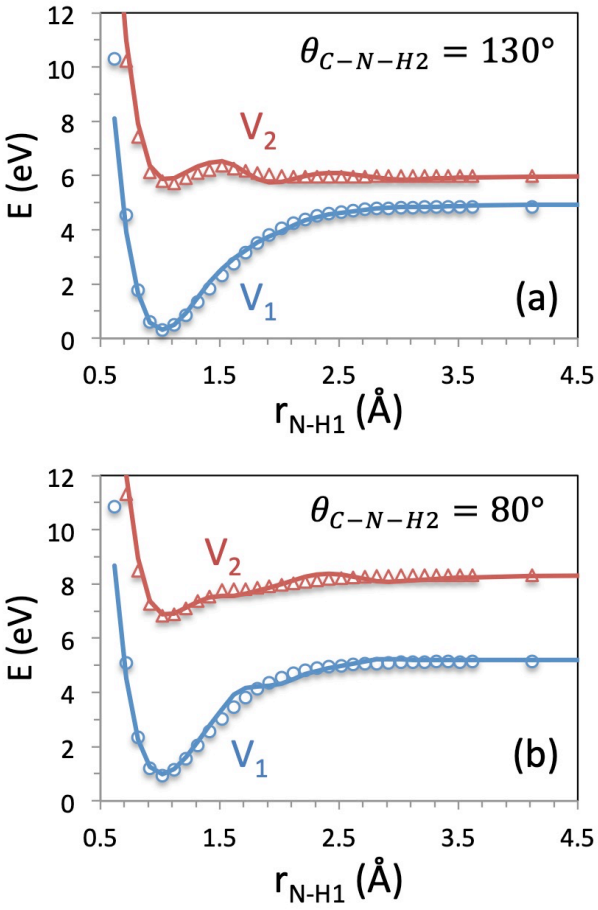

Figure 6.7. Adiabatic PESs along the N-H1 dissociation with C-H-H2 at (a) 130° (b) 80° calculated with APRP and CASPT2

We considered slices along two tertiary coordinates, C-N and C-H7 in Fig. 6.8. The results illustrate an important limitation of our surfaces, namely that they cannot dissociate along all bond distances. While the C-H7 bond is energetically allowed to dissociate, the C-N bond distance is not due to its functional form. As shown in Fig. 8(a), the energy contribution from the C-N stretch grows rapidly around 2 Å. The N-H2 bond

dissociation (not shown in the figure) is also not allowed along our surfaces, and this is an important limitation to keep in mind for future use of these DPEMs. As our surfaces are designed to model N-H1 pathways, we believe this is an acceptable approximation.

In addition to showing this limitation, Fig 6.8 also shows how our surface extrapolates between anchor points. For the calculations in the figure, the H1-N-C-H2 improper torsion was set to 30° (approximately halfway between the anchor point values of 0° and ~ 60°) and the N-H1 bond distance was set to 1.6 Å (approximately halfway between the anchor point values of ~1.0 Å and 2.2 Å). The tertiary contribution at these structures will depend on the parameters at anchor points: [2,2], [2,3], [3,2], and [3,3], but it is as far away as possible from these anchor point inside their mini grid.

For both C-N and C-H7 plots, the APRP V_1 results are a little higher in energy compared to XMS-CASPT(6,6), and the APRP V_2 results are slightly lower. Overall, the APRP results are close to those from XMS-CASPT(6,6) for these structures outside the fitting procedure.

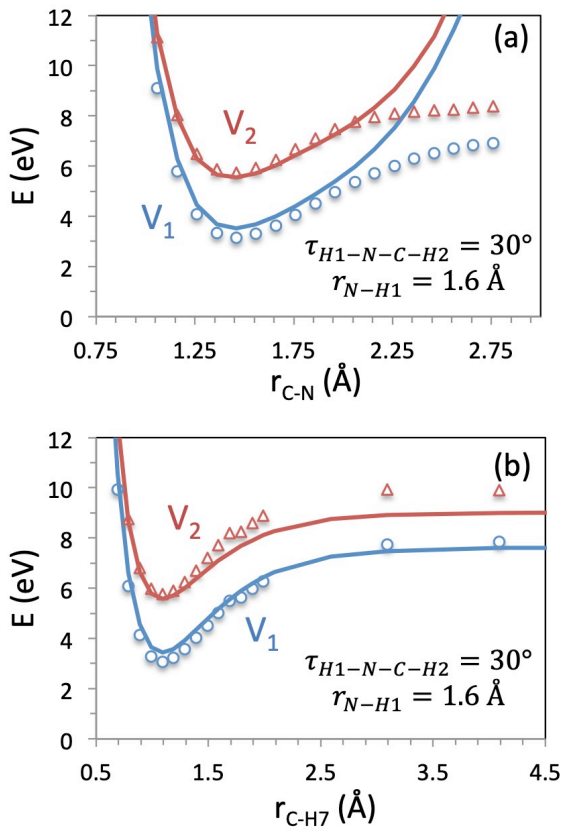

Figure 6.8. Adiabatic PESs along the (a) C-N stretch and (b) C-H7 stretch with the primary coordinates parameters: N-H1 = 1.6 Å and H1-N-C-H2 = 30° calculated with APRP and CASPT2

Figure 6.9 shows three-dimensional plots of our APRP surfaces along the primary coordinates. Figure 6.9(a) shows the diabats and 6.9(b) shows the adiabats. Trajectories can be run in either representation

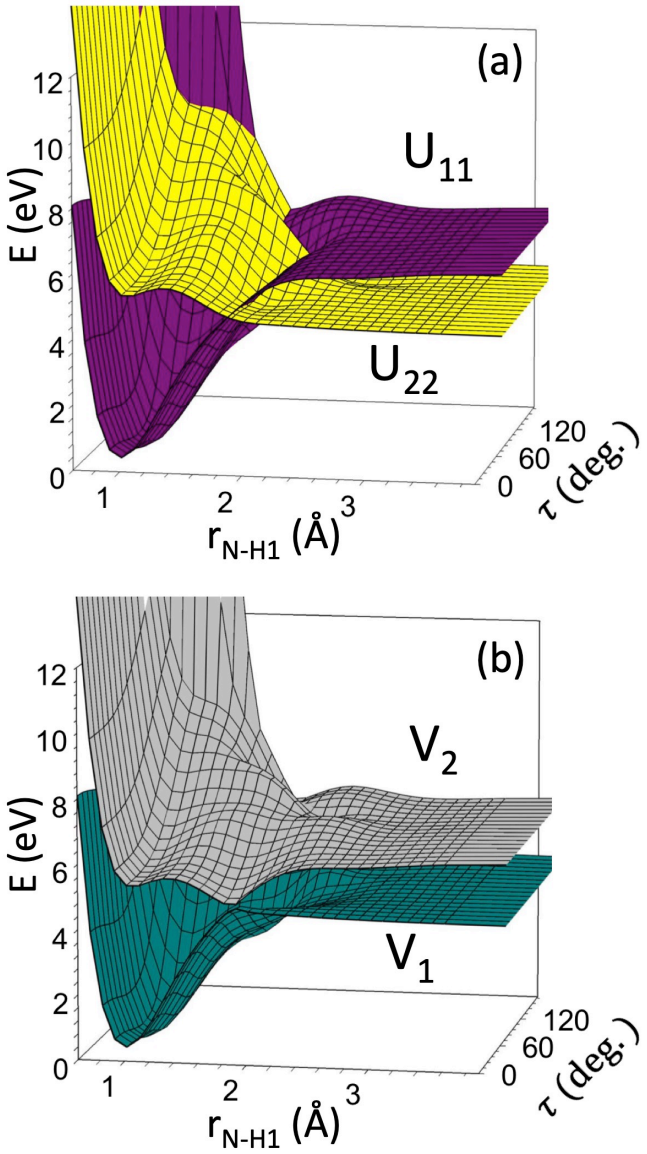

Figure 6.9. 3D plots of the APRP PESs along the primary coordinates in the (a) diabatic, and (b) adiabatic representation.

6.4 Conclusions

In this paper, we described our construction of analytical PESs in the diabatic representation for the photodissociaiton of methylamine. Towards this end, we used two methods developed by the Truhlar group, DQ diabatization and APRP, and we expanded on these methods in the process. For the DQ diabatization method, we incorporated a coordinated dependent weighting scheme on the contribution of the quadrupole; we

showed that using this approach, we could get reasonable diabats along multiple dissociation pathways. For the APRP method, we fit data along tertiary coordinates to different functional forms. We also used a two-dimensional tent function to interpolate between the anchor points. The PESs can be used in dynamics studies of the N-H1 dissociation.

Bibliography

1. Levine, B. G.; Ko, C.; Quenneville, J.; Martínez, T. J. Conical intersections and double excitations in time-dependent density functional theory. *Molecular Physics* **2006,** *104* (5-7), 1039-1051.
2. Jasper, A. W.; Kendrick, B. K.; Mead, C. A.; Truhlar, D. G. Non-Born-Oppenheimer Chemistry: Potential Surfaces, Couplings, and Dynamics. In *Modern Trends in Chemical Reaction Dynamics: Experiment and Theory (Part 1)*, Yang, X.; Liu, K., Eds. World Scientific: Singapore, 2004; pp 329-391.
3. Hoyer, C. E.; Xu, X.; Ma, D.; Gagliardi, L.; Truhlar, D. G. Diabatization based on the dipole and quadrupole: The DQ method. *The Journal of chemical physics* **2014,** *141* (11), 114104.
4. Yang, K. R.; Xu, X.; Truhlar, D. G. Anchor Points Reactive Potential for Bond-Breaking Reactions. *Journal of chemical theory and computation* **2014,** *10* (3), 924-933.
5. Gross, E. K. U.; Gross, E. K. U.; Kohn, W.; Kohn, W. Time-Dependent Density-Functional Theory. *Advances in Quantum Chemistry* **1990,** *21* (C), 255-291.
6. Casida, M. E. Time-dependent density functional response theory for molecules. In *Recent Advances In Density Functional Methods: (Part I)*, World Scientific: 1995; pp 155-192.
7. Appel, H.; Gross, E. K. U.; Burke, K. Excitations in time-dependent density-functional theory. *Physical Review Letters* **2003,** *90* (4), 430051-430054.
8. Maitra, N. T. Perspective: Fundamental aspects of time-dependent density functional theory. *Journal of Chemical Physics* **2016,** *144* (22).
9. Yu, H. S.; Li, S. L.; Truhlar, D. G.; Energy Frontier Research Centers . Energy Frontier Research Center for Inorganometallic Catalyst, D. Perspective: Kohn-Sham density functional theory descending a staircase. *The Journal of Chemical Physics* **2016,** *145* (13), 130901.
10. Roos, B. O. The complete active space SCF method in a fock‐matrix‐based super‐CI formulation. *International Journal of Quantum Chemistry* **1980,** *18* (S14), 175-189.
11. Roos, B. O.; Taylor, P. R.; Sigbahn, P. E. A complete active space SCF method (CASSCF) using a density matrix formulated super-CI approach. *Chemical Physics* **1980,** *48* (2), 157-173.
12. Werner, H. J.; Meyer, W. A quadratically convergent MCSCF method for the simultaneous optimization of several states. *The Journal of Chemical Physics* **1981,** *74* (10), 5794-5801.
13. Werner, H. J.; Knowles, P. J. A second order multiconfiguration SCF procedure with optimum convergence. *The Journal of chemical physics* **1985,** *82* (11), 5053-5063.

14. Knowles, P. J.; Werner, H.-J. An efficient second-order MC SCF method for long configuration expansions. *Chemical Physics Letters* **1985,** *115* (3), 259-267.
15. Andersson, K.; Malmqvist, P. A.; Roos, B. O.; Sadlej, A. J.; Wolinski, K. Second-order perturbation theory with a CASSCF reference function. *Journal of Physical Chemistry* **1990,** *94* (14), 5483-5488.
16. Mead, C. A.; Truhlar, D. G. Conditions for the definition of a strictly diabatic electronic basis for molecular systems. *The Journal of Chemical Physics* **1982,** *77* (12), 6090-6098.
17. Teller, E. The Crossing of Potential Surfaces. *The Journal of Physical Chemistry* **1937,** *41* (1), 109-116.
18. Klessinger, M.; Michl, J. *Excited states and photochemistry of organic molecules*. VCH: New York, 1995; p xxiv, 537 pages.
19. Robb, M. A.; Bernardi, F.; Olivucci, M. Conical intersections as a mechanistic feature of organic photochemistry. *Pure and Applied Chemistry* **1995,** *67* (5), 783-789.
20. Yarkony, D. R. Diabolical conical intersections. *Reviews of Modern Physics* **1996,** *68* (4), 985-1013.
21. Yarkony, D. R. Conical Intersections: Diabolical and Often Misunderstood. *Accounts of Chemical Research* **1998,** *31* (8), 511-518.
22. Domcke, W.; Yarkony, D. R.; Köppel, H. *Conical intersections: electronic structure, dynamics & spectroscopy*. World Scientific Publishing Co. Pte. Ltd: 2004; Vol. 15.
23. Jasper, A. W.; Nangia, S.; Zhu, C.; Truhlar, D. G. Non-Born−Oppenheimer Molecular Dynamics. *Accounts of Chemical Research* **2006,** *39* (2), 101-108.
24. Levine, B. G.; Martínez, T. J. In *Isomerization through conical intersections*, PALO ALTO, 2007; ANNUAL REVIEWS: PALO ALTO, 2007; pp 613-634.
25. Rozgonyi, T.; González, L. A two-dimensional wavepacket study of the nonadiabatic dynamics of CH2BrCl. *The Journal of Physical Chemistry A* **2008,** *112* (25), 5573-5581.
26. Nakano, H. Quasidegenerate perturbation theory with multiconfigurational self‐consistent‐field reference functions. *The Journal of chemical physics* **1993,** *99* (10), 7983-7992.
27. Woywod, C.; Domcke, W.; Sobolewski, A. L.; Werner, H. J. Characterization of the S 1‐S 2 conical intersection in pyrazine using ab initio multiconfiguration self‐consistent‐field and multireference configuration‐interaction methods. *The Journal of chemical physics* **1994,** *100* (2), 1400-1413.
28. Hirata, S.; Head-Gordon, M. Time-dependent density functional theory within the Tamm–Dancoff approximation. *Chemical Physics Letters* **1999,** *314* (3), 291-299.

29. Fetter, A. L.; Walecka, J. D. *Quantum theory of many-particle systems*. Courier Corporation: 2012.
30. Handy, N. C.; Tozer, D. J. Excitation energies of benzene from Kohn–Sham theory. *Journal of Computational Chemistry* **1999,** *20* (1), 106-113.
31. Hirata, S.; Lee, T. J.; Head-Gordon, M. Time-dependent density functional study on the electronic excitation energies of polycyclic aromatic hydrocarbon radical cations of naphthalene, anthracene, pyrene, and perylene. *Journal of Chemical Physics* **1999,** *111* (19), 8904-8912.
32. Zhao, Y.; Truhlar, D. G. The M06 suite of density functionals for main group thermochemistry, thermochemical kinetics, noncovalent interactions, excited states, and transition elements: two new functionals and systematic testing of four M06 functionals and 12 other functionals. *Theoretical Chemistry Accounts* **2008,** *119* (5), 525-525.
33. Peach, M. J. G.; Benfield, P.; Helgaker, T.; Tozer, D. J. Excitation energies in density functional theory: An evaluationand a diagnostic test. *Journal of Chemical Physics* **2008,** *128* (4), 044118-044118-8.
34. Jacquemin, D.; Perpète, E. A.; Ciofini, I.; Adamo, C.; Valero, R.; Zhao, Y.; Truhlar, D. G. On the Performances of the M06 Family of Density Functionals for Electronic Excitation Energies. *Journal of Chemical Theory and Computation* **2010,** *6* (7), 2071-2085.
35. Peverati, R.; Truhlar, D. G. Performance of the M11 and M11-L density functionals for calculations of electronic excitation energies by adiabatic time-dependent density functional theory. *Physical Chemistry Chemical Physics* **2012,** *14* (32), 11363-1137.
36. Isegawa, M.; Peverati, R.; Truhlar, D. G. Performance of recent and high-performance approximate density functionals for time-dependent density functional theory calculations of valence and Rydberg electronic transition energies. *Journal of Chemical Physics* **2012,** *137* (24), 244104.
37. Casida, M. E.; Huix-Rotllant, M. Progress in time-dependent density-functional theory. *Annual Review of Physical Chemistry* **2012,** *63* (1), 287-323.
38. Brillouin, L. Les problèmes de perturbations et les champs self-consistents**1932**.
39. Hsu, C.-P.; Hirata, S.; Head-Gordon, M. Excitation Energies from Time-Dependent Density Functional Theory for Linear Polyene Oligomers: Butadiene to Decapentaene. *The Journal of Physical Chemistry A* **2001,** *105* (2), 451-458.
40. Maitra, N. T.; Zhang, F.; Cave, R. J.; Burke, K. Double excitations within time-dependent density functional theory linear response. *Journal of Chemical Physics* **2004,** *120* (13), 5932-5937.
41. Elliott, P.; Goldson, S.; Canahui, C.; Maitra, N. T. Perspectives on double-excitations in TDDFT. *Chemical Physics* **2011,** *391* (1), 110-119.

42. Yang, Y.; Van Aggelen, H.; Yang, W. Double, Rydberg and charge transfer excitations from pairing matrix fluctuation and particle-particle random phase approximation. *Journal of Chemical Physics* **2013,** *139* (22), 224105.
43. Shao, Y.; Head-Gordon, M.; Krylov, A. I. The spin-flip approach within time-dependent density functional theory: Theory and applications to diradicals. *Journal of Chemical Physics* **2003,** *118* (11), 4807-4818.
44. Huix-Rotllant, M.; Filatov, M.; Gozem, S.; Schapiro, I.; Olivucci, M.; Ferré, N. Assessment of Density Functional Theory for Describing the Correlation Effects on the Ground and Excited State Potential Energy Surfaces of a Retinal Chromophore Model. *Journal of Chemical Theory and Computation* **2013,** *9* (9), 3917-3932.
45. Liu, X.; Ou, Q.; Alguire, E.; Subotnik, J. E. Communication: An inexpensive, variational, almost black-box, almost size-consistent correction to configuration interaction singles for valence excited states. *Journal of Chemical Physics* **2013,** *138* (22), 221105.
46. Li, S. L.; Marenich, A. V.; Xu, X.; Truhlar, D. G. Configuration Interaction-Corrected Tamm–Dancoff Approximation: A Time-Dependent Density Functional Method with the Correct Dimensionality of Conical Intersections. *The Journal of Physical Chemistry Letters* **2014,** *5* (2), 322-328.
47. Liu, X.; Subotnik, J. E. The Variationally Orbital-Adapted Configuration Interaction Singles (VOA-CIS) Approach to Electronically Excited States. *Journal of Chemical Theory and Computation* **2014,** *10* (3), 1004-1020.
48. Yang, Y.; Shen, L.; Zhang, D.; Yang, W.; Energy Frontier Research Centers . Center for the Computational Design of Functional Layered, M. Conical Intersections from Particle–Particle Random Phase and Tamm–Dancoff Approximations. *The Journal of Physical Chemistry Letters* **2016,** *7* (13), 2407-2411.
49. Fuks, J. I.; Nielsen, S. E. B.; Ruggenthaler, M.; Maitra, N. T. Time-dependent density functional theory beyond Kohn-Sham Slater determinants**2016,** *18* (31), 2976-2985.
50. Mead, C. A. The "noncrossing" rule for electronic potential energy surfaces: The role of time-reversal invariance. *The Journal of Chemical Physics* **1979,** *70* (5), 2276-2283.
51. Schmidt, M. W.; Baldridge, K. K.; Boatz, J. A.; Elbert, S. T.; Gordon, M. S.; Jensen, J. H.; Koseki, S.; Matsunaga, N.; Nguyen, K. A.; Su, S.; Windus, T. L.; Dupuis, M.; Montgomery, J. A. General atomic and molecular electronic structure system. *Journal of Computational Chemistry* **1993,** *14* (11), 1347-1363.

52. Gordon, M. S.; Schmidt, M. W. Advances in electronic structure theory: GAMESS a decade later. In *Theory and applications of computational chemistry*, Elsevier: 2005; pp 1167-1189.
53. Shu, Y.; Higashi, M.; Marenich, A.; Olson, R.; Chamberlin, A.; Pu, J.; Kelly, C.; Thompson, J.; Xidos, J.; Li, J. GAMESSPLUS, version 2017. *University of Minnesota: Minneapolis, MN* **2017**.
54. Shu, Y.; Marenich, A. V.; Parker, K.; Truhlar, D. G. Gamess+DF: A package that incorporates dual functional—Tamm Dancoff approximation,

and the MN12-L, MN15-L, MN15 density functionals into GAMESS. https://comp.chem.umn.edu/gamess+df/.
55. Peverati, R.; Truhlar, D. G. Improving the Accuracy of Hybrid Meta-GGA Density Functionals by Range Separation. *The Journal of Physical Chemistry Letters* **2011,** *2* (21), 2810-2817.
56. Yu, H. Y. S.; He, X.; Li, S. H. L.; Truhlar, D. G. MN15: A Kohn-Sham global-hybrid exchange-correlation density functional with broad accuracy for multi-reference and single-reference systems and noncovalent interactions (vol 7, pg 6278, 2016). *CHEMICAL SCIENCE* **2016,** *7* (9), 6278-6279.
57. Frisch, M. J.; Pople, J. A.; Binkley, J. S. Self-consistent molecular orbital methods 25. Supplementary functions for Gaussian basis sets. *The Journal of Chemical Physics* **1984,** *80* (7), 3265-3269.
58. Watson, M. A.; Chan, G. K.-L. Excited States of Butadiene to Chemical Accuracy: Reconciling Theory and Experiment. *Journal of Chemical Theory and Computation* **2012,** *8* (11), 4013-4018.
59. Feller, D.; Peterson, K. A.; Davidson, E. R. A systematic approach to vertically excited states of ethylene using configuration interaction and coupled cluster techniques. *Journal of Chemical Physics* **2014,** *141* (10), 104302.
60. Sherrill, C. D.; Schaefer Iii, H. F. The Configuration Interaction Method: Advances in Highly Correlated Approaches. *Advances in Quantum Chemistry* **1999,** *34* (C), 143-269.
61. Levine, B. G.; Coe, J. D.; Martínez, T. J. Optimizing Conical Intersections without Derivative Coupling Vectors: Application to Multistate Multireference Second-Order Perturbation Theory (MS-CASPT2). *The Journal of Physical Chemistry B* **2008,** *112* (2), 405-413.
62. Werner, H.-J.; Knowles, P. J.; Knizia, G.; Manby, F. R.; Schütz, M.; Celani, P.; Korona, T.; Lindh, R.; Mitrushenkov, A.; Rauhut, G. MOLPRO, version 2012.1, a package of ab initio programs. *See http://www. molpro. net* **2012**.
63. Werner, H.; Knowles, P.; Knizia, G.; Manby, F.; Schütz, M. Wiley Interdiscip. *Rev.: Comput. Mol. Sci* **2012,** *2* (2), 242-253.

64. Hause, M. L.; Yoon, Y. H.; Crim, F. F. Vibrationally mediated photodissociation of ammonia: The influence of N-H stretching vibrations on passage through conical intersections. *Journal of Chemical Physics* **2006,** *125* (17), 174309-174309-7.
65. Ben-Nun, M.; Quenneville, J.; Martínez, T. J. Ab initio multiple spawning: Photochemistry from first principles quantum molecular dynamics. *Journal of Physical Chemistry A* **2000,** *104* (22), 5172-5175.
66. Foster, J.; Boys, S. Canonical configurational interaction procedure. *Reviews of Modern Physics* **1960,** *32* (2), 300.
67. Edmiston, C.; Ruedenberg, K. Localized atomic and molecular orbitals. *Reviews of Modern Physics* **1963,** *35* (3), 457.
68. Subotnik, J. E.; Yeganeh, S.; Cave, R. J.; Ratner, M. A. Constructing diabatic states from adiabatic states: Extending generalized Mulliken-Hush to multiple charge centers with Boys localization. *Journal of Chemical Physics* **2008,** *129* (24), 244101-244101-10.
69. Nakamura, H.; Nakamura, H.; Truhlar, D. G. The direct calculation of diabatic states based on configurational uniformity. *Journal of Chemical Physics* **2001,** *115* (22), 10353-10372.
70. Dunning Jr, T. H. Gaussian basis sets for use in correlated molecular calculations. I. The atoms boron through neon and hydrogen. *The Journal of chemical physics* **1989,** *90* (2), 1007-1023.
71. Aquilante, F.; Autschbach, J.; Carlson, R. K.; Chibotaru, L. F.; Delcey, M. G.; De Vico, L.; Fdez Galván, I.; Ferré, N.; Frutos, L. M.; Gagliardi, L.; Garavelli, M.; Giussani, A.; Hoyer, C. E.; Li Manni, G.; Lischka, H.; Ma, D.; Malmqvist, P.-Å.; Müller, T.; Nenov, A.; Olivucci, M.; Pedersen, T. B.; Peng, D.; Plasser, F.; Pritchard, B.; Reiher, M.; Rivalta, I.; Schapiro, I.; Segarra-Martí, J.; Stenrup, M.; Truhlar, D. G.; Ungur, L.; Valentini, A.; Vancoillie, S.; Veryazov, V.; Vysotskiy, V.; Weingart, O.; Zapata, F.; Lindh, R. Molcas 8: New capabilities for multiconfigurational quantum chemical calculations across the periodic table. *Journal of Computational Chemistry* **2015**.
72. Malmqvist, P. Å. Calculation of transition density matrices by nonunitary orbital transformations. *International journal of quantum chemistry* **1986,** *30* (4), 479-494.
73. Dunning Jr, T. H. Gaussian basis functions for use in molecular calculations. III. Contraction of (10s6p) atomic basis sets for the first‐row atoms. *The Journal of Chemical Physics* **1971,** *55* (2), 716-723.
74. Yang, K. R.; Xu, X.; Truhlar, D. G. Direct diabatization of electronic states by the fourfold-way: Including dynamical correlation by multi-configuration

quasidegenerate perturbation theory with complete active space self-consistent-field diabatic molecular orbitals. *Chemical Physics Letters* **2013,** *573*, 84-89.
75. Krishnan, R.; Binkley, J. S.; Seeger, R.; Pople, J. A. Self-consistent molecular orbital methods. XX. A basis set for correlated wave functions. *The Journal of Chemical Physics* **1980,** *72* (1), 650-654.
76. Dunning Jr, T. H. Gaussian basis functions for use in molecular calculations. I. Contraction of (9s5p) atomic basis sets for the first‐row atoms. *The Journal of Chemical Physics* **1970,** *53* (7), 2823-2833.
77. Hoyer, C. E.; Gagliardi, L.; Truhlar, D. G. DQΦpac 2.0: A Diabatization Program for Performing DQ and DQΦ Diabatization. https://comp.chem.umn.edu/dqphipac/.
78. Jasper, A. W.; Truhlar, D. G. Non-Born-Oppenheimer Molecular Dynamics for Conical Intersections, Avoided Crossings, and Weak Interactions. In *Conical Intersections: Theory, Computation, and Experiment*, Domcke, W.; Yarkony, D. R.; Köppel, H., Eds. World Scientific: Singapore, 2011; pp 375-412.
79. Pauling, L. *The Nature of the Chemical Bond*. Cornell university press Ithaca, NY: 1960; Vol. 260.
80. Xu, X.; Yang, K. R.; Truhlar, D. G. Diabatic Molecular Orbitals, Potential Energies, and Potential Energy Surface Couplings by the 4-fold Way for Photodissociation of Phenol. *Journal of Chemical Theory and Computation* **2013,** *9* (8), 3612-3625.
81. Kendrick, B. K.; Mead, C. A.; Truhlar, D. G. Properties of nonadiabatic couplings and the generalized Born–Oppenheimer approximation. *Chemical Physics* **2002,** *277* (1), 31-41.
82. Child, M. Electronic excitation: Nonadiabatic transitions. In *Atom-Molecule Collision Theory*, Springer: 1979; pp 427-465.
83. Meek, G. A.; Levine, B. G. Wave function continuity and the diagonal Born-Oppenheimer correction at conical intersections. *J Chem Phys* **2016,** *144* (18), 184109.
84. Bates, D. R.; McCarroll, R. Electron Capture in Slow Collisions. *Proceedings of the Royal Society of London. Series A, Mathematical and Physical Sciences* **1958,** *245* (1241), 175-183.
85. Thorson, W. R. Theory of slow atomic collisions. I. H2. *The Journal of Chemical Physics* **1965,** *42* (11), 3878-3891.
86. Melius, C. F.; Goddard, W. A. The theoretical description of an asymmetric, nonresonant charge transfer process; Li + Na + ⇌ Li + + Na the two-state approximation. *Chemical Physics Letters* **1972,** *15* (4), 524-529.

87. Chen, J. C. Y.; Ponce, V. H.; Watson, K. M. Translational factors in eikonal approximation and their effect on channel couplings. *Journal of Physics B: Atomic and Molecular Physics* **1973,** *6* (6), 965-981.
88. Thorson, W. R.; Delos, J. B. Theory of near-adiabatic collisions. I. Electron translation factor method. *Physical Review A* **1978,** *18* (1), 117-134.
89. Hahn, Y. An improved perturbed stationary state approach to ion-atom collisions. *Journal of Physics B: Atomic and Molecular Physics* **1978,** *11* (18), 3221-3233.
90. Delos, J. B. Theory of electronic transitions in slow atomic collisions. *Reviews of Modern Physics* **1981,** *53* (2), 287-357.
91. Kimura, M.; Chapman, S.; Lane, N. F. Electron capture in Ar++H2 collisions in the keV energy regime. *Physical Review A* **1986,** *33* (3), 1619-1625.
92. Macias, A.; Riera, A.; Salas, P. J.; Ponce, V. H. United-atom limit of radial couplings between molecular wavefunctions. *Journal of Physics B: Atomic and Molecular Physics* **1987,** *20* (2), 295-303.
93. Errea, L. F.; Harel, C.; Jouini, H.; Mendez, L.; Pons, B.; Riera, A. Common translation factor method. *Journal of Physics B: Atomic, Molecular and Optical Physics* **1994,** *27* (16), 3603-3634.
94. Buenker, R. J.; Li, Y. On the independence of nonadiabatic coupling elements on the choice of origin of the coordinate system. *The Journal of Chemical Physics* **2000,** *112* (19), 8318-8321.
95. Belyaev, A. K.; Dalgarno, A.; McCarroll, R. The dependence of nonadiabatic couplings on the origin of electron coordinates. *The Journal of chemical physics* **2002,** *116* (13), 5395-5400.
96. Varandas, A. Accurate ab initio potential energy curves for the classic Li–F ionic-covalent interaction by extrapolation to the complete basis set limit and modeling of the radial nonadiabatic coupling. *The Journal of chemical physics* **2009,** *131* (12), 124128.
97. Belyaev, A. K. Nonadiabatic effects in inelastic collisional processes. *Physica Scripta* **2009,** *80* (4), 048113.
98. Belyaev, A. K. Revised Born-Oppenheimer approach and a reprojection method for inelastic collisions. *Physical Review A* **2010,** *82* (6), 060701.
99. Fatehi, S.; Alguire, E.; Shao, Y.; Subotnik, J. E. Analytic derivative couplings between configuration-interaction-singles states with built-in electron-translation factors for translational invariance. *The Journal of chemical physics* **2011,** *135* (23), 234105.
100. Ou, Q.; Fatehi, S.; Alguire, E.; Shao, Y.; Subotnik, J. E. Derivative couplings between TDDFT excited states obtained by direct differentiation in the Tamm-Dancoff approximation. *The Journal of chemical physics* **2014,** *141* (2), 024114.

101. Werner, H.; Knowles, P.; Knizia, G.; Manby, F.; Schütz, M.; Celani, P.; Györffy, W.; Kats, D.; Korona, T.; Lindh, R. MOLPRO, version 2015.1, a package of ab initio programs. *University of Cardiff Chemistry Consultants (UC3): Cardiff, Wales, UK* **2015**.
102. Clark, T.; Chandrasekhar, J.; Spitznagel, G. W.; Schleyer, P. V. R. Efficient diffuse function‐augmented basis sets for anion calculations. III. The 3‐21+ G basis set for first‐row elements, Li‐F. *Journal of Computational Chemistry* **1983,** *4* (3), 294-301.
103. Weigend, F.; Ahlrichs, R. Balanced basis sets of split valence, triple zeta valence and quadruple zeta valence quality for H to Rn: Design and assessment of accuracy. *Physical Chemistry Chemical Physics* **2005,** *7* (18), 3297-3305.
104. Hoyer, C. E.; Parker, K.; Gagliardi, L.; Truhlar, D. G. The DQ and DQΦ electronic structure diabatization methods: Validation for general applications. *The Journal of chemical physics* **2016,** *144* (19), 194101.
105. Barbieri, P. L.; Fantin, P. A.; Jorge, F. E. Gaussian basis sets of triple and quadruple zeta valence quality for correlated wave functions. *Molecular Physics* **2006,** *104* (18), 2945-2954.
106. Rappoport, D.; Furche, F. Property-optimized Gaussian basis sets for molecular response calculations. *The Journal of chemical physics* **2010,** *133* (13), 134105.
107. Kendall, R. A.; Dunning Jr, T. H.; Harrison, R. J. Electron affinities of the first‐row atoms revisited. Systematic basis sets and wave functions. *The Journal of chemical physics* **1992,** *96* (9), 6796-6806.
108. Papajak, E.; Leverentz, H. R.; Zheng, J.; Truhlar, D. G. Efficient Diffuse Basis Sets: cc-pV x Z+ and maug-cc-pV x Z. *Journal of chemical theory and computation* **2009,** *5* (5), 1197-1202.
109. Papajak, E.; Truhlar, D. G. Efficient diffuse basis sets for density functional theory. *Journal of chemical theory and computation* **2010,** *6* (3), 597-601.
110. Werner, H.-J. Third-order multireference perturbation theory The CASPT3 method. *Molecular Physics* **1996,** *89* (2), 645-661.
111. Finley, J. P.-. Malmqvist, BO Roos, L. Serrano-AndrØs. *Chem. Phys. Lett* **1998,** *288* (29), 9-306.
112. Shiozaki, T.; Győrffy, W.; Celani, P.; Werner, H.-J. Communication: Extended multi-state complete active space second-order perturbation theory: Energy and nuclear gradients. American Institute of Physics: 2011.
113. Xu, X.; Zheng, J.; Yang, K. R.; Truhlar, D. G. Photodissociation dynamics of phenol: Multistate trajectory simulations including tunneling. *Journal of the American Chemical Society* **2014,** *136* (46), 16378-16386.
114. Wall, F.; Hiller Jr, L.; Mazur, J. Statistical computation of reaction probabilities. *The Journal of Chemical Physics* **1958,** *29* (2), 255-263.

115. Alder, B. J.; Wainwright, T. E. Studies in molecular dynamics. I. General method. *The Journal of Chemical Physics* **1959,** *31* (2), 459-466.
116. Bunker, D. Classical trajectory methods,". *Methods of computational physics* **2012,** *10*, 287.
117. Truhlar, D. G.; Muckerman, J. T. Reactive scattering cross sections III: Quasiclassical and semiclassical methods. In *Atom-Molecule Collision Theory*, Springer: 1979; pp 505-566.
118. Allen, M.; Tildesley, D. Computer simulation of liquids Oxford Science. London: 1990.
119. Kollman, P. Perspective on "Molecular dynamics study of liquid water". In *Theoretical Chemistry Accounts*, Springer: 2000; pp 306-307.
120. Frenkel, D.; Smit, B. Understanding Molecular Simulation. 2nd edn. San Diego and London. Academic press: 2002.
121. Marx, D.; Hutter, J. *Ab initio molecular dynamics: basic theory and advanced methods*. Cambridge University Press: 2009.
122. Karplus, M. Development of multiscale models for complex chemical systems: from H+ H2 to biomolecules (Nobel lecture). *Angewandte Chemie International Edition* **2014,** *53* (38), 9992-10005.
123. Zheng, J.; Xu, X.; Meana-Paneda, R.; Truhlar, D. G. Army ants tunneling for classical simulations. *Chemical Science* **2014,** *5* (5), 2091-2099.
124. Truhlar, D. G.; Isaacson, A. D. Statistical‐diabatic model for state‐selected reaction rates. Theory and application of vibrational‐mode correlation analysis to OH (n OH)+ H2 (n HH)→ H2O+ H. *The Journal of Chemical Physics* **1982,** *77* (7), 3516-3522.
125. Haug, K.; Schwenke, D. W.; Shima, Y.; Truhlar, D. G.; Zhang, J.; Kouri, D. J. ℒ2 Solution of the quantum mechanical reactive scattering problem. The threshold energy for D+ H2 (v= 1)→ HD+ H. *Journal of Physical Chemistry* **1986,** *90* (26), 6757-6759.
126. Chatfield, D. C.; Friedman, R. S.; Schwenke, D. W.; Truhlar, D. G. Control of chemical reactivity by quantized transition states. *The Journal of Physical Chemistry* **1992,** *96* (6), 2414-2421.
127. Bowman, J. M.; Kuppermann, A. Comparison of semiclassical, quasiclassical, and exact quantum transition probabilities for the collinear H+ H2 exchange reaction. *The Journal of Chemical Physics* **1973,** *59* (12), 6524-6534.
128. Gray, J. C.; Truhlar, D. G.; Clemens, L.; Duff, J. W.; Chapman Jr, F. M.; Morrell, G. O.; Hayes, E. F. Quasiclassical trajectory calculations compared to quantum mechanical reaction probabilities, rate constants, and activation energies for two different potential surfaces for the collinear reaction H2+ I→ H+ HI, including

dependence on initial vibrational state. *The Journal of Chemical Physics* **1978,** *69* (1), 240-252.
129. Hase, W. L.; Buckowski, D. G. Dynamics of ethyl radical decomposition. II. Applicability of classical mechanics to large‐molecule unimolecular reaction dynamics. *Journal of Computational Chemistry* **1982,** *3* (3), 335-343.
130. Schatz, G. C. The origin of cross section thresholds in H+ H2: Why quantum dynamics appears to be more vibrationally adiabatic than classical dynamics. *The Journal of chemical physics* **1983,** *79* (11), 5386-5391.
131. Gibson, L. L.; Schatz, G. C.; Ratner, M. A.; Davis, M. J. Phase space bottlenecks: a comparison of quantum and classical intramolecular dynamics for collinear OCS. *The Journal of chemical physics* **1987,** *86* (6), 3263-3272.
132. Lu, D. h.; Hase, W. L. Classical mechanics of intramolecular vibrational energy flow in benzene. IV. Models with reduced dimensionality. *The Journal of chemical physics* **1988,** *89* (11), 6723-6735.
133. Nguyen, P. H.; Stock, G. Nonequilibrium molecular-dynamics study of the vibrational energy relaxation of peptides in water. *The Journal of chemical physics* **2003,** *119* (21), 11350-11358.
134. Stock, G. Classical simulation of quantum energy flow in biomolecules. *Physical review letters* **2009,** *102* (11), 118301.
135. Park, S.-M.; Nguyen, P. H.; Stock, G. Molecular dynamics simulation of cooling: Heat transfer from a photoexcited peptide to the solvent. *The Journal of chemical physics* **2009,** *131* (18), 11B606.
136. Heller, E. J. Quantum localization and the rate of exploration of phase space. *Physical Review A* **1987,** *35* (3), 1360.
137. Guo, Y.; Thompson, D. L.; Sewell, T. D. Analysis of the zero‐point energy problem in classical trajectory simulations. *The Journal of chemical physics* **1996,** *104* (2), 576-582.
138. Stock, G.; Müller, U. Flow of zero-point energy and exploration of phase space in classical simulations of quantum relaxation dynamics. *The Journal of chemical physics* **1999,** *111* (1), 65-76.
139. Bowman, J. M.; Gazdy, B.; Sun, Q. A method to constrain vibrational energy in quasiclassical trajectory calculations. *The Journal of chemical physics* **1989,** *91* (5), 2859-2862.
140. Miller, W. H.; Hase, W. L.; Darling, C. L. A simple model for correcting the zero point energy problem in classical trajectory simulations of polyatomic molecules. *The Journal of chemical physics* **1989,** *91* (5), 2863-2868.
141. Sewell, T. D.; Thompson, D. L.; Gezelter, J. D.; Miller, W. H. Some problems of correcting the zero-point energy problem in classical trajectories. *Chemical physics letters* **1992,** *193* (6), 512-517.

142. Varandas, A.; Marques, J. Method for quasiclassical trajectory calculations on potential energy surfaces defined from gradients and Hessians, and model to constrain the energy in vibrational modes. *The Journal of chemical physics* **1994,** *100* (3), 1908-1920.
143. Peslherbe, G. H.; Hase, W. L. Analysis and extension of a model for constraining zero‐point energy flow in classical trajectory simulations. *The Journal of chemical physics* **1994,** *100* (2), 1179-1189.
144. McCormack, D. A.; Lim, K. F. The zero-point energy problem in classical trajectory simulations at dissociation threshold. *The Journal of chemical physics* **1997,** *106* (2), 572-574.
145. Xie, Z.; Bowman, J. M. Zero-point energy constraint in quasi-classical trajectory calculations. *The Journal of Physical Chemistry A* **2006,** *110* (16), 5446-5449.
146. Bonhommeau, D.; Truhlar, D. G. Mixed quantum/classical investigation of the photodissociation of NH 3 (Ã) and a practical method for maintaining zero-point energy in classical trajectories. *The Journal of chemical physics* **2008,** *129* (1), 014302.
147. Czakó, G.; Kaledin, A. L.; Bowman, J. M. Zero-point energy constrained quasiclassical, classical, and exact quantum simulations of isomerizations and radial distribution functions of the water trimer using an ab initio potential energy surface. *Chemical Physics Letters* **2010,** *500* (4-6), 217-222.
148. Czako, G.; Kaledin, A. L.; Bowman, J. M. A practical method to avoid zero-point leak in molecular dynamics calculations: Application to the water dimer. *The Journal of chemical physics* **2010,** *132* (16), 164103.
149. Quintales, L.; Varandas, A.; Alvariño, J. Quasiclassical trajectory calculations of the thermal rate coefficient for the oxygen atom+ hydroxyl. fwdarw. oxygen+ hydrogen atom reaction on realistic double many-body expansion potential energy surfaces for ground-state hydroperoxy. *The Journal of Physical Chemistry* **1988,** *92* (15), 4552-4555.
150. Uzer, T.; MacDonald, B. D.; Guan, Y.; Thompson, D. L. Theoretical studies of mode specificity in the dissociation of overtone-excited hydrogen peroxide. *Chemical physics letters* **1988,** *152* (4-5), 405-408.
151. Lu, D. h.; Hase, W. L. Classical mechanics of intramolecular vibrational energy flow in benzene. V. Effect of zero‐point energy motion. *The Journal of chemical physics* **1989,** *91* (12), 7490-7497.
152. Nyman, G.; Davidsson, J. A low‐energy quasiclassical trajectory study of O (3 P)+ OH (2Π)→ O2 (3Σ− g)+ H (2 S). II. Rate constants and recrossing, zero‐point energy effects. *The Journal of chemical physics* **1990,** *92* (4), 2415-2422.

153. Varandas, A. Excitation function for H+ O2 reaction: A study of zero‐point energy effects and rotational distributions in trajectory calculations. *The Journal of chemical physics* **1993,** *99* (2), 1076-1085.
154. Marks, A. J. Methods for constraining zero-point energy in classical Monte Carlo transition-state theory. *The Journal of chemical physics* **1998,** *108* (4), 1438-1446.
155. Varandas, A. Trajectory binning scheme and non-active treatment of zero-point energy leakage in quasi-classical dynamics. *Chemical physics letters* **2007,** *439* (4-6), 386-392.
156. Paul, A. K.; Hase, W. L. Zero-Point energy constraint for unimolecular dissociation reactions. Giving trajectories multiple chances to dissociate correctly. *The Journal of Physical Chemistry A* **2016,** *120* (3), 372-378.
157. Cao, J.; Voth, G. A. The formulation of quantum statistical mechanics based on the Feynman path centroid density. IV. Algorithms for centroid molecular dynamics. *The Journal of chemical physics* **1994,** *101* (7), 6168-6183.
158. Jang, S.; Voth, G. A. A derivation of centroid molecular dynamics and other approximate time evolution methods for path integral centroid variables. *The Journal of chemical physics* **1999,** *111* (6), 2371-2384.
159. Craig, I. R.; Manolopoulos, D. E. Quantum statistics and classical mechanics: Real time correlation functions from ring polymer molecular dynamics. *The Journal of chemical physics* **2004,** *121* (8), 3368-3373.
160. Hone, T. D.; Rossky, P. J.; Voth, G. A. A comparative study of imaginary time path integral based methods for quantum dynamics. *The Journal of chemical physics* **2006,** *124* (15), 154103.
161. Habershon, S.; Manolopoulos, D. E. Zero point energy leakage in condensed phase dynamics: An assessment of quantum simulation methods for liquid water. *The Journal of chemical physics* **2009,** *131* (24), 244518.
162. Dammak, H.; Chalopin, Y.; Laroche, M.; Hayoun, M.; Greffet, J.-J. Quantum thermal bath for molecular dynamics simulation. *Physical Review Letters* **2009,** *103* (19), 190601.
163. Perez de Tudela, R.; Aoiz, F.; Suleimanov, Y. V.; Manolopoulos, D. E. Chemical reaction rates from ring polymer molecular dynamics: Zero point energy conservation in Mu+ H2→ MuH+ H. *The journal of physical chemistry letters* **2012,** *3* (4), 493-497.
164. Habershon, S.; Manolopoulos, D. E.; Markland, T. E.; Miller III, T. F. Ring-polymer molecular dynamics: Quantum effects in chemical dynamics from classical trajectories in an extended phase space. *Annual review of physical chemistry* **2013,** *64*, 387-413.
165. Brieuc, F.; Bronstein, Y.; Dammak, H.; Depondt, P.; Finocchi, F.; Hayoun, M. Zero-point energy leakage in quantum thermal bath molecular dynamics

simulations. *Journal of chemical theory and computation* **2016,** *12* (12), 5688-5697.
166. Garashchuk, S.; Rassolov, V. A. Stable long-time semiclassical description of zero-point energy in high-dimensional molecular systems. *The Journal of chemical physics* **2008,** *129* (2), 024109.
167. Alimi, R.; García‐Vela, A.; Gerber, R. A remedy for zero‐point energy problems in classical trajectories: A combined semiclassical/classical molecular dynamics algorithm. *The Journal of chemical physics* **1992,** *96* (3), 2034-2038.
168. Sun, X.; Miller, W. H. Semiclassical initial value representation for electronically nonadiabatic molecular dynamics. *The Journal of chemical physics* **1997,** *106* (15), 6346-6353.
169. Sun, X.; Wang, H.; Miller, W. H. Semiclassical theory of electronically nonadiabatic dynamics: Results of a linearized approximation to the initial value representation. *The Journal of chemical physics* **1998,** *109* (17), 7064-7074.
170. Heller, E. J. Time‐dependent approach to semiclassical dynamics. *The Journal of Chemical Physics* **1975,** *62* (4), 1544-1555.
171. Heller, E. J. Frozen Gaussians: A very simple semiclassical approximation. *The Journal of Chemical Physics* **1981,** *75* (6), 2923-2931.
172. Hénon, M.; Heiles, C. The applicability of the third integral of motion: some numerical experiments. *The Astronomical Journal* **1964,** *69*, 73.
173. Davis, M. J.; Stechel, E. B.; Heller, E. J. Quantum dynamics in classically integrable and non-integrable regions. *Chemical Physics Letters* **1980,** *76* (1), 21-26.
174. Lim, K. F.; McCormack, D. A. The conservation of quantum zero‐point energies in classical trajectory simulations. *The Journal of chemical physics* **1995,** *102* (4), 1705-1715.
175. Bowman, J. M. Self‐consistent field energies and wavefunctions for coupled oscillators. *The Journal of Chemical Physics* **1978,** *68* (2), 608-610.
176. Gaw, J. F.; Handy, N. C. On the accuracy of higher-order force constants calculated at the self-consistent field level of theory. *Chemical physics letters* **1986,** *128* (2), 182-188.
177. Kuhler, K. M.; Truhlar, D. G.; Isaacson, A. D. General method for removing resonance singularities in quantum mechanical perturbation theory. *The Journal of chemical physics* **1996,** *104* (12), 4664-4671.
178. Garashchuk, S.; Rassolov, V. A. Energy conserving approximations to the quantum potential: Dynamics with linearized quantum force. *The Journal of chemical physics* **2004,** *120* (3), 1181-1190.

179. Mielke, S. L.; Truhlar, D. G. Displaced-points path integral method for including quantum effects in the Monte Carlo evaluation of free energies. *The Journal of Chemical Physics* **2001,** *115* (2), 652-662.
180. Mielke, S. L.; Dinpajooh, M.; Siepmann, J. I.; Truhlar, D. G. Efficient methods for including quantum effects in Monte Carlo calculations of large systems: extension of the displaced points path integral method and other effective potential methods to calculate properties and distributions. *The Journal of chemical physics* **2013,** *138* (1), 014110.
181. Michael, J. V.; Noyes, W. A. The photochemistry of methylamine. *Journal of the American Chemical Society* **1963,** *85* (9), 1228-1233.
182. Waschewsky, G.; Kitchen, D.; Browning, P.; Butler, L. Competing bond fission and molecular elimination channels in the photodissociation of CH3NH2 at 222 nm. *The Journal of Physical Chemistry* **1995,** *99* (9), 2635-2645.
183. Kassab, E.; Gleghorn, J.; Evleth, E. Theoretical aspects of the photochemistry of methanol, methylamine, and related materials. *Journal of the American Chemical Society* **1983,** *105* (7), 1746-1753.
184. Dunn, K. M.; Morokuma, K. Ab initio study of the photochemical dissociation of methylamine. *The Journal of Physical Chemistry* **1996,** *100* (1), 123-129.
185. Xiao, H.; Maeda, S.; Morokuma, K. Theoretical study on the photodissociation of methylamine involving S1, T1, and S0 states. *The Journal of Physical Chemistry A* **2013,** *117* (28), 5757-5764.
186. Michael, N. Near-UV photolysis of methylamine studied by H-atom photofragment translational spectroscopy. *Journal of the Chemical Society, Faraday Transactions* **1996,** *92* (24), 4897-4904.
187. Ashfold, M.; Dixon, R.; Kono, M.; Mordaunty, D.; Reed, C. Near ultraviolet photolysis of ammonia and methylamine studied by H Rydberg atom photofragment translational spectroscopy. *Philosophical Transactions of the Royal Society of London. Series A: Mathematical, Physical and Engineering Sciences* **1997,** *355* (1729), 1659-1676.
188. Golan, A.; Rosenwaks, S.; Bar, I. Molecular Dynamics of Methylamine Following C□ H and N□ H Vibrational Excitation and Promotion to the Ã State. *Israel Journal of Chemistry* **2007,** *47* (1), 11-16.
189. Golan, A.; Rosenwaks, S.; Bar, I. Mode-dependent enhancement of photodissociation and photoionization in a seven atom molecule. American Institute of Physics: 2006.
190. Baek, S. J.; Choi, K.-W.; Choi, Y. S.; Kim, S. K. Vibrational structures of predissociating methylamines (CH 3 NH 2 and CH 3 ND 2) in Ã states: Free internal rotation of CH 3 with respect to NH 2. *The Journal of chemical physics* **2002,** *117* (22), 10057-10060.

191. Baek, S. J.; Choi, K.-W.; Choi, Y. S.; Kim, S. K. Spectroscopy and dynamics of methylamine. I. Rotational and vibrational structures of CH 3 NH 2 and CH 3 ND 2 in Ã states. *The Journal of chemical physics* **2003,** *118* (24), 11026-11039.
192. Park, M. H.; Choi, K.-W.; Choi, S.; Kim, S. K.; Choi, Y. S. Vibrational structures of methylamine isotopomers in the predissociative Ã states: CH 3 NHD, CD 3 NH 2, CD 3 NHD, and CD 3 ND 2. *The Journal of chemical physics* **2006,** *125* (8), 084311.
193. Ahn, D.-S.; Lee, J.; Choi, J.-M.; Lee, K.-S.; Baek, S. J.; Lee, K.; Baeck, K.-K.; Kim, S. K. State-selective predissociation dynamics of methylamines: The vibronic and H/D effects on the conical intersection dynamics. *The Journal of chemical physics* **2008,** *128* (22), 224305.
194. Marom, R.; Zecharia, U.; Rosenwaks, S.; Bar, I. Vibrational overtone spectra of N–H stretches and intramolecular dynamics on the ground and electronically excited states of methylamine. *The Journal of chemical physics* **2008,** *128* (15), 154319.
195. Epshtein, M.; Portnov, A.; Bar, I. Evidence for quantum effects in the predissociation of methylamine isotopologues. *Physical Chemistry Chemical Physics* **2015,** *17* (29), 19607-19615.
196. Wang, Y.; Xie, C.; Guo, H.; Yarkony, D. R. A Quasi-Diabatic Representation of the 1, 21A States of Methylamine. *The Journal of Physical Chemistry A* **2019,** *123* (25), 5231-5241.
197. Thomas, J. O.; Lower, K. E.; Murray, C. Formation of vibrationally excited methyl radicals following state-specific excitation of methylamine. *The Journal of Physical Chemistry A* **2014,** *118* (42), 9844-9852.
198. Taylor, D.; Bernstein, E. On the low lying excited states of methyl amine. *The Journal of chemical physics* **1995,** *103* (24), 10453-10464.
199. Levi, C.; Halász, G.; Vibók, Á.; Bar, I.; Zeiri, Y.; Kosloff, R.; Baer, M. An intraline of conical intersections for methylamine. *The Journal of chemical physics* **2008,** *128* (24), 244302.
200. Levi, C.; Halász, G.; Vibók, A.; Bar, I.; Zeiri, Y.; Kosloff, R.; Baer, M. A novel intraline of conical intersections for methylamine: A theoretical study. *International Journal of Quantum Chemistry* **2009,** *109* (11), 2482-2489.
201. Yang, K. R.; Xu, X.; Zheng, J.; Truhlar, D. G. Full-dimensional potentials and state couplings and multidimensional tunneling calculations for the photodissociation of phenol. *Chemical Science* **2014,** *5* (12), 4661-4680.
202. Li, S. L.; Truhlar, D. G. Full-dimensional ground-and excited-state potential energy surfaces and state couplings for photodissociation of thioanisole. *The Journal of chemical physics* **2017,** *146* (6), 064301.

203. Zhang, L.; Truhlar, D. G.; Sun, S. Full-dimensional three-state potential energy surfaces and state couplings for photodissociation of thiophenol. *The Journal of chemical physics* **2019,** *151* (15), 154306.
204. Dill, J. D.; Pople, J. A. Self‐consistent molecular orbital methods. XV. Extended Gaussian‐type basis sets for lithium, beryllium, and boron. *The Journal of Chemical Physics* **1975,** *62* (7), 2921-2923.
205. Hehre, W. J.; Ditchfield, R.; Pople, J. A. Self—consistent molecular orbital methods. XII. Further extensions of Gaussian—type basis sets for use in molecular orbital studies of organic molecules. *The Journal of Chemical Physics* **1972,** *56* (5), 2257-2261.
206. Hariharan, P.; Pople, J. A. Accuracy of AH n equilibrium geometries by single determinant molecular orbital theory. *Molecular Physics* **1974,** *27* (1), 209-214.
207. Gordon, M. S. The isomers of silacyclopropane. *Chemical Physics Letters* **1980,** *76* (1), 163-168.
208. Ruscic, B.; Pinzon, R. E.; Morton, M. L.; von Laszevski, G.; Bittner, S. J.; Nijsure, S. G.; Amin, K. A.; Minkoff, M.; Wagner, A. F. Introduction to active thermochemical tables: Several "key" enthalpies of formation revisited. *The Journal of Physical Chemistry A* **2004,** *108* (45), 9979-9997.
209. Ruscic, B.; Pinzon, R. E.; Von Laszewski, G.; Kodeboyina, D.; Burcat, A.; Leahy, D.; Montoy, D.; Wagner, A. F. In *Active Thermochemical Tables: thermochemistry for the 21st century*, Journal of Physics: Conference Series, IOP Publishing: 2005; p 561.
210. Porterfield, J. P.; Bross, D. H.; Ruscic, B.; Thorpe, J. H.; Nguyen, T. L.; Baraban, J. H.; Stanton, J. F.; Daily, J. W.; Ellison, G. B. Thermal decomposition of potential ester biofuels. Part I: methyl acetate and methyl butanoate. *The Journal of Physical Chemistry A* **2017,** *121* (24), 4658-4677.
211. Chang, Y.-C.; Xiong, B.; Bross, D. H.; Ruscic, B.; Ng, C. A vacuum ultraviolet laser pulsed field ionization-photoion study of methane (CH 4): determination of the appearance energy of methylium from methane with unprecedented precision and the resulting impact on the bond dissociation energies of CH 4 and CH 4+. *Physical Chemistry Chemical Physics* **2017,** *19* (14), 9592-9605.
212. Ruscic, B. Uncertainty quantification in thermochemistry, benchmarking electronic structure computations, and Active Thermochemical Tables. *International Journal of Quantum Chemistry* **2014,** *114* (17), 1097-1101.
213. Ruscic, B.; Bross, D. H. Active Thermochemical Tables (ATcT) values based on ver. 1.122g of the Thermochemical Network. ATcT.anl.gov.
214. Zhao, Y.; Truhlar, D. G. The M06 suite of density functionals for main group thermochemistry, thermochemical kinetics, noncovalent interactions, excited states, and transition elements: two new functionals and systematic testing of four

M06-class functionals and 12 other functionals. *Theoretical Chemistry Accounts* **2008,** *120* (1-3), 215-241.

215. Boese, A. D.; Handy, N. C. New exchange-correlation density functionals: The role of the kinetic-energy density. *The Journal of chemical physics* **2002,** *116* (22), 9559-9569.